Universidade de Aveiro Departamento de Engenharia Cerâmica e do Vidro
2009

Daria Ivanova

Silica-scavenging effects in ceria-based electrolytes

Remoção de sílica em electrólitos à base de céria

Universidade de Aveiro Departamento de Engenharia Cerâmica e do Vidro
2009

Daria Ivanova

Silica-scavenging effects in ceria-based electrolytes

Remoção de sílica em electrólitos à base de céria

A Master Degree dissertation presented to the University of Aveiro in fulfilment of the requirements for the awarding of the Master in Materials Science and Engineering carried out under the supervision of Professor Fernando Manuel Bico Marques, Full Professor of the Department of Ceramics and Glass Engineering of the University of Aveiro.

Financial Support from ECIU Erasmus Mundus Joint Masters Programme “European Master in Materials Science and Engineering”.

The Board of Examiners

president

Dr. Joaquim Manuel Vieira
Full Professor of the Department of Ceramics and Glass Engineering of the University of Aveiro

Dr. Fernando Manuel Bico Marques
Full Professor of the Department of Ceramics and Glass Engineering of the University of Aveiro

Dr. Regina da Conceição Monteiro
Associate Professor of the Faculty of Sciences and Technology, New University of Lisbon

Acknowledgements

I would like to express my heartfelt thanks to my supervisor Prof. Dr. Fernando M. B. Marques for his patience and willingness to help me to find solutions to many problems.

I would like also to thank Dr. Vladislav Kharton, Prof. Dr. Augusto Lopes and Dr. Filipe Figueiredo for their help and advice.

I would like also to thank heartly to Dr. Alexander Shaula and Eugenie Pivak for their willingness to support me during the work in the laboratory.

I am very grateful to the “European Master Programme in Materials Science” and all coordinators of the programme for their invaluable help and financial support.

Keywords

Gadolinium-doped ceria, grain boundary, silica, scavenging effect, apatite

Summary

Gadolinium-doped ceria based powders were co-fired with additions of silica, and silica and lanthanum oxide, to test the silica-scavenging role of lanthanum. The formation of one ionic conducting secondary phase, instead of an insulating phase, was attempted. The structural, microstructural and electrical characterization of these samples confirmed the formation of one apatite-type lanthanum silicate-based phase and a significant enhancement of the grain boundary conductivity of these materials.

Palavras-chave

Céria dopada com gadolínio, fronteira de grão, sílica, efeito de remoção, apatite

Sumário

Pós de céria dopada com gadolínio foram sinterizados com adições de sílica, e de sílica e óxido de lantânio, para testar o efeito de remoção de sílica do óxido de lantânio. Com esta abordagem explorou-se a formação de uma fase secundária condutora iónica em vez de uma fase isoladora. A caracterização estrutural, microestrutural e eléctrica das amostras confirmou a formação de uma fase tipo apatite derivada do silicato de lantânio e uma melhoria significativa da condutividade da fronteira de grão destes materiais.

Abstract

Cerium oxide-based ceramic electrolytes are potential electrolyte materials for intermediate temperature solid oxide fuel cells. However, low cost single-phase ceria electrolytes show poor conductivity due to the presence of silica in such powders. The composite materials approach is used here to improve the performance of low grade ceria-based ceramic electrolytes. In recent years, a novel family of materials derived from $La_{10}(SiO_4)_6O_3$ attracted an increasing attention since they show comparatively high oxygen conductivity and low cost. The conductivity of the $La_{10}Si_{5.5}Al_{0.5}O_{26.75}$ apatite is similar to that of gadolinium-doped ceria (CGO), especially at intermediate temperatures. The high oxygen ion conduction of this family of apatites justified the attempt to form this secondary phase, in low-grade powders, from reaction of La_2O_3 with silica.

$Ce_{0.8}Gd_{0.2}O_{2-\delta}$, SiO_2 and La_2O_3 high purity powders were used as the starting materials using a conventional ceramic route. Sintering was performed at temperatures up to 1650°C, in air, using a constant heating rate of 5°C/min and cooling rate of 3°C/min. The samples were analyzed by X-ray diffraction analysis to check for their phase composition and SEM/EDS to characterize their microstructure. The bulk and grain boundary resistances of sintered pellets were obtained by ac impedance spectroscopy in air. To confirm the scavenging effect of combined addition of La_2O_3 and silica, the conductivities of pure CGO and silica-containing CGO were also investigated as reference materials.

This work demonstrated that formation of the secondary apatite phase from reaction between the precursors improved transport properties of silica-containing CGO ceramics. On the other hand, an addition of lanthanum oxide was found to change the densification and grain growth rate, resulting in grain size reduction of CGO-based ceramics. While formation of apatite phase is appealed to reduce grain boundary resistivity of CGO composites, the grain size diminution results in increase of grain boundary density, making total conductivity lower. Additionally, it was found that lanthanum oxide concentration plays determinant role in the scavenging mechanisms since this dopant tends to change the space-charge layers of CGO composites. The most pronounced scavenging effect was observed in the samples with $La_{9.33}Si_6O_{26}$ secondary phase. The formation of gadolinium apatite phase was detected in highly doped silica-containing CGO ceramics. This interesting observation opens new inside on the phase interaction of low-grade CGO powders.

Content

List of symbols

BIMEVOX – family of materials derived from $Bi_4V_2O_{11}$

$\mathbf{Ca_{Ce}^{''}}$ – calcium ion in substitutional position in the cerium sublattice, with double negative charge

$\mathbf{C_e}$ – capacitance attributed to the electrode polarization

$\mathbf{Ce_{Ce}^{'}}$ – cerium atom in the cerium sublattice with one negative charge

$\mathbf{Ce^{x}_{Ce}}$ – cerium atom in a normal site in the cerium sublattice

$\mathbf{C_g}$ – capacitance attributed to the grain interior

$\mathbf{C_{gb}}$ – capacitance attributed to the grain boundaries

CGO – gadolinium doped ceria ($Ce_{0.8}Gd_{0.2}O_{2-\delta}$)

CGO(10) – gadolinium doped ceria with formula ($Ce_{0.9}Gd_{0.1}O_{2-\delta}$)

CGOLSE – $Ce_{0.8}Gd_{0.2}O_{2-\delta}$ with addition of lanthanum oxide to form $La_{9.83}Si_6O_{26.75}$ as secondary phase

CGOLSH – $Ce_{0.8}Gd_{0.2}O_{2-\delta}$ with addition of lanthanum oxide to form $La_{10}Si_6O_{27}$ as secondary phase

CGOLSL – $Ce_{0.8}Gd_{0.2}O_{2-\delta}$ with addition of lanthanum oxide to form $La_{9.33}Si_6O_{26}$ as secondary phase

CGOSi – $Ce_{0.8}Gd_{0.2}O_{2-\delta}$ with addition of silica (SiO_2) as secondary phase

CPE – constant phase element

d – distance between crystallographic planes

$\mathbf{d}_g$ – average grain size

EDS – energy dispersive spectroscopy

$\mathbf{E_a}$ – activation energy for electrical conduction

$\mathbf{f_{gb}}$ – relaxation frequency of grain boundary impedance

$\mathbf{Ga_{Ce}^{'}}$ – gallium ion in substitutional position in the cerium sublattice, with one negative charge

$\mathbf{Gd_{Ce}^{'}}$ – gadolinium ion in substitutional position in the cerium sublattice, with one negative charge

hkl – the orientation of crystallographic place and interplanar spacing are defined by the three integers h, k, l, called indices

I – peak intensity

IT-SOFC – intermediate temperature solid oxide fuel cell

k – Boltzmann constant

L – inductance

l – thickness of specimen

LAMOX – family of materials derived from $La_2Mo_2O_9$

LGSM – family of materials with general formula $La_{1-x}Sr_xGa_{1-y}Mg_yO_{3-\delta}$

Me_{Ce}'' – rare-earth metal ion in substitutional position in the cerium sublattice, with double negative charge

n – integral number

N_{gb} – number of grain boundaries

O_o^x – oxygen ion in a normal lattice site (in the oxygen sublattice)

PVA – polyvinyl alcohol

R_b – bulk resistance of material

R_e – electrode resistance of material

R_{gb} – grain boundary resistance of material

S – electrode surface area

SEM – scanning electron microcopy

SOFC – solid oxide fuel cell

T – absolute temperature

TEC – thermal expansion coefficient

$V_o^{\cdot\cdot}$ – oxygen vacancy with double positive charge

XRD – X-ray diffraction

YSZ – yttria stabilized zirconia

Z' – real part of the impedance

Z'' – imaginary part of the impedance

Greek symbols

δ-Bi_2O_3 – bismuth oxide

$\boldsymbol{\delta_{gb}}$ – grain boundary thickness

$\boldsymbol{\varepsilon_o}$ – permittivity of vacuum

$\boldsymbol{\varepsilon_r}$ – dielectric constant of gadolinium-doped ceria

λ – wavelength

$\boldsymbol{\rho_{gb}}$ – grain boundary resistivity

$\boldsymbol{\sigma_{gb}}$ – grain boundary conductivity

$\boldsymbol{\sigma_i}$ – ionic conductivity

$\boldsymbol{\sigma_o}$ – pre-exponential factor of the ionic conductivity

Preamble

This work outlines the potential of grain boundary engineering in the development of heterogeneous ceria-based ceramics with enhanced performance. Starting from a well known solid electrolyte, the possible formation of conductive grain boundaries is addressed. Processing conditions and composition play a dominant role in the performance design of such heterostructures.

Doped ceria has been investigated over the last 30 years as a prospective electrolyte for solid oxide fuel cells (SOFCs). The advantage of ceria-based materials in this kind of devices is high oxygen conductivity even at temperatures as low as $800^{o}C$. However, the poor grain boundary conductivity of ceria-based ceramics, attributed to the accumulation of impurities in the grain boundary region, causes detrimental effects on the general performance of these materials. Silica, the dominant impurity in many low grade powders, namely in zirconia and ceria-based materials, is a representative example.

The effect of silica in grain boundaries was firstly investigated in yttria stabilized zirconia (YSZ) ceramics. The addition of Al_2O_3 to reduce the grain boundary resistivity of YSZ by removal of silica to localized areas is one of the first examples of grain boundary engineering in this field. However, to improve the grain boundary conductivity of gadolinia doped ceria (CGO) ceramics, the same alumina additions showed a negative effect due to formation of a non-conductive phase, $GdAlO_3$.

In the present work we exploit an alternative approach based on the recent discovery of high oxygen ionic conductivity in materials derived from the nominal $La_{10}(SiO_4)_6O_3$ apatite-type phase. As opposed to other attempts with the same goal, the reaction between silica and the additive (lanthanum oxide) is now expected to form one apatite phase with good ionic transport properties. In the present study the formation of a conductive apatite phase in the grain boundary region of gadolinium doped ceria was related to the microstructural development and electrical properties of these ceramics. XRD, SEM and EDS techniques were used for microstructural characterization, while the electrical properties of ceramics were evaluated by means of impedance spectroscopy.

Understanding mutual relationships between processing conditions – microstructure - properties – performance is crucial in Materials Science. A large amount of work on ceria-based electrolytes performed during the last decades played an important role in the comprehension of the most important features of ceria-based materials and served as a guide during this work.

Chapter 1 introduces ceria-based ceramics as a prospective electrolyte material for solid oxide fuel cells. The advantage of ceria-based materials is presented as well as problems related to the use of gadolinium doped ceria. The defect chemistry of ceria based ceramics partly explains the ionic transport in this family of electrolytes. The influence of concentration and types of dopants or co-dopants on the electrical performance of ceria-based ceramics is discussed. Considering the poor sinterability of ceria, ways to optimize the sintering process are reviewed. The grain boundary electrical properties of ceria-based ceramics are in the focus of this work. The role of grain boundaries is addressed from two different points of view: i) the nature of grain boundaries as a function of dopant type and content; ii) the influence of impurities on the transport properties of ceramics. The way to optimize the grain boundary properties is reviewed in terms of silica-scavenging effects.

Chapter 2 describes the experimental procedure which was adopted during this work. The materials and preparation methods are presented here. To a certain extent CGO and CGO with silica were used as reference materials. Lanthanum oxide additions to silica containing materials envisaged the removal of the latter constituent from grain boundaries. Compositions close to practical interest (modest silica impurity levels) and other compositions with exaggerated (high silica content) or unusual compositions (CGO + apatite) were prepared to improve the overall set of available information.

Since X-ray powder diffractometry, scanning electron microscopy and impedance spectroscopy techniques were used for the characterization of all prepared samples, a brief description of these techniques gives an introduction to how experimental data were obtained.

The experimental results are presented and discussed in Chapter 3. The combined characterization of samples by means of several techniques showed how the introduction of a conductive second phase can cause beneficial effects on the electrical properties of gadolinium-doped ceria ceramics. The complex relation between composition, processing conditions, microstructure and properties is addressed in this chapter.

Major conclusions and suggestions for further activity are presented in Chapters 4 and 5, respectively. Two appendixes complement the previously presented and discussed experimental data.

Chapter 1

1 Introduction

This chapter is devoted to the consideration of the most important aspects of electrolyte design for solid oxide fuel cells (SOFCs). Beginning with the principles of SOFC operation, we will move to the crucial requirements for the solid oxide electrolyte which are essential for effective SOFCs utilization. A comparative characterization of highly promising solid oxide electrolytes will be given with especial focus on materials with the fluorite structure.

The most important structural features of ceria-based materials and their electrical properties will be discussed in terms of defect chemistry and influence of dopants on the materials performance. A number of different synthesis routes of ceria-based materials will be introduced to discuss their influence on the sinterability of ceria-based powders. Special attention will be given to grain boundary effects in ceria-based electrolytes since their performance are greatly influenced by the presence of silica impurities in these materials. Several approaches are proposed to eliminate the detrimental effects of impurities on the electrical properties of ceria-based ceramics. Finally, we will focus on the optimization of electrical properties of ceria-based materials by means of the so-called silica-scavenging effect.

1.1 Solid electrolytes for solid oxide fuel cells

1.1.1 Principle of operation of solid oxide fuel cells

The solid oxide fuel cell is a device for direct conversion of chemical energy into electrical energy. The basic principle of SOFC's operation is illustrated in Figure1.1.

A fuel cell comprises two porous electrodes, with a conducting electrolyte between them. Hydrogen, one of the possibilities as fuel, is fed to the anode. On the other side, the cathode is exposed to air. An oxygen concentration gradient is created across the electrolyte. Consumption of hydrogen on the anode side also drops the local concentration of oxygen. The electrode process at this surface will allow oxygen ions to leave the electrolyte and react with the fuel which is oxidised, thereby releasing electrons. An external circuit allows electrons to flow from the anode to the cathode, where a continuous supply of oxygen ions to the solid electrolyte is provided, maintaining the overall electrical charge flow, and generating useful electrical power from the combustion of the fuel [1].

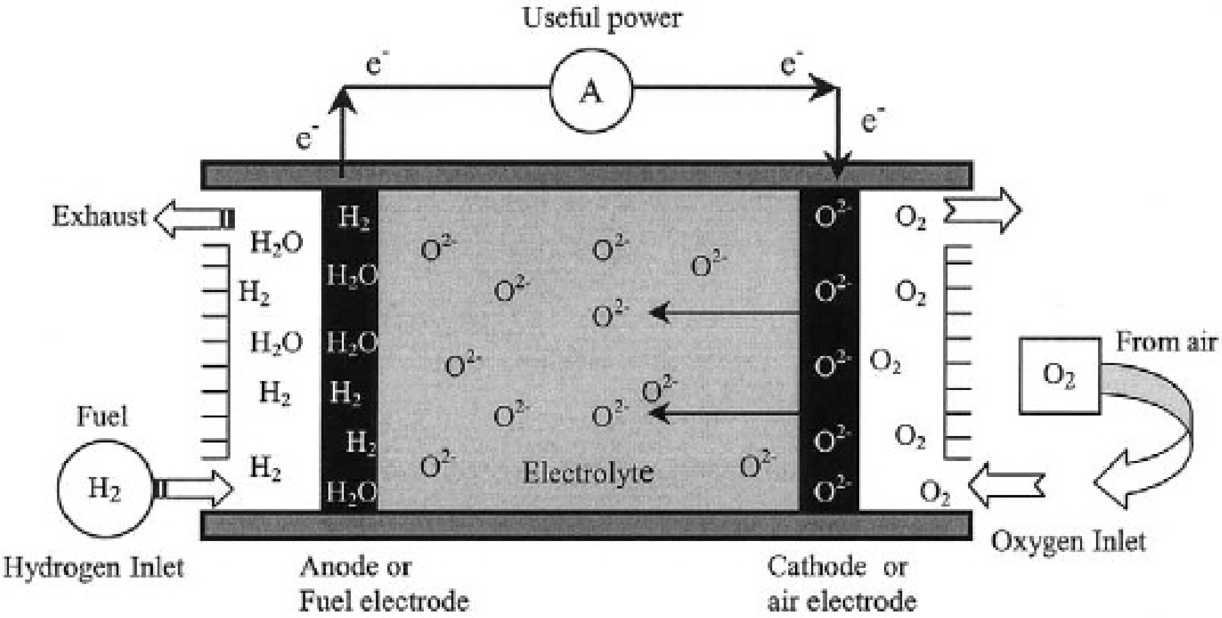

Figure 1.1 Concept diagram of SOFCs based on oxygen ion conductors [1].

1.1.2 Families of solid electrolytes for solid oxide fuel cells

Taking into account the principles and conditions of SOFC's operation, the most important requirements for the electrolyte materials for solid oxide fuel cells are high ionic conductivity, low electronic conductivity and thermodynamic stability over a wide range of temperature and oxygen partial pressure. Additionally, it is important for the solid electrolyte to have thermal expansion close to those of electrodes and other construction materials, negligible volatilization of the components, good mechanical properties and negligible interaction with the electrode materials under operating conditions. On the other hand, the cost of materials and processing conditions must not be ignored if such materials are going to be used in commercial devices. However, one of the crucial requirements is high oxygen conduction [2-6].

Investigations on potential candidates for electrolyte materials in SOFCs resulted in a wide range of different oxygen conducting materials [2-6]. One short comparison of well established and novel oxygen conductors which attracted large attention during last years is given in Table 1.1.

Table1.1. Comparative characterisation of solid electrolytes for SOFCs [2-29]

Structural type	**Main materials**	**Advantages**	**Disadvantages**
Fluorite	YSZ (yttria stabilized zirconia), CGO (gadolinia doped ceria), δ-Bi_2O_3	High ionic conductivity **(0.1 S/cm at 1000°C for YSZ and at 800°C for CGO),** thermodynamic stability in wide range of temperature and oxygen partial pressures, comparatively low cost [2-21].	High level of impurities in low-cost powders, moderate mechanical properties, relatively poor densification behaviour of CGO [2-21].
Aurivillius layered-perovskite family	$Bi_4V_2O_{11}$-based ceramics (BIMEVOX)	High oxygen conductivity **(~0.003 S/cm at 510°C)**	Unstable in reducing conditions, high chemical reactivity, low mechanical strength [5, 6, 22].
$La_2Mo_2O_9$-based structures	LAMOX	Mixed ionic-electronic conductivity, unusual mechanism of transport properties (lone –pair substitution concept) opens new research horizons.	Oxygen conductivity is about **0.0003 S/cm at 1000°C**, high TEC (thermal expansion coefficient) values, degradation behaviour at moderate oxygen pressures [3, 5, 23].
Apatite	$La_{10-x}Si_6O_{26\pm\delta}$	High oxygen conductivity **(0.0043 S/cm at 500°C)**,	Silicon oxide volatilization in reducing conditions and

		low cost, low TEC	conductivity degradation above 1100K. [3, 5, 24, 25].
$LaGaO_3$–based perovskites	$(La_{0.9}Sr_{0.1})_{0.98}$ $Ga_{0.8}Mg_{0.2}O_{3-\delta}$ - LSGM	High oxygen conductivity in the intermediate temperature range **(0.12 S/cm at 800°C)**, low TEC	Instability of Ga_2O_3 in reducing conditions, high cost, high reactivity with potential electrode materials [2, 5, 6, 26, 27].
Pyrochlore	$(Gd,Ca)_2Ti_2O_{7-\delta}$	Moderate TEC	Moderate oxygen conductivity **(0.05 S/cm at 1000°C)**. [5, 28].
Perovskite and brownmillerite-like phases	$Ba_2In_2O_5$	High proton conductivity at moderate temperatures	Instability in humid and reducing atmospheres, high reactivity with CO_2. [5, 29].

Overall, it is known that fast ion conduction in solid electrolytes requires large concentrations of ionic defects coupled with high ionic defects mobility which are governed to a great extent by structural features (low energy requirements for defect formation and hopping either involving normal lattice or interstitial sites), composition (formation of charged defects to compensate for aliovalent dopants), processing history (e.g., densification levels achieved) and other microstuctural features of these materials (due to known ion-blocking characteristics of grain boundaries).

1.1.3 The fluorite structure as one of the most promising structures for oxygen conductors

Along with other structural types, materials with fluorite structure are recognized to be amongst the best established due to their comparatively high oxygen mobility, thermodynamic stability in wide ranges of temperatures and oxygen partial pressures, and comparatively low cost. The fluorite structure allows high levels of atomic disorder which can be introduced by means of doping, also reduction or oxidation, the latter effects with likely relevance in enhancing the electrode kinetics. The oxides with cubic fluorite structure were intensively studied during the last decades [2-21]. The electrical properties of fluorite oxides are presented in Figure 1.2 [7].

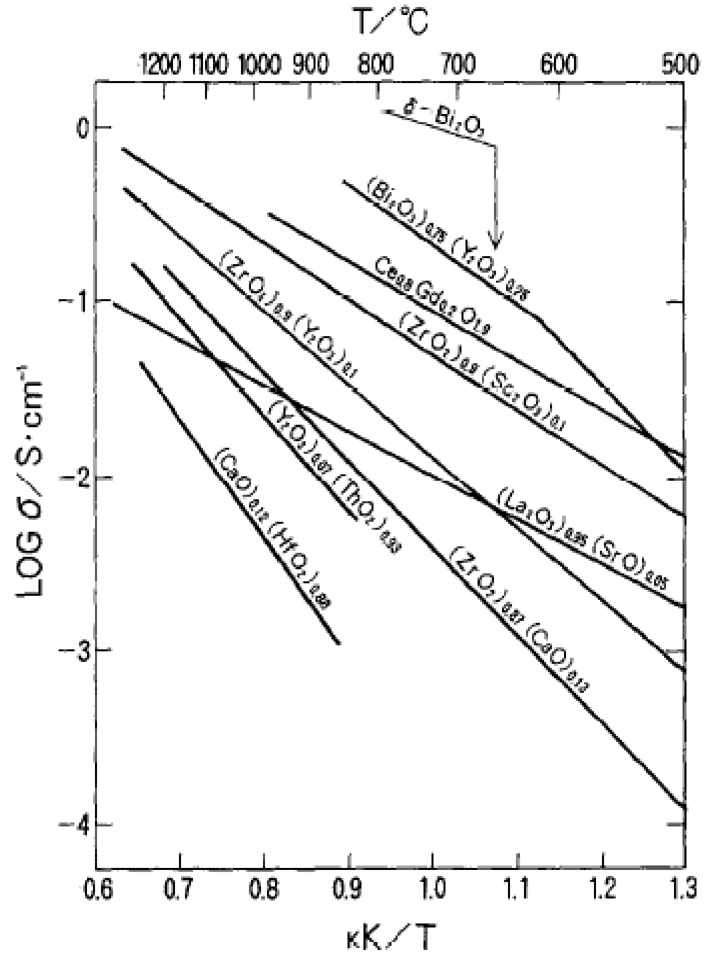

Figure 1.2 Electrical conductivity of fluorite oxides [7].

It can be seen that Bi_2O_3-based materials have the highest electrical conductivity even if compared to gadolinium-doped ceria (CGO) or Sc-doped zirconia. However, according to Inaba *et al* [7]., Bi_2O_3 is less stable in reducing atmospheres than CGO (and YSZ) and cannot be used as solid electrolyte in SOFCs.

One of the most investigated and used fluorite oxide is yttria-stabilized zirconia (YSZ) [2-6, 15-21]. Although, YSZ was considered to be one of the most promising electrolytes, due to the comparatively low ionic conductivity of zirconia-based electrolytes, the operating temperature range is limited to values of 900°C and even higher. However, one of the strategies in SOFC's development is to lower the operating temperature as far as possible, namely below 800℃ [7,8]. One of the most important reasons is to increase the lifetime of the fuel cells. At high operating temperatures, many interface reactions occurring at the electrode/solid electrolyte contacts, would decrease the efficiency and the stability of the cell [7]. Another reason is that cheap ferritic stainless steel could be used as current collector at intermediate temperatures. On the other hand, lowering the temperature also allows the replacement of other ceramic materials by metallic high-temperature alloys, less expensive and easier to fabricate than brittle ceramics [7].

The conductivity of ceria-based oxides is larger than the electrical conductivity of YSZ. Since CGO has conductivity about 0.1 S/cm at low temperatures such as 800°C, ceria-based ceramics have received increasing attention during last years [7-12].

There are several other advantages provided by ceria-based electrolytes which made them promising electrolytes for intermediate temperature SOFCs (IT-SOFCs). The thermal expansion coefficient of ceria-based ceramics is compatible with ferritic stainless steels, ideal solution for metal supported SOFCs. On the other hand, ceria-based solid electrolytes are acceptable from an economical point of view, as compared to LSGM and derivatives, namely due to the high cost of Ga. Another advantage of this group of oxygen conductors is that doped ceria is comparatively unreactive towards potential electrode materials including Mn, Co and Fe-based perovskytes. As an example, CGO has a good chemical compatibility with high performance cathode materials such as $(La_xSr_{1-x})_{0.98}Co_yFe_{1-y}O_{3-\delta}$ [11].

There are also several problems related to the partial reduction of Ce^{4+} to Ce^{3+} under moderately reducing conditions [7]. Reduction of ceria is known to play a deleterious role in ceria-based electrolytes since high electron conductivity results in efficiency losses caused by a voltage drop due to a cell internal short-circuit current. On the other hand, this reduction can cause an isothermal chemical expansion of the ceria lattice which might lead to mechanical failure of the electrolyte under operating conditions, and delamination of the electrodes. This makes ceria-based solid electrolytes unstable above 700°C [11-13].

1.2 Ceria-based solid electrolytes

The conductivity in fluorite-based oxygen ionic electrolytes like YSZ and CGO is based on the motion of oxide ion vacancies. The oxide ion vacancies concentration influences the ionic conductivity of fluorite-type oxides to a great extent. For low defect concentrations, the ionic conductivity tends to be proportional to the defect concentration. For high defect concentrations, the conductivity drops due to strong defect interaction. There are two main ways to introduce additional oxygen vacancies into these materials [7]:

i. reduction of the material in reducing conditions, when the loss of oxygen is accompanied by reduction of Ce^{4+} to Ce^{3+};

ii. doping with a lower valence cation, when the formation of oxygen vacancies is used to preserve electroneutrality.

This means that to keep the vacancy concentration constant, irrespective of the working conditions, the main controlling parameter is the dopant concentration, for proper types of dopant (radius and charge). Temperature and oxygen partial pressure will influence the formation of intrinsic defects, less effective in solid electrolyte development.

Pure stoichiometric ceria has a fluorite structure type with space group Fm3m over the whole temperature range from room temperature to the melting point. This is a significant advantage with respect to zirconia-based electrolytes, where doping is also mandatory to preserve the fluorite structure within extended ranges of working conditions.

1.2.1 Defect structure and oxygen-ion conductivity of ceria

When CeO_2 is reduced to CeO_{2-x} defects are formed in the form of Ce^{3+}, which in the Kroger–Vink-notation is written as Ce_{Ce}' (as Ce^{3+} has one negative charge compared to the normal lattice). Reduction of CeO_2 can be written as

$$O_o^x + 2Ce^x_{Ce} \leftrightarrow V_o^{\bullet\bullet} + 1/2O_2\,(gas) + 2Ce_{Ce}' \qquad (1.1)$$

O_o^x is an O^{2-} ion on its normal site in the CeO_2 lattice and $V_o^{\bullet\bullet}$ is a doubly positive charged vacancy [9].

On the other hand, additional oxygen is removed from the material (formation of oxygen vacancies) when dopants of valence lower than +4 are incorporated in the lattice.

$$CaO \leftrightarrow V_o^{\bullet\bullet} + O_o^x + Ca_{Ce}'' \tag{1.2}$$

$$Gd_2O_3 \leftrightarrow V_o^{\bullet\bullet} + 3O_o^x + 2Gd_{Ce}' \tag{1.3}$$

Thus, Gd^{3+} or Ca^{2+} cation substitute Ce^{4+} in gadolinium– or calcium-doped ceria, giving rise to formation of oxygen vacancies as schematically shown in Figure 1.3.

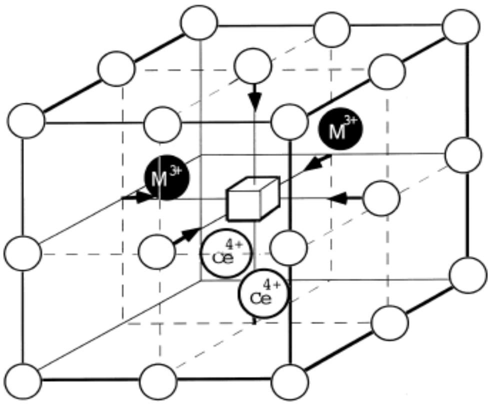

Figure 1.3 Scheme for doped ceria. The small open circles show oxygen ions. The cube indicates one oxygen vacancy. The arrows show the displacement of oxygen ions towards the vacancy along the [100] direction [14].

The vacancies that are formed as a consequence of doping shift the equilibrium in the reaction of ceria reduction to the left with a decrease in electron concentration and electron conductivity as a result. When the dopant concentration is increased the resistance to reduction increases. This means that substitution of ceria by di- or trivalent metal oxides like CaO or rare earth oxides increases the oxide ion vacancies concentration, resulting in high ionic conductivity of ceria-based electrolyte. On the other hand, increase in the concentration of the oxide vacancies results in enhanced stability of ceria under reducing conditions [9]. The enhanced ionic conductivity of doped-ceria was proved by Arai *et al.* several years ago as illustrated in Figure 1.4 [7].

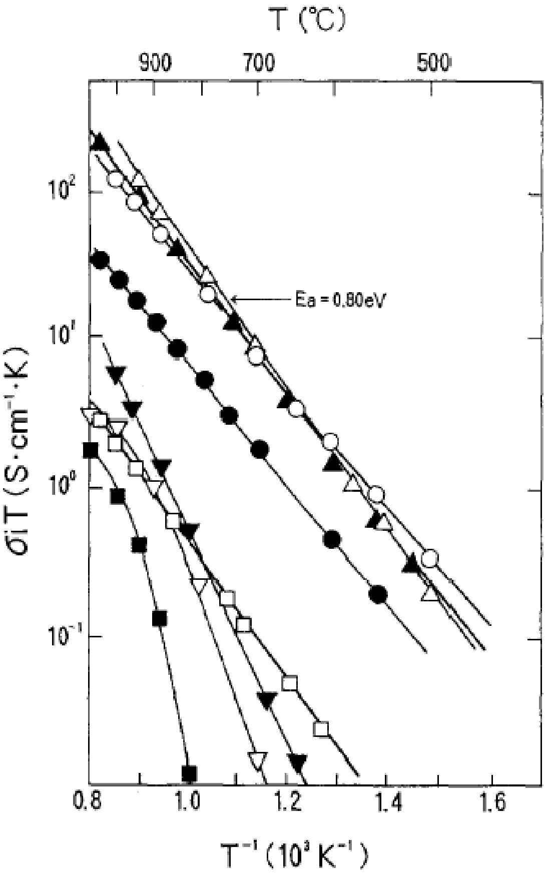

Figure 1.4 Arhenius plots of ionic conductivities of ceria-based oxides doped with alkaline-earth oxides;- $(CeO_2)_{0.9}(CaO)_{0.1}$, ▲ - $(CeO_2)_{0.7}(CaO)_{0.3}$, O - $(CeO_2)_{0.9}(SrO)_{0.1}$, ● - $(CeO_2)_{0.7}(SrO)_{0.3}$, □ - $(CeO_2)_{0.9}(BaO)_{0.1}$, ▽- $(CeO_2)_{0.9}(MgO)_{0.1}$, ▼ - $(ZrO_2)_{0.85}(CaO)_{0.15}$, ■ - CeO_2 [7].

It can be seen that the conductivity of pure ceria is several orders of magnitude lower than for the doped ceria compositions.

1.2.2 Influence of temperature and dopant concentration on the conductivity of ceria-based solid electrolytes

The ionic conductivity depends on temperature following the so-called Arrhenius-type dependence (1.4) [9]:

$$\sigma_i = (\sigma_o/T)\exp(-E_H/kT) \qquad (1.4)$$

At elevated temperatures but within the extrinsic domain, the vacancy concentration is controlled by the level of dopant ion or impurity in the material. However, at low temperature, the population of mobile charge-carrier defects is controlled by the thermodynamic equilibrium between the free defects and associated pairs (assuming that the oxygen vacancy induced by doping is bound to the dopant cation by coulombic attraction, forming defect associates) [7, 12].

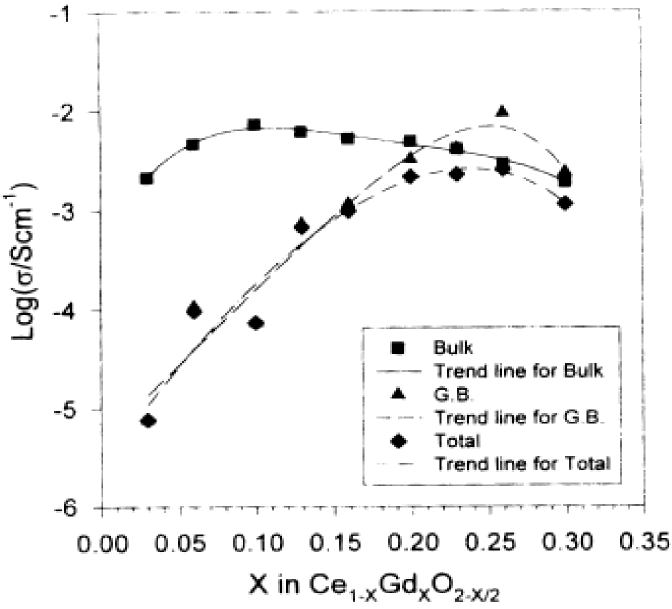

Figure 1.5 Isothermal conductivity of CGO at 500°C as a function of Gd concentration showing data for the total conductivity, grain boundary and bulk contributions [8].

As already mentioned, the assumption of the unassociated vacancies is only valid for dilute dopant concentrations. Formation of defect associates and clusters occurs at high vacancy/dopant concentrations, which leads to lower mobility of part of the oxygen vacancies [9]. Usually there is a maximum in the conductivity dependence on dopant concentration corresponding to the maximum in the concentration of unassociated vacancies, as shown in Figure 1.5.

Another phenomenon which is responsible for lower conductivity at dopant concentration higher than $x=0.25$ is an increase in the local strain produced by the dopant cation and oxygen vacancies in the ceria lattice, which decreases the oxygen diffusivity due to distortion of lattice and high level of disorder. All these phenomena cause a decrease in oxygen mobility at too high dopant concentration [14].

1.2.3 Influence of ionic radius of dopant on conductivity of ceria-based electrolytes

The ionic radius of the dopant ion also affects the electrical properties. The highest electrical conductivity is observed in compositions with Gd or Sm as dopants, as indicated in Figure 1.6. This phenomena can be attributed to the small difference between the ionic radius of Ce^{4+} and the dopant cation [7].

In fact, since the radius of Sm^{3+} and Gd^{3+} are almost the same as the ionic radius of Ce^{4+}, the dopant cation causes no contraction or expansion in the ceria lattice. On the contrary, in the cases where the dopant cations are Y or La, which differ significantly from the Ce^{4+} size, the lattice is distorted [7]. The lattice distortion of Y- or La-doped ceria is illustrated schematically in Figure 1.7. Another consequence of similar sizes of host and dopant cations is the low association enthalpy between dopant cation and oxygen vacancy, as shown in Figure 1.8(a)

Molecular dynamics calculations performed by Inaba showed that the distance Gd–O in gadolinium doped ceria is almost the same as distance Ce–O in undoped ceria [14]. This means that the internal stress in the ceria lattice induced by gadolinium doping is minimized [9]. As a result, the oxygen diffusion in gadolinium doped ceria is easier when compared with other possible dopants.

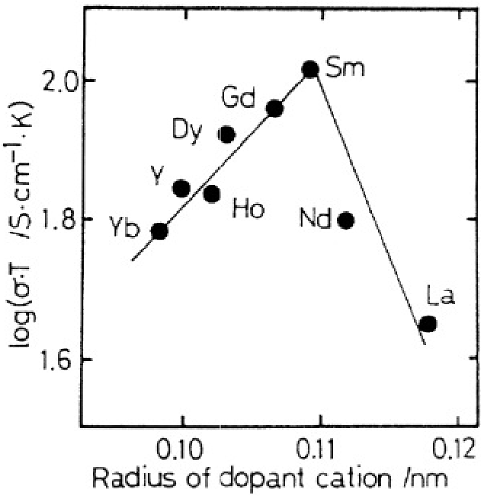

Figure 1.6 Ionic conductivity of $(CeO_2)_{1.8}(LnO_{1.5})0_{0.2}$ at 800°C as a function of the radius of the dopant ion [9].

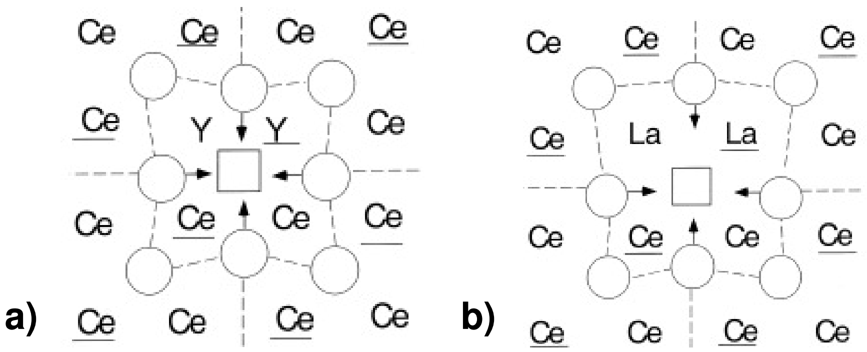

Figure 1.7 Schematic illustration of the distorted structure of Y-doped ceria (a) and La-doped ceria (b). Open circles show oxygen ions and the square shows an oxygen vacancy on the paper plane. Cations with and without underlines are above and below the paper plane, respectively. Arrows show the direction of the displacement of oxygen ions and dotted lines show the stretched oxygen-oxygen bonds [14].

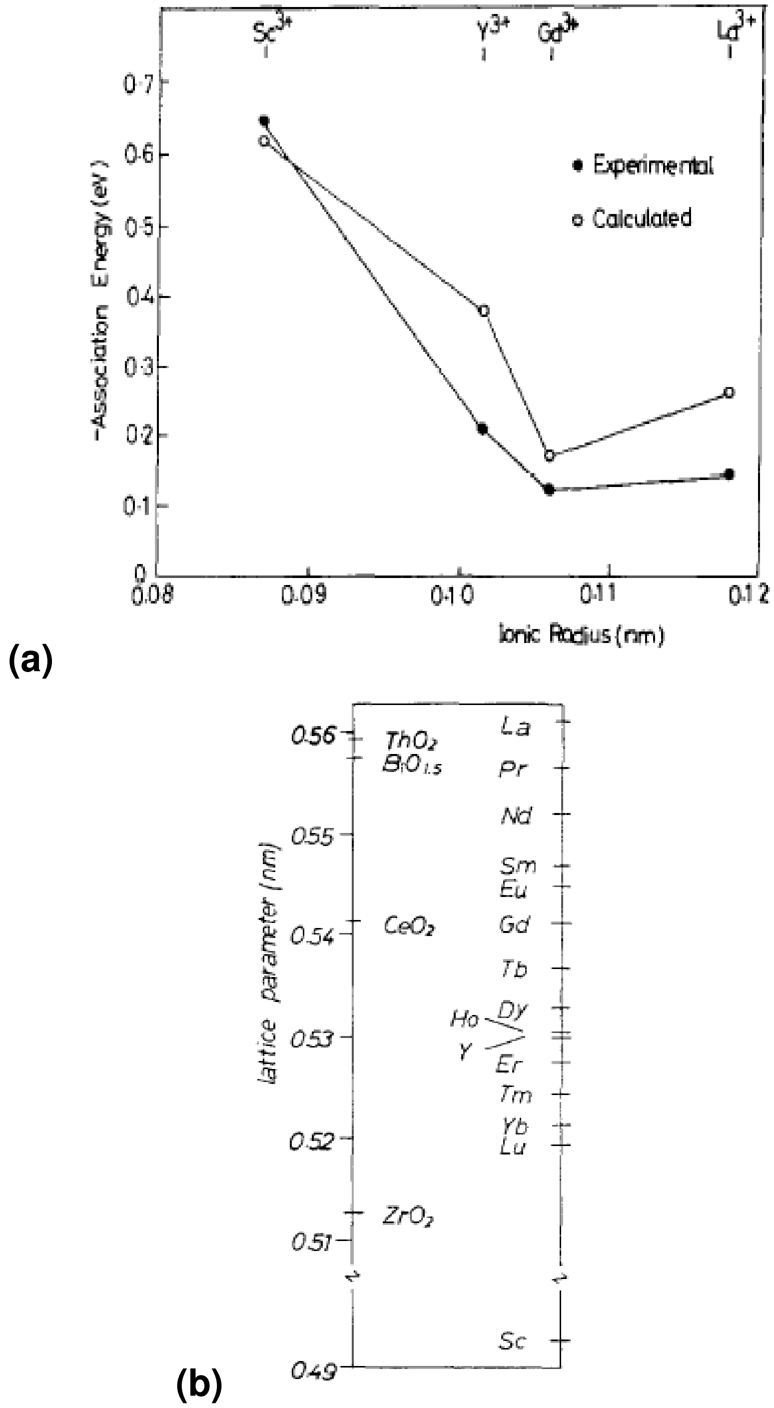

Figure 1.8 (a) Plot of binding energy (both experimental and calculated values) versus ionic radius for a range of dopant ions associated with an oxygen vacancy in CeO_2

(b) Lattice parameters of the various fluorite oxides [7].

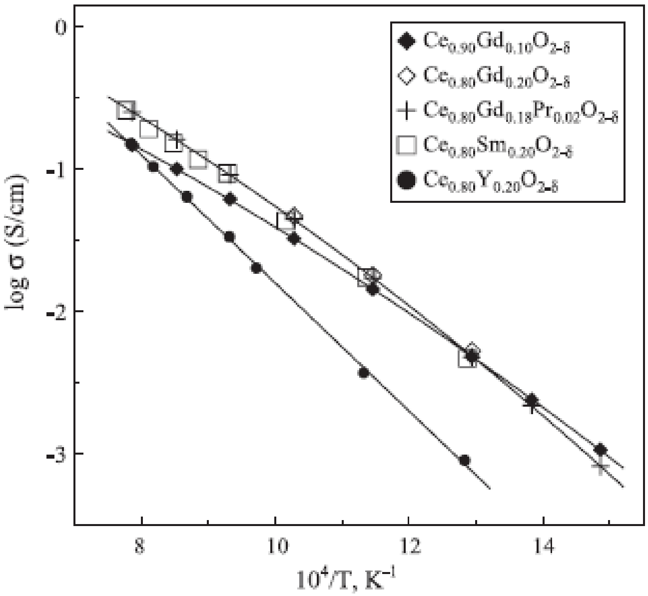

Figure 1.9 Selected data on the total conductivity of ceria based solid electrolytes in air [5].

The highest ionic conductivity in Gd-doped ceria was reported for a doping level of 20 mol%-CGO(20), as indicated in Figure 1.9 [5]. It can be noticed that 10 mol% CGO- CGO(10) has lower total conductivity if compared to CGO(20). This was explained by the fact that while CGO(10) shows higher lattice conductivity, CGO(20) is more tolerant to impurities, and, as a result of that, has higher total conductivity [5].

1.2.4 Co-doping approach towards enhanced ionic conductivity in ceria-based electrolytes

The co-doping approach was intensively evaluated during the last years in order to improve the electrical performance of ceria-based materials [30-41]. The total ionic conductivity of ceria doped with Y and several rare-earth elements like Gd, Sm, Nd and Dy is much higher (by 10-30%) than that one for the best single-doped material, taking into account that the oxygen vacancy concentration was the same for all samples prepared [30].

In order to examine the co-doping effect on the electrical properties of ceria-based ceramics a variety of co-doped ceria-based materials were investigated. Taking into account that single doped ceria $Ce_{1-x}Gd_xO_{2-y}$, $Ce_{1-x}Sm_xO_{2-y}$ and $Ce_{1-x}Y_xO_{2-y}$ show high ionic conductivity, most of the studies were focused on Gd, Sm and Y-containing samples: $Ce_{1-a}Gd_{a-y}Sm_yO_{2-0.5a}$ (wherein a=0.15 or 0.2, 0<y<a) [31], $Ce_{0.8}Sm_{0.2-x}Y_xO_{1.9}$ (x=0-0.2) [32, 33], $Ce_{0.8}Gd_{0.2-x}Y_xO_{1.9}$ (x=0-0.2) [34] and $Ce_{1-x}Sm_{x/2}Nd_{x/2}O_{2-\delta}$ (x=0.01-0.20) . [35]. In all cases examined co-doping with appropriate ratio of rare-earth elements resulted in enhanced ionic conductivity. It was also found that co-doping with alkaline-earth elements like Ca and Mg has a beneficial effect on the electrical performance of $Ce_{0.85}Gd_{0.1}Mg_{0.05}O_{1.9}$ [36], $Ce_{1-x}(Sm_{0.5}Ca_{0.5})_xO_{2-\delta}$ [33], and $Ce_{0.8+x}Y_{0.2-2x}Ca_xO_{2-\delta}$ (x=0-0.1) [37] materials, especially in the low-temperature range.

On the other hand, investigation of the electrical properties of $Ce_{0.8}La_{0.1}Y_{0.1}O_{1.9}$ showed that the oxide ionic conductivity of doubly doped ceria is similar to the average conductivity of each corresponding singly doped materials ($Ce_{0.8}La_{0.2}O_{1.9}$ and $Ce_{0.8}Y_{0.2}O_{1.9}$) [38]. However, recent work of W.Su *et al.* showed that the electrical properties of La and Y co-doped ceria-based ceramics are significantly influenced by the ratio of rare-earth elements in co-doped ceria. The highest ionic conductivity was found in $Ce_{0.8}La_{0.2-x}Y_xO_{1.9}$ samples, where x=0.06, 0.10, 0.14 [39]. The beneficial effect of co-doping is attributed to a rise in configurational entropy in the presence of several co-dopants in ceria-based ceramics [30-41]. This theory proposes that random mixing of cations enhances the disorder of oxygen vacancies, giving rise to a configurational entropy contribution. Thus, the configurational entropy of doubly-doped ceria is higher than that for singly-doped ceria solid solutions leading to higher oxygen vacancy mobility in the presence of co-dopants. The introduction of additional co-dopants in Me^{3+}-doped ceria suppresses the oxygen vacancies ordering resulting in lower activation energy of conduction and, therefore, in high ionic conductivity.

Incorporation of aliovalent ions in the ceria lattice in co-doped ceria materials leads to distortion of ceria lattice as mentioned before. This usually results in low conduction when the deviation from the lattice parameters of pure ceria is very large and in high ionic conductivity when the distortion of the ceria lattice is very small. Coherently, different ionic conductivities were observed for doubly doped ceria with the same total dopant concentration and different ratio of co-dopants [31, 34]. This cannot be explained by changes in the configurational entropy of samples. Lattice distortion in co-doped ceria samples can indeed play an important role related to the size of dopants and their relative fractions.

Kim proposed that doping with one element which would not cause either expansion or contraction of ceria lattice results in minimum elastic strain in a lattice leading to high ionic conductivity. He estimated that the critical ionic radius of dopant should be close to 0.1038 nm. This approach works well for singly-doped ceria: as the lattice distortion of Gd-doped ceria is the smallest amongst other doped materials, the highest ionic conductivity is observed [40]. Co-doping gives an opportunity to optimize the average ionic radius of the dopant playing with types of co-dopants and the composition of ceria-based ceramics. This approach was used by Omar *et al.* The electrical performance of $Ce_{1-x-y}Lu_xNd_yO_{2-\delta}$ (where x+y=0.05,0.10, 0.15, 0.20) ceramics were studied and compared with those of singly-doped Lu- and Nd-doped ceria as a function of the lattice strain produced in materials by aliovalent doping and co-doping. It was proved that samples with negligible elastic strain of the ceria lattice $Ce_{1-x-y}Lu_xNd_yO_{2-\delta}$ possess higher ionic conductivity then singly-doped materials [40].

An investigation of grain boundary and bulk contributions to the total conductivity of co-doped ceria based ceramics showed that the segregation of dopants in the grain boundary region significantly changes the grain boundary properties [37, 41].

1.3 Sinterability of CGO ceramics

Gadolinium-doped ceria is known for its poor ability to densify. High temperature (close to 1700°C) is needed to obtain ceramics with proper microstructure and high density [42]. Many attempts were made in order to decrease the sintering temperature of CGO ceramics.

It is well known that the microstructural development during sintering is greatly influenced by the particle size and properties of the initial powder. Powders with nanoscale particle size are of great interest since they provide high surface area, high reactivity and, as a consequence, high sinterability. A number of synthesis techniques was exploited in order to obtain nanocrystalline gadolinium-doped ceria powders.

One sol-gel method starting from a solution of nitrates and ethylene-glycol was adopted by Huang et al. in order to get one uniform CGO powder with particle size of about 250 nm [43].

Jurado reported that combustion synthesis is also a convenient technique to get homogeneous and reactive ceria-based powders [44]. Amongst other wet chemical synthesis routes, hydrothermal synthesis and co-precipitation of oxalates are also recognized to be reliable methods to achieve reactive CGO powders with nanosized particles [45, 46]. Various processing routes were analysed by Torres *et al*. 1) oxalate co-precipitation route; 2) traditional solid state ceramic technique and 3) commercial nanoscale powder prepared by the hydrothermal synthesis method. Dense ceramics were obtained sintering commercial powders at low temperatures such as 1400°C and, in the case of co-precipitated powder, at a sintering temperature of 1650°C.

Another strategy, developed for the improvement of ceria-based powders sinterability, includes the use of sintering promoters. It was found that the addition of transition metal oxides in small amounts (up to the solubility limit) to gadolinium-doped ceria promotes the densification rate and enhances grain growth resulting in compact ceramics at comparatively low sintering temperatures.

Kleinlogel and Gauckler showed that an addition of Co_3O_4 (from 0.5% to 5%) results in intensively promoted densification of CGO ceramics [47]. This allowed a decrease in sintering temperature from 1300°C for pure CGO to 900°C for Co-doped CGO ceramics. The liquid phase sintering mechanism was accepted to explain the quick densification process (in the range of 50K) in the case of Co-containing materials. The thin Co_3O_4 film formed around CGO grains during decomposition of cobalt nitrate melts at temperatures below 900°C leading to liquid phase sintering [47]. Besides, they evaluated the relationships between initial particle size of CGO powder and the effectiveness of Co doping [48]. This investigation showed that addition of Co as sintering aid provides enhanced densification rate for powders with initial particle size higher than 10 nm and is less effective for powders with small (diameter <10 nm) particles since their high surface area requires larger amounts of sintering additive to be homogeneously distributed around the nanosized particles [48].

Zhang et al. investigated the influence of the Fe_2O_3 or MnO_2 additions on the sintering behaviour of pure ceria [49, 50]. It was found that when the concentration of transition metal oxides does not exceed the solubility limit (about 1 at.%) the sinterability of ceria increases significantly. The viscous flow mechanism in the early stage of sintering was suggested to explain the promotion in densification rate for Fe or Mn doped ceria. The proposed reason for that is the high ability of transition metal ions to diffuse around the particles surface at comparatively low temperatures.

Besides, the substitution of Ce^{4+} by smaller iron or manganese ions leads to high grain boundary mobility in the final stage of sintering due to distortion of the ceria lattice and formation of numerous dislocations. This allows achieving almost completely densified ceria based ceramics at low temperatures such as 1300°C [49, 50]. However, an addition of iron or manganese oxide to ceria in amounts higher than 1% leads to formation of a second phase in the grain boundary regions causing the so-called pinning effect on grain boundary mobility and resulting in lower final density [49].

The effect of gallia additions on the microstructural development of gadolinium-doped ceria was intensively investigated by Lee [51, 52, 53]. It was found that the type of precursors plays a major role in the amount of gallia which has to be added in order to get a desirable enhancement in densification rate for ceria-based ceramics. The solubility limit of gallia is claimed to be 5% for co-precipitated ceria-based powders. With this concentration of gallia as additive the highest density was achieved. However, in conventionally obtained CGO ceramics, the solubility limit of gallia is apparently much smaller – only 0.5%. Dissolution of gallium oxide in ceria is accompanied by formation of oxygen vacancies accordingly to the reaction

$$Ga_2O_3 \longrightarrow 2Ga'_{Ce} + V_o^{\bullet\bullet} + 3O_o^x \qquad (1.5)$$

These oxygen vacancies are claimed to facilitate mass diffusion increasing the grain boundary mobility and enhancing the densification process in the early stage of sintering of Ga-doped ceria-based ceramics. Additionally, the lattice distortion caused by gallium substitution in ceria lattice could also affect the grain boundary mobility accordingly to the theory of severely undersized dopant [54].

In the same way, alumina addition was found to promote the sintering processes in ceria-based ceramics [55, 56]. However, even though addition of transition metal oxides has a positive influence on the microstructural development of CGO, it was noticed that additives such as Al_2O_3 or MnO_2 cause a detrimental effect on the electrical properties of ceramics. The reason for that is a sharp decrease in grain boundary conduction due to formation of secondary phases along the grain boundary in the presence of manganese oxide, and formation of thin resistive layers of $GdAlO_3$ in the grain boundary region of Al-doped ceramics [57, 58].

Co-doped CGO ceramics sintered at temperatures higher then 1000°C have lower bulk conductivity when compared with undoped CGO due to dissolution of Co in the ceria lattice and strong vacancy association [59].

High energy ball-milling seems to be an alternative approach for the improvement of the sinterability of ceria-based ceramics for several reasons. First of all, it creates conditions for the formation of homogeneous fine powders with weak agglomeration, large specific surface area and narrow particle size distribution. Moreover, this technique can be used with low-cost and widely available oxides as starting materials to produce nanocrystalline powders in large amounts [53, 58].

1.4 Silica impurity in ceria-based solid electrolytes

1.4.1 Grain boundary effects in ceria-based electrolytes

The total conductivity of polycrystalline ceramics consists of grain boundary and grain interior conductivity contributions. The specific grain boundary conductivity is known to be several orders of magnitude smaller than bulk conductivity [8]. As bulk and grain boundary contributions are in series, low grain boundary conductivity results in a low total conductivity of the material (Table 1.2).

Table 1.2. Comparison of lattice and total resistivities for selected electrolyte compositions [8]

Composition	Lattice resistivity ρ_L, 600°C (Ω cm)	Total resistivity ρ_T, 690°C (Ω cm)	Ratio ρ_T/ρ_L
$Ce_{0.9}Gd_{0.1}O_{1.95}$	40[a]	10600[d]	265
$Ce_{0.9}Gd_{0.1}O_{1.95}$	40[a]	873[e]	22
$Ce_{0.8}Gd_{0.2}O_{1.9}$	55[b]	110[f]	2
$Ce_{0.9}Sm_{0.1}O_{1.95}$	110[c]	1429[g]	13

Factors such as microporosity of the grain boundaries and segregation of dopant ions lower the conductivity significantly [9]. Thus, the grain boundary resistivity is greatly influenced by the dopant concentration and microstructure of ceramics. Christie and Berkel demonstrated that even high purity CGO ceramics with evident absence of secondary phases in the grain boundary region and direct grain to grain contact show large grain boundary resistance. The grain boundary conductivity of CGO ceramics with grain size (GS) bigger then 3 μm was found to be in linear dependence with grain size. This means that the more grain boundaries per unit area the bigger grain boundary resistivity is expected [60]. However, specimens with small mean grain size (GS<3 μm) show abnormally high grain boundary conductivity. This effect needs further investigation to be explained [60]. Thus, grain size, affected by sintering time and temperature, is extremely important in the engineering of the grain boundary contribution to the electrical performance of these materials.

The introduction of acceptor-type dopants such as Ca^{2+} or Gd^{3+} results in formation of the space-charge layers in the grain boundary regions [9]. The depletion of oxygen vacancies as a result of negatively charged Ca_{Ce}'' (or Gd_{Ce}') species segregation in the grain boundary region significantly reduces the ionic transport through the intergranular phase (Figure 1.10) [61].

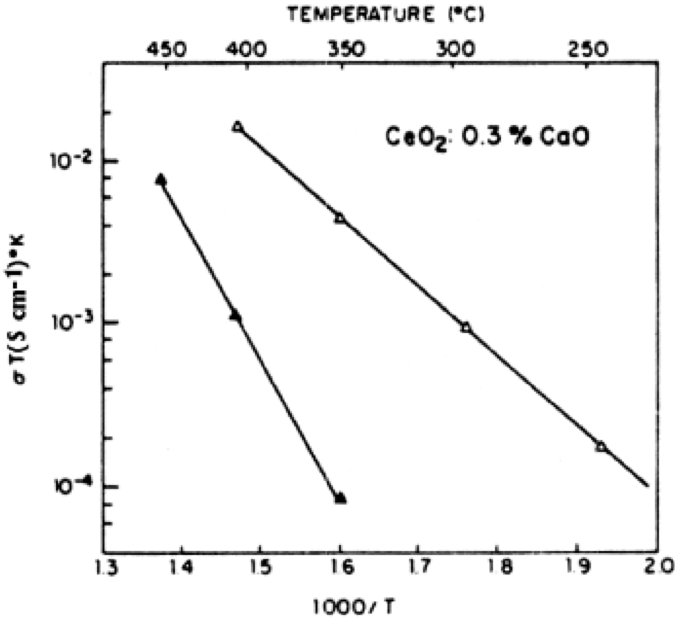

Figure 1.10 Plot of σT vs. 1/T for the CeO_2;0.3% CaO sample based on a.c. measurements. Solid triangles are for bulk + grain boundary and open triangles for bulk conductivity [9].

It was also demonstrated that the space-charge potential decreases with increasing dopant content [62]. That is why even high purity CGO ceramics demonstrate high grain boundary resistivity. However, the main contribution to the grain boundary resistivity is related to the presence of impurities in ceria-based materials [8].

At high temperatures the electrical properties of ceria-based ceramics are usually limited by the grain interior resistance only. However, in the low/intermediate temperature range, resistive grain boundaries affect considerably the actual performance [8].

It is depicted in Figure 1.11 that the grain boundary contribution to the total resistivity of pure CGO(10) cannot be detected above 500°C, while for impure CGO(10) the grain boundary contribution becomes visible already below 1000°C. In the low temperature range, the activation energy attributed to the grain boundary conductivity is much higher than the activation energy for bulk conductivity. This makes the total conductivity of the ceramics much lower in the presence of impurities in the material at low temperatures [8].

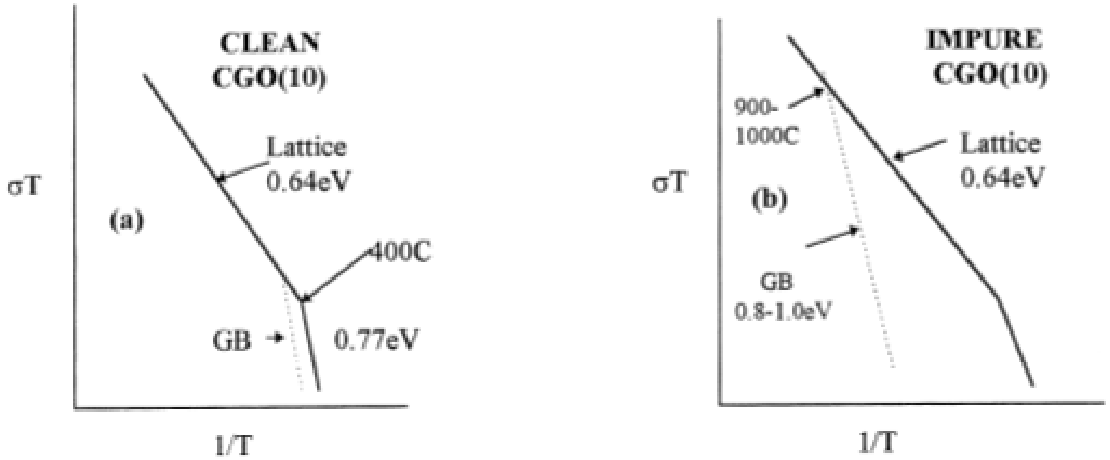

Figure 1.11 Schematic σT vs. 1/T relationships for lattice and grain boundary contributions for (a) pure CGO(10) and impure CGO(10) [8].

Silica impurities are recognized to be the predominant constituent of the grain boundary region in low grade ceria-based materials. There are several reasons for the presence of SiO_2 in ceria. Firstly, since silica is ubiquitous in minerals it can come from the original ore. Another possibility is the contamination by SiO_2 from the furnace refractories during high temperature sintering [8].

Segregation of SiO_2 impurities at the grain boundaries during sintering causes a deleterious effect on the total conductivity of CGO ceramics since the ionic conductivity of this glassy siliceous layer is several (about four) orders of magnitude lower than the transport properties of CGO [8].

Several models were proposed to describe the grain boundary effects in solid electrolytes [15]. The so-called "brick layer model" describes the material as consisting of highly conductive grains, which are separated by relatively thin uniform grain boundaries. This model is usually applied to two extreme cases: highly pure materials or highly impure materials. In the first case, the grain boundary conductivity is determined by space-charge effects which result of the segregation of solute components at the grain boundaries. In highly impure samples, continuous siliceous layers surround all grains – Figure 1.12.

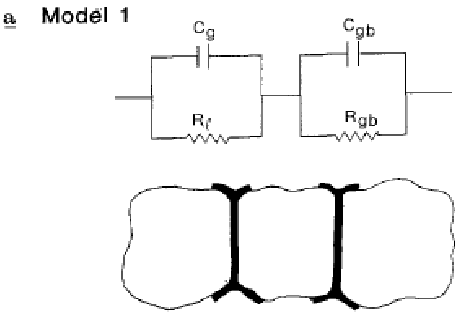

Figure 1.12 Model and equivalent circuit describing one grain boundary phase surrounding all grains [15].

The oxygen ion transport across the grain boundaries is expected to proceed through this glassy phase. Taking into account the well-known low oxygen conductivity of silicate glasses, the presence of continuous amorphous grain boundary phases causes a detrimental effect on the electrical properties of ceramics.

In most materials with modest impurity levels, silica does not form continuous siliceous films covering the grains. A “parallel model” assumes that the grains are *partially* covered by the siliceous phase. In this case, an oxygen ion can move across the grain boundaries in the places free from silica, through direct grain-grain contact, while the siliceous phase is located at triple grain junctions and in pockets along some grain boundaries as show in Figure 1.13. In this case part of the diffusion pathways will be blocked by the highly resistive glassy phase.

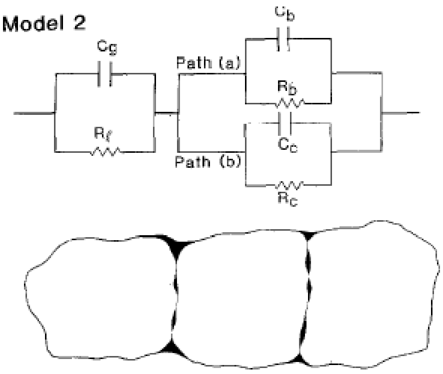

Figure 1.13 Model and equivalent circuit describing one partially wetting grain boundary phase. [15].

The parallel model is considered to be more accurate especially in low content Si-containing electrolytes [15].

In polycrystalline ceramics, grain boundaries play an important, sometimes, controlling role on the electrical properties of materials. An investigation of the grain boundary effects is essential for the design of ceramics materials in order to control and optimize their performance. Due to their relatively high oxygen ion conductivities, doped cerium oxide ceramic electrolytes are potential electrolyte materials for intermediate-temperature solid oxide fuel cell applications. However, the utilization of single-phase ceria electrolytes in SOFCs has been limited by the poor grain boundary conductivity which arises mainly from the presence of silica in cheap commercially available powders. Alternative strategies towards improved performance of low grade powders are needed to bring the cost of materials to competitive levels. The composite approach is widely used nowadays since it provides an easy optimization of performance by means of introduction of one second phase. This approach will be presented in the following discussion.

1.4.2 Scavenging effects in ceria-based electrolytes

The detrimental effect of silica on the grain boundary conductivity is well investigated for YSZ ceramics [15, 16, 17]. Many attempts were undertaken to eliminate the negative effect of impure grain boundaries on the total conductivity of YSZ and CGO ceramics. Most methods are based on the addition of metal oxides to YSZ or CGO. An addition of Al_2O_3 (up to 5 mol %) was found to be a very popular method to reduce the grain boundary resistivity of YSZ ceramics [18, 19, 20, 21]. Several models were developed to explain the scavenging effect of Al_2O_3 additions to YSZ ceramics. Firstly, possible reaction between silica and Al_2O_3 can lead to concentration of the new phase in the triple points resulting in scavenging of silica from the grain boundaries. Additionally, change in the viscosity and wetting nature of silica due to dissolution of Al_2O_3 in the silica containing glass phase could be responsible for increased grain boundary conduction. Another possible explanation of the scavenging effect is that silica could be attracted to the Al_2O_3 interface due to the different wettability of two phases [63]. Overall, Al_2O_3 is recognized to be one of the most effective additive for YSZ materials to provide a scavenging effect of silica impurities.

Several attempts were undertaken by Zhang *et al.* in order to decrease the negative effect of resistive grain boundaries on the electrical performance of CGO ceramics. Alumina as additive to improve the grain boundary conductivity of CGO ceramics showed that this addition caused a deleterious effect due to formation of another non-conductive $GdAlO_3$ phase [57]. On the other hand, it was shown that addition of Fe_2O_3 (optimum concentration was found to be 0.5 at %) decreases the grain boundary resistivity of CGO(10) [64]. The scavenging mechanism of Fe_2O_3 loading was explained in terms of change in the viscosity and wetting nature of Si-rich glass phase due to dissolution of Fe_2O_3 there or/and trapping of SiO_2 at the Fe_2O_3 interface [63].

As was reported by Zhang *et al.*, an addition of CuO, CoO or MnO_2 improves the sinterability of ceria-based materials but causes negative effects on the grain boundary conductivity of CGO ceramics since they promote the propagation of the siliceous layers along grain boundaries. This effect becomes even more pronounced at high sintering temperatures [58, 65].

One detailed study of Perez-Coll et al. showed that an addition of Co causes an advantageous effect on the grain boundary conductivity as well as on the sinterability of CGO powder at low sintering temperatures. Several possible mechanisms were discussed to interpret the effect of Co loading on the electrical properties of CGO ceramics. Especial attention was given to the properties of the initial powders [66]., sintering temperature [67]. and role of Gd content in CGO [68]. in correlation with the scavenging effect of Co-doping in CGO. It was found that 2 mol % Co addition causes beneficial effect on the grain boundary conductivity at sintering temperatures of 1150°C, while a decrease in grain boundary conductivity was observed for Co-containing samples sintered at 1500°C. This phenomenon is in contradiction with the "brick layer model" assuming the increase in grain boundary conductivity with rise in grain size [69]. Such behavior was attributed to the lower Co content in the grain boundary region at higher sintering temperatures (since some Co dissolved in the ceria lattice) leading to a less pronounced cleaning effect [66]. However, investigation of high purity Co-doped CGO powders showed the same tendency. This result indicated that one possible explanation for the apparent decrease in the scavenging effect of Co loading at high sintering temperatures could be a modification of resistive space charge layers of grain boundary shells in the presence of Co addition [67]. Further confirmation of the proposed mechanism was obtained after detailed investigation of Co-doped CGO ceramics with different amounts of gadolinium. [68].

Earth metal oxides such as CaO, MgO or SrO were suggested by Cho et al. as effective scavenging additions to CGO ceramics [70, 71, 72]. An improvement in grain boundary conduction of 120 times in the presence of 2-mol% CaO (or 0.5 mol % SrO) was explained by the scavenging effect due to reaction between alkaline metal oxide and silica as well as formation of a coherent faceted grain boundary structure [70,71]. An increase in the MeO level in CGO higher than 2-mol% leads to reduction in grain boundary and grain interior conduction. The solubility of CaO or SrO in ceria is relatively high due to the small difference in size of Ce^{4+} (0.97Å) and Ca^{2+}(1.12 Å) or Sr^{2+} (1.25 Å). The increased activation energy for grain boundary conduction was attributed to the formation of the space-charge layers in the grain boundary region due to incorporation of Me^{2+} ions in ceria lattice. The small reduction in bulk conductivity in the presence of MeO was explained by strong defect association between Me_{Ce}'' and $V_o^{\bullet\bullet}$ [70]. The solubility of Mg^{2+} in the ceria lattice is reported to be very small. However, an addition of 0.3-10mol % MgO was found to enhance the grain boundary conduction by 45 times due to formation of Mg_2SiO_4 as secondary phase with preferential concentration in triple points [71].

The effect of post-sintering heat treatment on the grain boundary resistance of Si-containing CGO ceramics was investigated [73]. Kim et al. showed that post sintering heat treatment at 1350°C during 20 h enlarges the grain boundary conductivity in 2.5 times. The improvement of grain boundary conduction was attributed to the change in intergranular surface after additional heat treatment [73].

1.5 The prospects of lanthanum oxide as effective scavenging addition to CGO

In recent years, a novel family of materials with an apatite structure attracted an increasing attention since they show comparatively high oxygen conductivity, low thermal expansion coefficient and low cost. The conductivity mechanism in these materials can be attributed to the formation of interstitial defects as a result of deviation from the nominal composition - $La_{10}(SiO_4)_6O_3$ - of this group of materials from the formula of an ideal apatite $(M_1,M_2)_{10}(XO_4)Z_{2.}$ [25].

Comparison of the electrical properties of apatite materials and other solid electrolytes is illustrated in Figure 1.14, accordingly to Shaula [25]. It can be seen that the conductivity of the $La_{10}Si_{5.5}Al_{0.5}O_{26.75}$ apatite is close to that of gadolinium-doped ceria, especially in the intermediate temperature range. Furthermore, these apatite-type electrolytes show a significant tolerance to a variety of other substitutions, providing a likely effective solution to remove several impurities by incorporation in one single oxygen conductive phase.

The high oxygen conduction and compositional tolerance of these apatites justified the attempt to form this phase in low-grade YSZ powders from reaction of La_2O_3 with silica. Previous work of Kovalevsky *et.al*, proved that addition of La_2O_3 provided the formation of one conductive apatite phase from combination of silica and lanthanum oxide, resulting in decreasing grain boundary resistance due to this scavenging effect [74]. One parallel detrimental effect (formation of resistive lanthanum zirconate layers), partly cancelled this improvement.

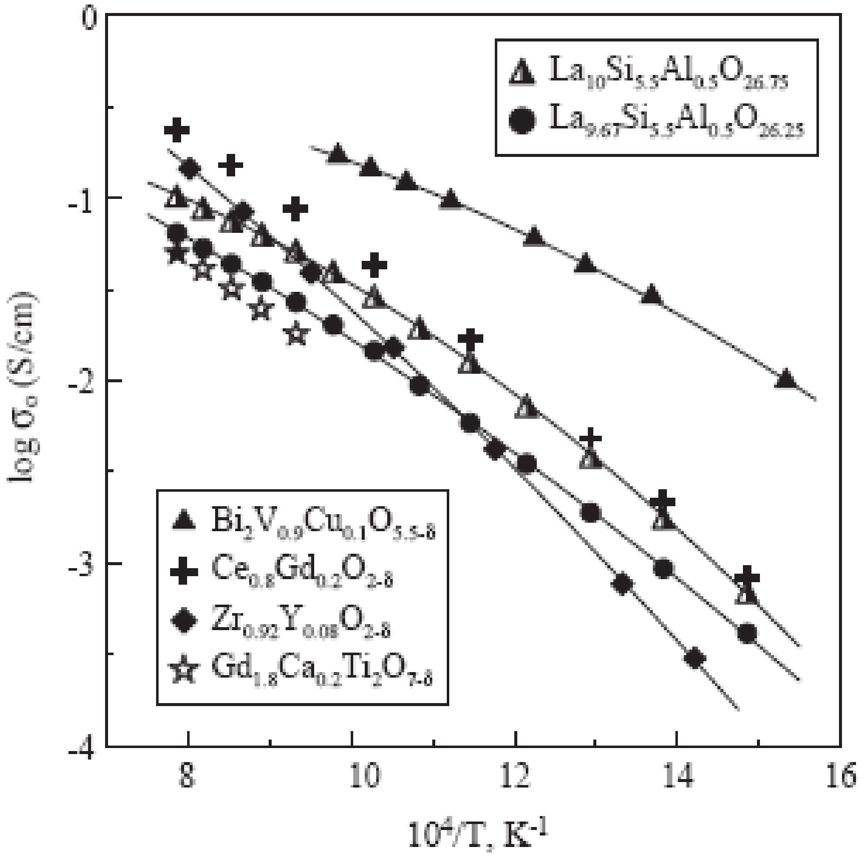

Figure 1.14. Temperature dependence of the oxygen ionic conductivity of various solid electrolytes in air [25].

Interaction of ceria-based materials with lanthanum oxide is expected to be less severe than in the case of zirconia-based materials. The present work was thus conducted to evaluate the impact of this approach on the oxygen ion transport properties of ceria-based electrolytes.

1.6 References

1 A. B. Stambouli, E. Traversa, Renewable and Sustainable Energy Reviews 6 (2002) 433–455

2 Osamu Yamamoto, Electrochimica Acta 45 (2000) 2423–2435

3 B. C. H. Steele, Journal of Materials Science 36 (2001) 1053 – 1068

4 T.H. Estell, S.N. Flengas, Chemical Review 70 (1970) 339

5 V.V. Kharton, F.M.B. Marques, A. Atkinson, Solid State Ionics 174 (2004) 135–149

6 J. W. Fergus, Journal of Power Sources 162 (2006) 30–40

7 Hideaki Inaba, Hiroaki Tagawa, Solid State Ionics 83 (1996) 1- 16

8 B.C.H. Steele, Solid State Ionics 129 (2000) 95–110

9 M. Mogensen, N. M. Sammes, G. A. Tompsett, Solid State Ionics 129 (2000) 63–94

10 T.Kudo, H. Obayashi, Journal of the Electrochemical Society 122 (1975) 1

11 V.V. Kharton, F.M. Figueiredo, L. Navarro, Ceria-based materials for solid oxide fuel cells, Journal of Materials Science 36 (2001) 1105-1117

12 B. Dalslet, P. Blennow, P. V. Hendriksen, N.Bonanos, D. Lybye, Mogens Mogensen, Journal of Solid State Electrochemistry 10 (2006) 547-561

13 D. Schneider, M.Godickemeier, L.J. Gaukler, Journal of Electroceramics 1:2 (1997) 165

14 H. Hayashia, R. Sagawa, Hideaki Inaba, Katsuyuki Kawamura, Solid State Ionics 131 (2000) 281

15 S.P.S. Badwal, Solid State Ionics 76 (1995) 67,

16 X.J.Chen, K.A. Khor, S.H. Chan, L.G.Yu, Materials Science and Engineering A 335 (2002) 246-252

17 J. Drennan, G. Auchterlonie, Solid State Ionics 134 (2000) 75-87

18 Xin Guo, Chao-Qun Tang, Run-Zhang Yuan, Journal of the European Ceramic Society, 15 (1995) 25-32

19 X.J.Chen, K.A. Khor, S.H. Chan, L.G.Yu, Materials Science and Engineering A 374 (2004) 64-71

20 Xin Guo, Solid State Ionics 96 (1997) 247-254

21 Aya Yuzaki, Akira Kishimoto, Solid State Ionics 116 (1999) 47–51

22 N. M. Sammes, G. A. Tompsett, H. Nafe and F. Aldinger, Journal of the European Ceramic Society 19 (1999) 1801-1826

23 X.P. Wang , Q.F. Fang, Solid State Ionics 146 (2002) 185

24 Susumu Nakayama and Masatomi Sakamoto, Journal, of the European Ceramic Society 18 (1998) 1413-1418

25 A.L. Shaula, V.V. Kharton, F.M.B. Marques, Journal of Solid State Chemistry 178 (2005) 2050–2061

26 K.Nomura, S.Tanase, Solid State Ionics 98 (1997) 229-236

27 J.W. Stevenson, T.R. Armstrong, L.R. Pederson, J. Li, C.A. Lewinsohn, S. Baskaran, Solid State Ionics 113–115 (1998) 571–583

28 S.A. Kramer, H.L. Tuller, Solid State Ionics, 82 (1995) 15-23

29 T. Schober, Solid State Ionics 109 (1998) 1–11

30 J. van Herle, D. Seneviratne, A.J. McEvoy, Journal of the European Ceramic Society 19 (1999) 837-841].

31 F.Y. Wang, S.Chen, S. Cheng, Electrochemistry Communications 6 (2004) 743-746

32 X. Sha, Z. Lu, X.Huang, J.Miao, L.Jia, X.Xin, W. Su, Journal of Alloys and Compounds 424 (2006) 315-321

33 M.Dudek, Journal of the European Ceramic Society 28 (2008) 965-971

34 X. Guan, H. Zhou, Y.Wang, J.Zhang, Journal of Alloys and Compounds 464 (2008) 310-316

35 S. Omar, E.D. Wachsman, J.C. Nino, Solid State Ionics 178 (2008) 1890-1897

36 F.Y. Wang, S.Chen, Q.Wang, S.Yu, S. Sheng, Cataysis Today 97 (2004) 189-194

37 Xu Hongmei, Y. Hongee, Chen Zhenhua, Solid State Ionics 10 (2008) 1179-1184

38 H. Yoshiba, H. Deguchi, K.Miura, M.Horiuchi, T. Inagaki, Solid State Ionics 140 (2001) 191-199

39 X.Sha, Z.Lu, X. Huang, J.Miao, Z. Ding, X. Xin, W. Su, Journal of Alloys and Compounds 428 (2007) 59-64

40 S. Omar, E.D. Wachsman, J.C. Nino, Solid State Ionics 177 (2006) 3199-3203

41 W. Zajak, J. Molenda, Solid State Ionics 179 (2008) 154-158

42 G.B. Bazals, R.S. Glass, Solid State Ionics 76 (1995) 155

43 K. Huang, M. Heng, J.B. Goodenough, Journal of the American Ceramic Society 81 (1998) 357

44 J.R. Juardo, Journal of Materials Science 36 (2001) 1133

45 J. Van Herle, T. Horita, T. Kawada, N. Sakai, H. Yokokawa, M. Dokiya, Solid State Ionics 86-88 (1996) 1255-1258

46 R.S. Torrens, N.M. Sammes, G.A.Tompsett, Solid State Ionics 111 (1998) 9-15

47 C. Kleinlogel, L.J. Gauckler, Solid State Ionics 135 (2000) 567–573

48 L. J. Gauckler, Journal of Electroceramics 14 (2005) 247-253

49 T.S. Zhang, P. Hing, H.Huang, J.A. Kilner, Journal of the European Ceramic Society 21 (2001) 2221-2228

50 T.S. Zhang, P. Hing, H.Huang, J.A. Kilner, Materials Letters 57 (2002) 507-512

51 J.S. Lee, K.-H. Choi, B.-K. Ryu, B.-C. Shin, I.-S. Kim Materials Research Bulletin 39 (2004) 2025

52 J.S. Lee, K.-H. Choi, Journal of Materials Science 40 (2005) 1153

53 J.S. Lee, K.-H. Choi, M.-W. Park,D.-J. Kwak, K.-H. Shin, C.-W. Shin, Journal of Materials Science 41 (2006) 7983-7988

54 P.L. Chen, I.W. Chen, Journal of the American Ceramic Society 79 (1997) 1793-1800

55 J.S. Lee, K.-H. Choi, B.-K. Ryu, B.-C. Shin, I.-S. Kim, Ceramics International 30 (2004) 807-812

56 K.-H. Choi, J.-S.-Lee, B.-K. Ryu, B.-C. Shin, I.-S. Kim, Journal of the Ceramic Society of Japan 112 (2004) S629-S632

57 T.S. Zhang, Z. Zeng, H. Huang, P. Hing, J. Kilner, Materials Letters 57 (2002) 124-129

58 T.S. Zhang, J. Ma, L.B. Kong, P. Hing, Y.J. Leng, S.H. Chan, J.A. Kilner, Journal of Power Sources 124 (2003) 26-33

59 D. P. Fagg, J. C. C. Abrantes, D. Perez-Coll, P. Nunez, V.V. Kharton, J. R. Frade Electroceramica acta 48 (2003) 1023-1029

60 G.M. Christie, F.P.F. van Berkel, Solid State Ionics 83 (1996) 17-27

61 Tshope, Solid State Ionics 173 (2004) 57

62 T.S. Zhang, J. Ma, S.H. Chan, P. Hing, J.A. Kilner, Solid State Science 6 (2004) 565-572

63 T.S. Zhang, J. Ma, S.H. Chan, J.A. Kilner, Solid State Ionics 176 (2005) 377-384

64 T.S. Zhang, J. Ma, L.B. Kong, S.H. Chan, P. Hing, J.A. Kilner, Solid State Ionics 167 (2004) 203–207

65 T.S. Zhang, J. Ma, L.B. Kong, S.H. Chan, P. Hing, J.A. Kilner, Solid State Ionics 168 (2004) 187-195

66 D. Perez-Coll, P. Nunez, D. Marrero-Lopez, J. C. C. Abrantes J. R. Frade, Journal of Solid State Electrochemistry 8 (2004) 644-649

67 D. Perez-Coll, P. Nunez, J. C. C. Abrantes, D.P. Fagg, V.V. Kharton, J. R. Frade, Solid State Ionics, 176 (2005) 2799-2805

68 D. Perez-Coll, P. Nunez, J.C. Ruiz-Morales, J.Pena-Martinez,J.R. Frade, Electrochimica Acta 52 (2007) 2001-2008

69 J.C.C. Abrantes, J.A. Labrincha, J.R. Frade, Journal of the European Ceramic Society 20 (2000) 1603-1609

70 P.S. Cho, S.B. Lee, Y.H. Cho, D.Y. Kim, Journal of Power Sources 183 (2008) 518-523

71 D. K. Kim, J.-H. Lee, P.-S. Cho, G. Auchterlonie, D.-Y. Kim, H.-M. Park, J. Drennan, Electrochemical and Solid State Letters 10 (2007) (5) B91-B95

72 Y. H. Cho, P.-S. Cho, G. Auchterlonie, D. K. Kim,J.-H. Lee, D.-Y. Kim, H.-M. Park, J. Drennan, Acta Materialia 55 (2007) 4807-4815

73 S.D. Kim, P.-S. Cho, J.-H. Lee, D.-Y. Kim, H.-M. Park, Solid State Ionics 177 (2006) 2125-2128

74 A.V. Kovalevsky, F.M.B. Marques, V.V. Kharton, F. Maxim, J.R. Frade, Ionics 12 (200X) 179-184

Chapter 2

2 Experimental procedure

In this chapter major attention is given to the experimental techniques used throughout this work. Firstly, the materials preparation route will be presented. Especial attention will be given to important parameters in solid state synthesis and to subsequent steps in the fabrication of the ceramic samples. Then we will move to a brief description of the techniques used for the investigation of the properties of the obtained ceramics. The principles of structural characterization of specimens by X–ray diffraction (XRD) will be shortly described. The use of scanning electron microscopy (SEM) for the microstructural characterization will be presented. The determination of grain boundary and bulk conductivities separately, by impedance spectroscopy, will be discussed at the end of this chapter.

2.1 Sample preparation

Commercially available $Ce_{0.8}Gd_{0.2}O_{2-\delta}$ (Rhodia), SiO_2 (Merck) and La_2O_3 (Aldrich) high purity powders were used as starting materials. All CGO-based compositions, including $Ce_{0.8}Gd_{0.2}O_{2-\delta}$ (CGO), $Ce_{0.8}Gd_{0.2}O_{2-\delta}$ with silica (CGOSi), and CGOSi with addition of lanthanum oxide (CGOLS*X*, with the meaning of *X*=L, E or H described below), were prepared using a conventional ceramic processing route. Lanthanum oxide was added in adequate proportions to fully combine with silica either as $La_{9.33}Si_6O_{26}$ (LSL), as $La_{9.83}Si_6O_{26.75}$ (LSE), or as $La_{10}Si_6O_{27}$ (LSH), assuming that these apatite phases ideally form as part of the scavenging effect. This range of nominal compositions should also provide some information on the optimization of the silica scavenging process by appropriate dosage between silica and lanthanum oxide. Pure CGO and compositions containing different amounts of silica were used for comparison.

The reference amount of SiO_2 addition (0.5 mol%) was chosen taking into account typical concentrations of silica impurities in low-grade CGO powders (Si > 500ppm). As small quantities of this additive (or derived phases) are difficult to identify by X-ray diffraction (XRD) and/or scanning electron microscopy combined with energy dispersive spectroscopy (SEM/EDS), an additional set of compositions was investigated where the amount of additive was 5 mol % (SiO_2 addition).

There are two possible ways to introduce the apatite phase in CGO. The first one is to sinter CGO with SiO_2 and La_2O_3 oxides, closer to the expected circumstances foreseen for the silica scavenging process. Another way is to pre-synthesize the apatite separately with subsequent sintering after mixing with CGO. Namely due to the highly hygroscopic nature of lanthanum oxide, the samples produced mixing CGO with SiO_2 and La_2O_3 had low densities. Better samples were produced sintering together CGO with the already formed apatite phases. Although deviating from the central goal of this work, these samples provided interesting information on phase interaction.

Before proper dosage, lanthanum oxide and silica were annealed in air at 1200°C and 600°C, respectively. When the apatite was synthesized before sintering with CGO, SiO_2 and La_2O_3 were mixed with ethanol and polyvinyl alcohol (PVA, binder) and homogenized in one agate mortar. The three kinds of apatite-containing samples (CGOLSL, CGOLSE and CGOLSH) were pre-synthesized at 1200°C during 6h. Stoichiometric amounts of powders were mixed together with ethanol in a ball-mill for 4 h, using zirconia milling media. The slurries of all compositions were dried; the obtained powders were afterwards homogenized and mixed in an agate mortar with PVA, to reach higher plasticity and cohesion of powders during shaping. Lastly, the powders were uniaxially pressed (220 MPa) into cylindrical pellets.

For the fabrication of dense and crack-free ceramics the following temperature/time conditions were chosen for all compositions: 1) 1500°C/10h; 2) 1550°C/4h; 1) 1600°C/4h; 1) 1650°C/4h. Sintering was performed in air atmosphere at a constant heating rate of 5°C/min and cooling rate of 3°C/min.

Values of final densities of pellets were calculated from the mass and geometrical dimensions of the pellets.

2.2 Structural characterization

X-ray diffraction analysis (XRD) was used for the characterization and identification of crystalline phases in all samples.

In X-ray diffraction we normally distinguish between single crystal and polycrystalline or powder applications. X-ray powder diffraction is a non-destructive technique widely applied in the characterization of crystalline materials. The method has been traditionally used for phase identification, quantitative analysis and determination of structural imperfections [1].

Since interatomic distances are comparable in magnitude to the X-ray wavelengths and X-rays can be scattered by ions in crystalline solids, diffraction occurs when X-rays pass through a regular array of ions in crystalline samples. A diffracted beam may be described as a beam composed of a large number of X-ray reflections from a series of parallel planes inside the crystal. As the crystal structure and interatomic distances are different for each material, the diffraction pattern is individual for every crystalline substance. Moreover, in a mixture of substances, each one of them produces one pattern independent of the others. Thus, XRD is commonly used for identification purposes. It is customary to obtain the complete powder diffraction pattern of the material, which may then be compared directly with the patterns of known substances [1].

Basically, constructive interference occurs between x-rays diffracted from different planes from the same family when their path difference is equal to a whole number of wavelength. This means that diffraction is observed when the conditions of Bragg's law are accomplished:

$$n\lambda = 2d\sin\theta \qquad (2.1)$$

where λ is the wavelength of the X-ray radiation; d is the perpendicular distance between crystallographic planes; θ is half the angle through which the incident beam is diffracted by a particular family of planes and n is the order of reflection (Figure 2.1).

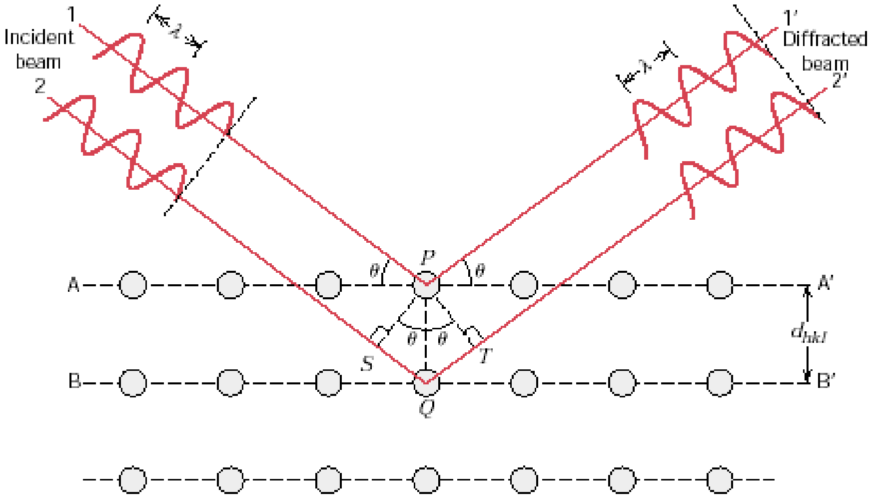

Figure 2.1 Diffraction of X-ray by planes of atoms (A – A' and B – B') [1].

Diffractometers are used to determine the angles at which diffraction occurs in powder specimens. When the Bragg diffraction condition is satisfied by some set of crystallographic planes in powder specimens, diffraction patterns can be observed using one diffractometer. The diffraction pattern is a distribution of peaks with intensity I(2*θ*) at various angle positions 2θ*,* characterized by the maximum peak height, the dispersion of the distribution (full-width at half-maximum and integral breadth), by the line shape factor, and the integrated intensity (Figure 2.2). The reflection angle position 2*θ* is related to the lattice spacing d of the reflecting plane hkl (the orientation and interplanar spacing of the planes are defined by the three integers h, k, l, called indices) and to the wavelength λ. The peaks are plane-indexed in the diffraction pattern for a polycrystalline specimen of iron (Figure 2.2). Each reflection is fully defined when we know the d-spacing, the intensity (area under the peak) and the indices h, k, l. If we know the d-spacing and the corresponding indices we can calculate the dimension of the unit cell. On the other hand, the peak position can help us in the space group determination (2*θ*/absent reflection) and phase identification (*d*/*I*).

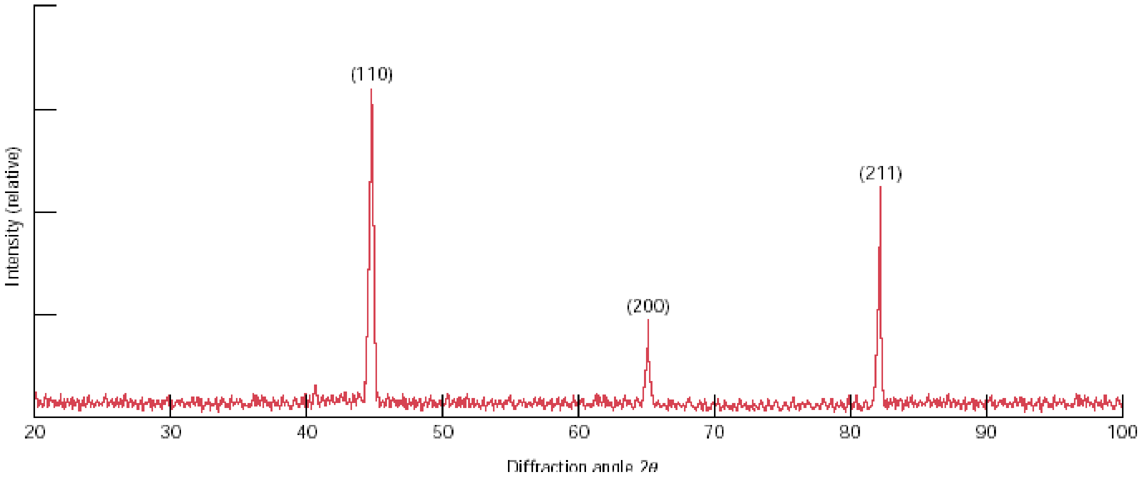

Figure 2.2 Diffraction pattern for polycrystalline α-iron. [1].

The intensity of the peaks can be used for the determination of the phase abundance, reaction kinetics, crystal structure analysis (whole pattern), Rietveld refinement (whole pattern), phase identification, preferred orientation, and texture analysis. The width, breadth and shape of the peaks can give us information about microstructure (crystallite size, size distribution, lattice distortion, structural defects, dislocations, compositional gradients) and crystallite growth kinetics.

The XRD patterns of sintered samples were collected at room temperature using a Rigaku D/max-B diffractometer (CuK_{α}, 2θ=20-70°, step 0.02°, 1 s/step).

2.3 Microstructural characterization

The microstructure of the sintered specimens was investigated using one scanning electron microscope (SEM). The compositional analysis of selected areas was determinated by energy dispersive spectroscopy (EDS).

Scanning electron microscopy (SEM) is one of the most versatile methods available for the microstructural characterization of solid objects. Electron microscopy takes advantage of the wave nature of rapidly moving electrons. The SEM uses electrons for imaging, such as a light microscope use visible light. Whereas visible light has wavelengths from 4,000 to 7,000 Angstroms, electrons accelerated to 10,000 KeV have a wavelength of 0.12 Angstroms. The advantages of SEM over light microscopy include greater magnification (up to 100,000X) and much greater depth of field [2].

In the SEM, the image is formed scanning point-to-point the sample surface with the electron beam. Various types of interactions between electron beam and specimen allow the local characterization of different aspects of the material such as chemical composition, crystallography, topography, atomic number distribution, electrical conductivity, etc.

When the specimen is bombarded with electrons over a very small area, electrons may be elastically reflected from the specimen, with no loss of energy. Electrons may also be absorbed by the specimen and give rise to secondary electrons of very low energy, together with X- rays, or even give rise to the emission of visible light (cathodoluminescent effect). Electrons may also give rise to electric currents within the specimen. All these signals can be used to characterize one material.

The most widely utilized signal produced by the interaction of the primary electron beam with the sample is the secondary electron emission signal. Secondary electrons are low energy electrons (energy lower than 50 eV) ejected from the sample as a result of inelastic collision with the electron beam. Due to their low energy, these electrons originate within a few nanometers from the surface. This is most useful for examining the surface structure and gives the best resolution image of any of the scanning signals. Depending on the initial size of the primary beam and conditions such as composition of sample, accelerating voltage, position of specimen relative to the detector, a secondary electron signal can resolve surface structures down to the order of 10 nm or better.

The topographic contrast is dependent on the degree of absorption of electrons by the sample before they reach the detector. Although an equivalent number of secondary electrons might be produced as a result of collisions between the primary electron beam and the specimen, secondary electrons that are prevented from reaching the detector will not contribute to the final image and these areas will appear as shadows or darker. The orientation of surface features influences the number of electrons that reach the secondary electron detector, which creates variations in image contrast that represent the sample's surface topography. Also, the higher the angle of incidence of the beam with the sample the smaller interaction volume and more secondary electrons will be emitted. Thus steep surfaces and edges tend to be brighter than flat surfaces resulting in images with good three-dimensional appearance. The ability of the secondary electron image to show the surface topography of a rough specimen is one of the most striking features of this method.

In addition to the secondary electrons, backscattered electrons can also be detected. Backscattered electrons are mainly used to detect contrast between areas with different chemical compositions, since the number of produced backscattered electrons increases with increasing atomic number of the specimen. Backscattered electrons are produced by the elastic interactions between the sample and the incident electron beam. These high energy electrons (energy greater than 50 eV) emerge nearly 180 degrees from the illuminating beam direction and can escape from much deeper than secondary electrons. The high penetration capability and big interaction volume are responsible for a small spatial resolution. So, the efficiency of emitting of backscattered electrons is proportional to the material's mean atomic number, which results in image contrast as a function of composition - higher atomic number materials appear brighter than low atomic number materials [2].

Chemical analysis is also obtained using an energy dispersive x-ray spectrometer with the SEM. The combined use of energy dispersive spectroscopy (EDS) and scanning electron microscopy (SEM) is a routine method of analytical electron microscopy enabling both qualitative and quantitative chemical analysis of interfaces with high resolution. Hence the use of EDS is indispensable in measuring the energy and intensity distribution of X-ray signals generated by the electron beam striking the surface of the sample. The elemental composition at a point, along a line, or in a defined area can be easily determined to a high degree of precision (~0.1 wt. %) [2].

The preparation of samples for observation followed a normal procedure including polishing and thermal etching. Sintered pellets were polished using diamond paste, with decreasing particle size of 6, 3, and 1 down to 0.25 μm, and then thermally etched at 1480^{o}C for 2 h to obtain a good resolution of major microstructural features. The average grain size for selected samples was determined by the linear intercept method using SEM photomicrographs.

2.4 Impedance spectroscopy

The transport properties of selected samples were analysed by impedance spectroscopy in air.

A.c. impedance analysis can be used to estimate the total resistivity of one material and at the same time to separate the bulk and grain boundary contributions. In this method, the complex impedance of a specimen is measured within a large range of frequencies and plotted as the imaginary part of the impedance (Z'') versus the real part (Z'). Actually, as under normal circumstances the imaginary part is negative, normal plots correspond to representations of -Z'' versus Z'.

The spectrum usually consists of several semicircles which are assigned to an equivalent circuit consisting of lumped *RC* elements. An idealized equivalent circuit for ceramic oxides corresponds to the complex impedance plot in Figure 2.3.

For ceramic oxides the low-frequency semicircle is due to electrode dispersion, the intermediate frequency circle is due to the grain boundaries and the high-frequency semicircle is attributed to the bulk behaviour. The electrodes are assumed to be partially blocking and are represented in the equivalent circuit by the double layer capacitance, *Ce*, and the charge transfer resistance, *Re.* The ideal description for bulk grain and grain boundaries is often more complicated as in some cases these elements might appear both in parallel and in series, as mentioned in the previous chapter [3]. However, for samples with significant amounts of secondary phases along the grain boundaries, as in the present work, the equivalent circuit shown in Figure 2.3 is quite appropriate.

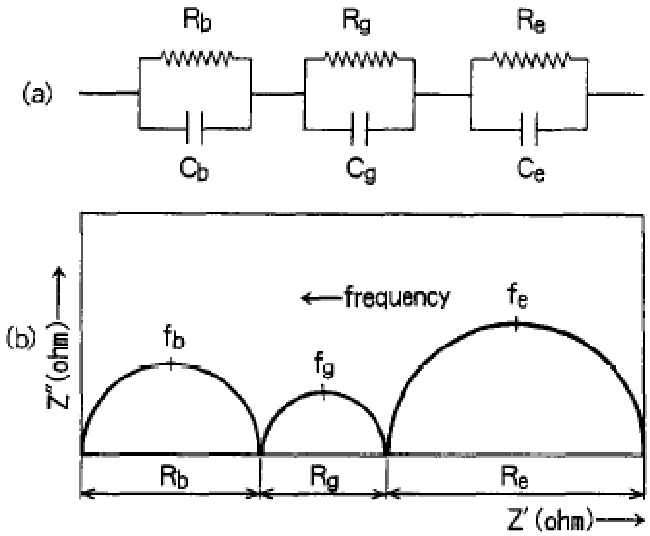

Figure 2.3 Idealized equivalent circuit (a) and complex impedance diagram for a two phase ceramic electrolyte (b). R_b, R_g and R_e denote the electrical resistivity due to the bulk, grain boundary and electrode, respectively [3].

Since the relaxation frequencies and capacitance values for bulk and grain boundary contributions are different by several orders of magnitude, it is possible to separate them in the low temperature range. However, due to the limited frequency range of the equipment and temperature dependence of the grain interior and grain boundary contributions, most single temperature spectra fail to show well resolved arcs for bulk, grain boundary and electrode contributions at the same time. The impedance measurements are made usually in wide temperature ranges in order to avoid misunderstanding in the interpretation of data.

The bulk and grain boundary resistances of sintered pellets were obtained by ac impedance spectroscopy in air using one HP Impedance Analyzer (HP4284A precision LCR meter). Symmetrical platinum electrodes were applied on both surfaces of the pellet using Pt paste and these were fired at 1000°C during 2 h. The electrical measurements were performed from 200°C to 1000°C, in the range of 20–10^6 Hz, with an excitation voltage of 500 mV. The complex impedance spectra of these materials usually comprised two or three well defined arcs. Data obtained in this manner were used for the determination of the ionic conductivity of all samples. In order to obtain a high resolution of impedance arcs attributed to the bulk and grain boundary contributions, samples with low length to electrode surface area (L/S) were used [4]. Impedance measurements were performed with samples with length to electrode surface area ratio L/S ~ 0.35 cm^{-1}.

Results were fitted to equivalent circuits using the ZView software package (Version 2.6b, 1990-2002, Scribner Associates). Representative examples obtained with the CGOLSL-0.5% sample (impedance spectra fitted with the corresponding equivalent circuit) are plotted in Figure 2.4.

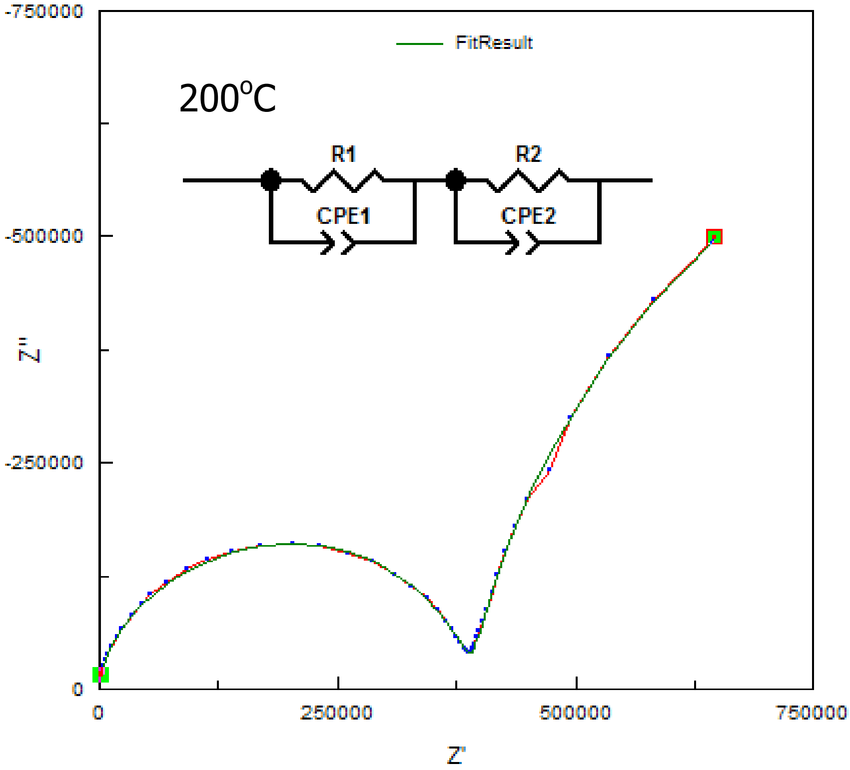

(a)

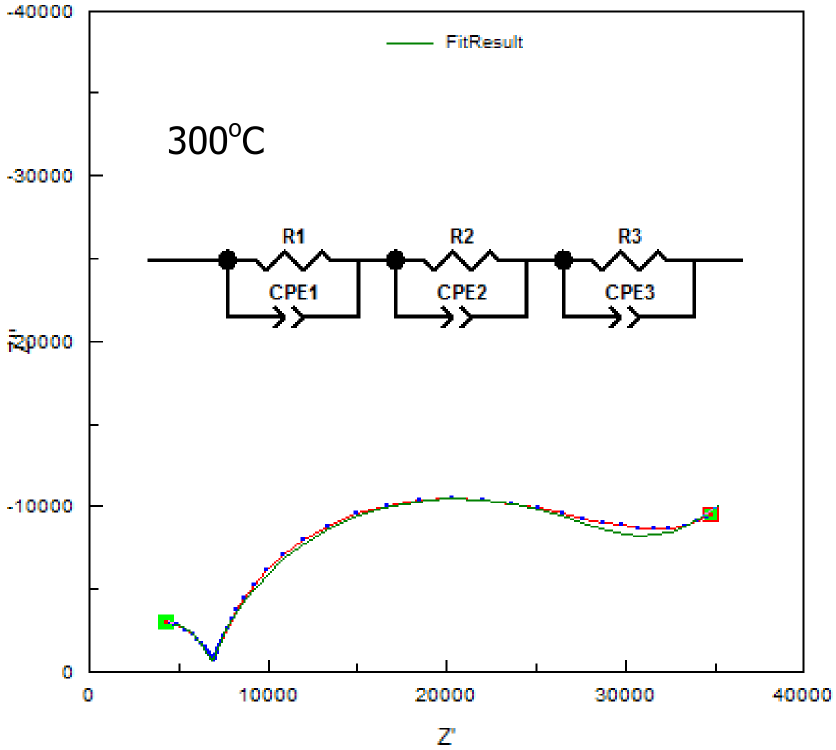
FitResult
300°C
R1
R2
R3
CPE1
CPE2
CPE3
-40000
-30000
-20000
-10000
0
Z''
0
10000
20000
30000
40000
Z'

(b)

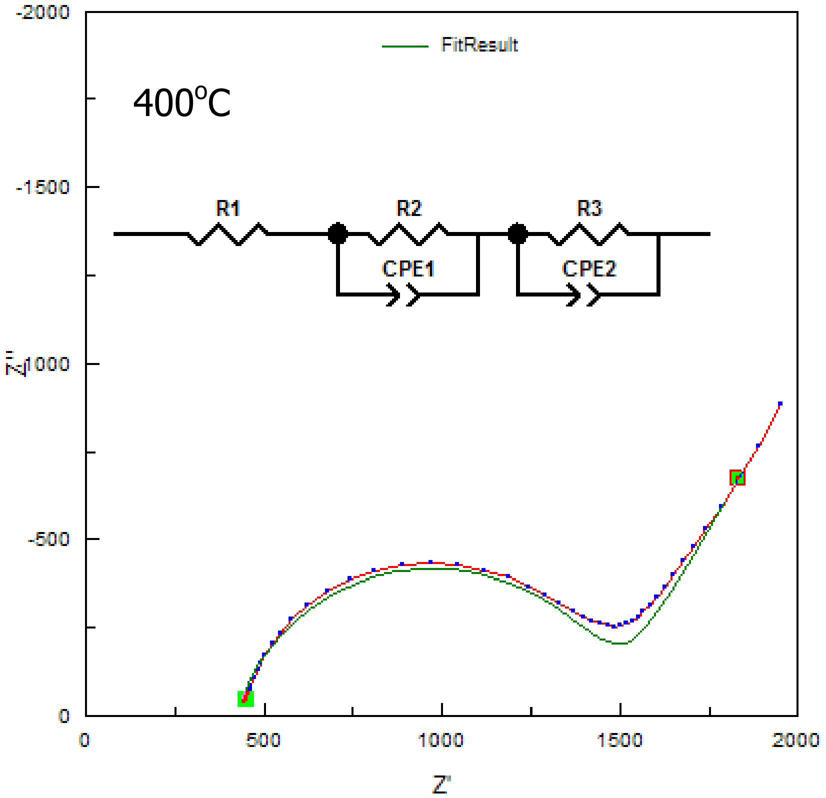
FitResult
400°C
R1
R2
R3
CPE1
CPE2
-2000
-1500
-1000
-500
0
Z''
0
500
1000
1500
2000
Z'

(c)

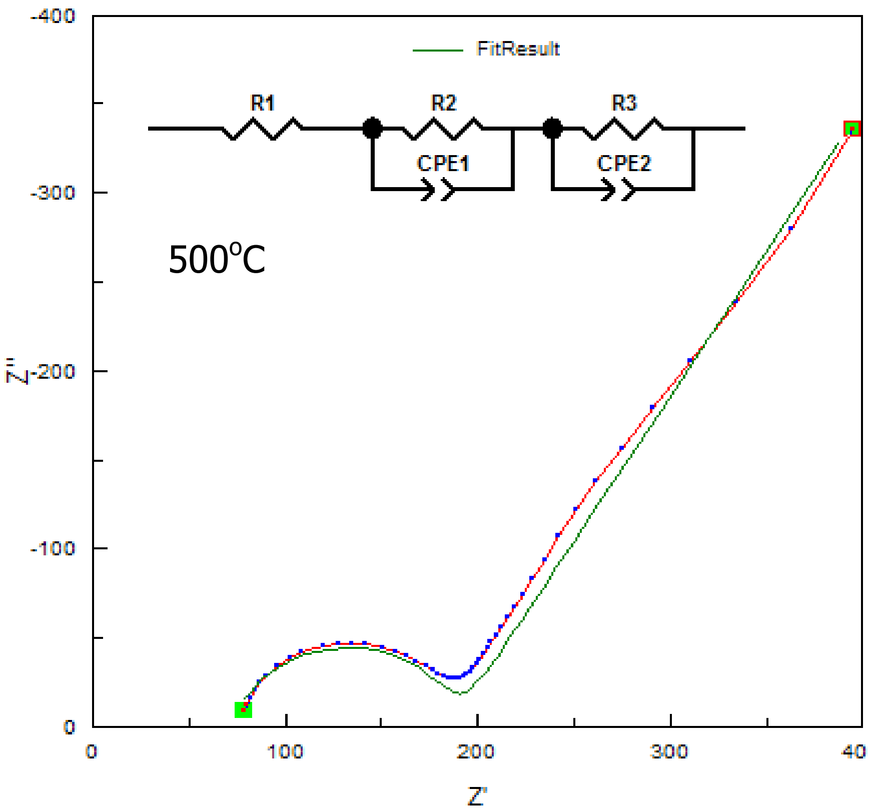
-400
-300
-200
-100
0
Z''
0
100
200
300
40
Z'
FitResult
R1
R2
R3
CPE1
CPE2
500°C

(d)

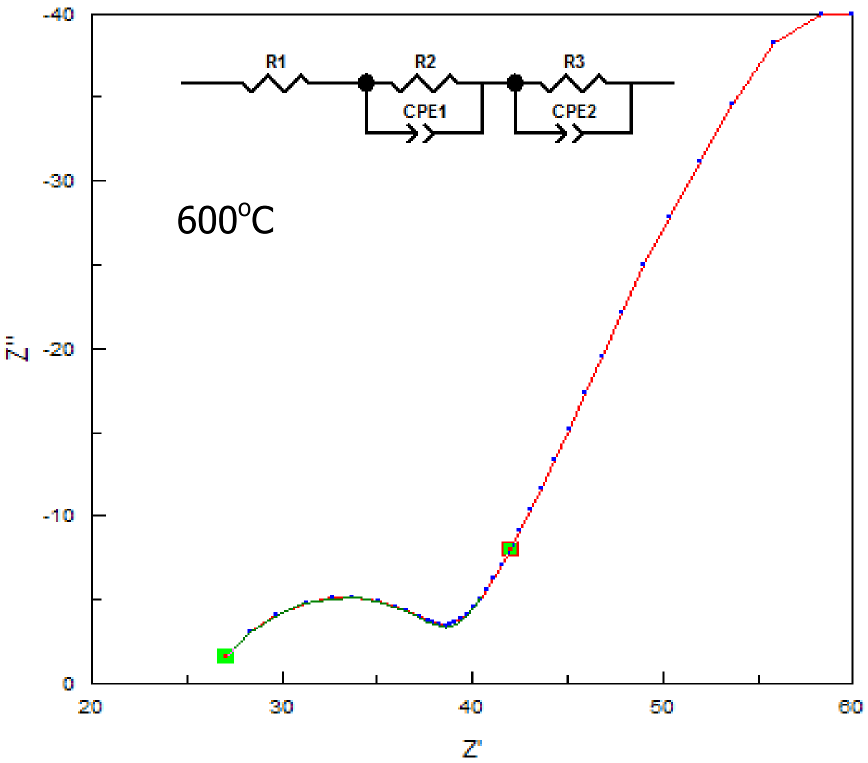
-40
-30
-20
-10
0
Z''
20
30
40
50
60
Z'
R1
R2
R3
CPE1
CPE2
600°C

(e)

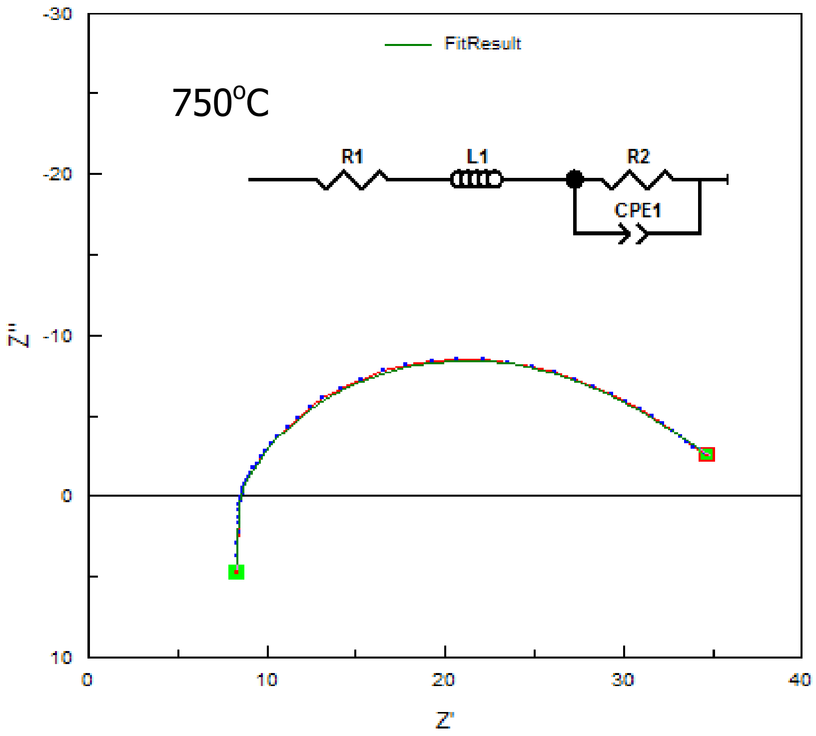

(f)

Figure 2.4 (a)-(f) Typical impedance spectra of one CGOLSL-0.5% sample obtained at different temperatures (shown inside figures)

In the high temperature range (1000 – 700°C) only the total resistivity of the specimens can be obtained from the intercept of the spectra with the Z' axis. However, the grain boundary and bulk arcs become more detectable and resolved in the low temperature range (from 700 to 200°C), allowing estimation of grain boundary and bulk contributions to the total resistivity of materials.

The constant phase elements (CPE) shown in the previous figure were used instead of resistors in the equivalent circuits since the arcs associated with bulk, grain boundary and electrode responses, were slightly depressed. Constant phase elements successfully fit depressed arcs which can be ascribed to the presence of a distribution of relaxation frequencies due to non-uniform properties or surface roughness of the material [5].

In the spectra obtained at 750°C one inductive element (L) was introduced to take into consideration the portion of the spectra crossing the Z' axis. This is not characteristic of the material. Instead, this type of feature at high temperature is usually related to the non-shielded measuring circuit under the influence of the furnace electrical load.

2.5 References

1 W. D. Callister, Jr., Materials Science and Engineering An Introduction, John Wiley & Sons, 4th edition, 1997

2 J. Goldstein, D. Newbure, D. Joy, C.Lyman, P. Echlin, E Lifshin, Scanning electron microscopy and X-ray microanalysis, Kluwer Academic/Plenum Publishers, 3rd, edition, New York, 2003

3 Hideaki Inaba, Hiroaki Tagawa, Solid State Ionics 83 (1996) 1- 16

4 L.Navaro, F.Marques, J. Frade, Journal of the Electrochemical Society 144 (1997) 1

5 Daria Vladikova, Proceedings of the International Workshop "Advanced Techniques for Energy Sources Investigation and Testing" 4 – 9 Sept. 2004, Sofia, Bulgaria

Chapter 3

3 Results and Discussion

In this chapter the results of this work will be presented and discussed. Considering the relevance of this part of the thesis and the overall range of compositions and experiments, some introductory comments are provided to explain the entire organization of this chapter.

Firstly, the sintering behaviour of ceria-based ceramics in the presence of silica or silica and lanthanum oxide is presented. Details on attempts to improve densification at moderate sintering temperatures, namely using high energy milling, are provided here. Although not entirely satisfactory, a set of conditions was established able to provide appropriate samples for ulterior electrical characterization.

The microstructural and structural characterization of the samples was based on XRD, SEM and EDS results. Special attention was given to interaction between silica, La_2O_3 and CGO-based materials. The likelihood of incomplete high temperature reactions justified the preparation of samples starting from major oxide constituents or from likely reaction products (e.g., CGO and apatite) to indirectly assess the role of this aspect.

The electrical properties of all ceramics were evaluated by means of impedance spectroscopy. Although mostly in the presence of composite materials, the entire analysis was centred in a classical discussion on bulk and grain boundary contributions. In fact, with a clearly dominant CGO-based phase, this simplified type of analysis seemed fully justified. The influence of the lanthanum addition on bulk and grain boundary resistivity of silica-containing CGO ceramics is thus discussed and related with microstructural and compositional features.

3.1 Sintering and densification

Several attempts were made to establish the most effective sintering conditions for the ceria-based ceramics. The values of sintering time/temperature, pressure and time for ball-milling are listed in Table 3.1. They describe briefly the preparation parameters exploited in the fabrication of these ceramics. It was surprising that the relative density of CGO-based ceramics sintered at 1500°C did not exceeded 86.3% of the theoretical density. Considering that the commercial CGO powder with submicrometric particles was used as raw material, a high level of reactivity and sinterability was expected. The poor sinterability of this powder can only be attributed to the existence of agglomerates. Ball-milling was used to reduce the level of agglomeration but an acceptable density was achieved (in the order of 92% densification) only when the sintering temperature reached 1650°C (Table 3.1).

Table 3.1. Sintering conditions and density of the samples

Attempt	Sintering T, °C	Sintering time, h	Pressure, MPa	Ball-milling, h	Composition	Relative density, %
1	1600	2	20	-	CGO	84.9
					CGOLSL-0.5%	78.6
2	1500	4	180	-	CGO	86.3
					CGOLSL-0.5%	76.9
3	1550	4	180	2	CGO	86.6
					CGOLSL-0.5%	81.6
4	1600	4	180	4	CGO	89.7
					CGOLSL-0.5%	87.8
5	1650	4	220	4	CGO	93.7
					CGOLSL-0.5%	93.2

The mechanical activation of powders is widely used to improve the sinterability of green compacts [1,2]. The mechanical activation (M/A) of the powders before sintering, in addition to isostatic pressing, was used as an attempt to increase the density of sintered ceramics. Accordingly, the powders were mechanically activated during 150 min in one nylon container, and the pellets were firstly shaped uniaxially and than pressed isostatically. As during mechanical activation the powder was contaminated by nylon from the jar, in order to eliminate this impurity, annealing of the powder compacts took place at an early stage of heating during the sintering procedure. The consequence of such steps in the preparation procedure of one of these ceramics is presented in Table 3.2. The mechanically activated isostatically powder pressed at 320 MPa gave almost the same result as the simplest preparation procedure described in the experimental part of work (see previous chapter).

Assuming this, all samples presented in this study were sintered at 1650°C during 4 hrs after pressing uniaxially at 220 MPa. Such high temperature facilitates interdiffusion between components leading to side effects such as formation of unexpected phases. However, this sintering route was adopted since for providing dense ceramics without open porosity.

Table 3.2. Preparation parameters and relative density of samples

№	M/A	Pressing				Annealing	Sintering	Annealing and sintering steps	Relative density,%, (CGOLSL -0.5% sample)
		Uniaxially		Isostatically					
		P, MPa	Green density, %	P, MPa	Green density, %				
1	150 min	125	57	-	-	350°C, 15 min	1650°C, 4h	together	90.5
2		375	63	250	63	350°C, 15 min	1650°C, 4h	together	Broken samples
3		375	63	-	-	400°C, 7h	1650°C, 4h	separately	91
4		62	54	320	61	400°C, 7h	1650°C, 4h	separately	93.3
5		62	54	320	61	400°C, 5h	1650°C, 4h	together	91.5
6*	-	220	60	-	-	-	1650°C, 4h	-	93.5

The short designations and microstructural features of the ceramics used in this investigation are shown in Table 3.3. The meanings for LSL, LSH and LSE were already presented, corresponding to a low, high or intermediate lanthanum oxide/silica ratios (see chapter 2). The extension "-ox" means that the sample was prepared directly from a mixture of the apatite constituent oxides. In the absence of this extension, a pre-synthesized apatite was used as precursor. The percentages indicated in the short designation (0.5 or 5%) correspond to the total amount of additions to the base CGO powder.

Table 3.3. Composition, relative density and grain size of the samples used in investigation.

Composition				Relative density, %	Average grain size of the CGO, µm
Main component	Additive	Content, mol %	Abbreviation		
CGO	none		CGO	93.8	4.70
CGO	SiO_2	0.5%	CGOSi-0.5%	93.9	3.73
CGO	SiO_2	5%	CGOSi-5%	92.9	2.23
CGO	$La_{9,33}Si_6O_{26}$	0.5%	CGOLSL-0.5%	93.5	4.23
CGO	La_2O_3, SiO_2	0.5%	CGOLSL-0.5%-ox	92.9	3.97
CGO	$La_{9,33}Si_6O_{26}$	5%	CGOLSL-5%	93.4	2.77
CGO	La_2O_3, SiO_2	5%	CGOLSL-5%-ox	91.9	2.73
CGO	$La_{9,83}Si_6O_{26,75}$	0.5%	CGOLSE-0.5%	93.4	4.04
CGO	La_2O_3, SiO_2	0.5%	CGOLSE-0.5%-ox	92.9	3.78
CGO	$La_{9,83}Si_6O_{26, 75}$	5%	CGOLSE-5%	90.8	3.01
CGO	La_2O_3, SiO_2	5%	CGOLSE-5%-ox	90.9	2.85
CGO	$La_{10}Si_6O_{26,75}$	0.5%	CGOLSH-0.5%	93.5	3.39
CGO	La_2O_3, SiO_2	0.5%	CGOLSH-0.5%-ox	92.3	3.22
CGO	$La_{10}Si_6O_{26, 75}$	5%	CGOLSH-5%	88.6	2.56
CGO	La_2O_3, SiO_2	5%	CGOLSH-5%-ox	89.5	2.51

Samples of pure CGO had the highest grain size and relative density. Figures 3.1 and 3.2 describe the grain size and relative density of sintered specimens as a function of the level of silica and/or lanthanum oxide, or direct apatite additions. As one can see the introduction of silica leads to a considerable reduction in grain size and causes little effect on the density of gadolinium-doped ceria. Also, as the level of other additives is increased, the grain size of ceria-based ceramics becomes smaller as well as the relative density of sintered specimens (Figures 3.1 and 3.2).

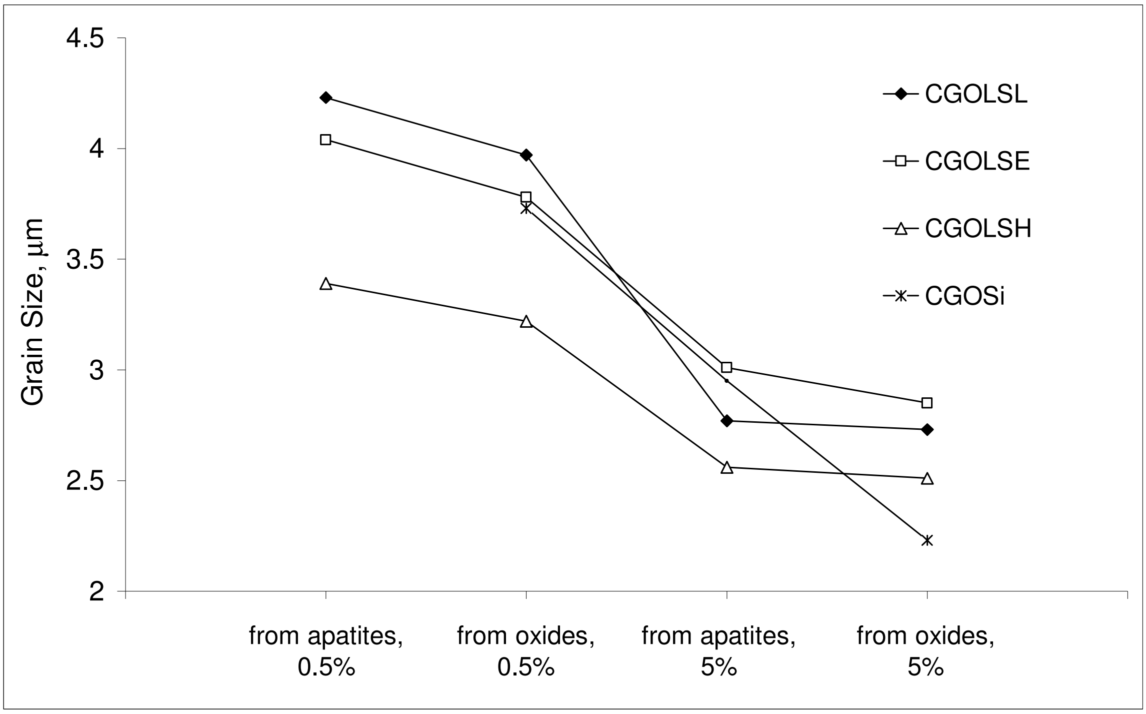

Figure 3.1 Grain size of sintered specimens as a function of level of silica and/or lanthanum oxide, or direct apatite additions

The suppressed grain growth can be explained in terms of a pinning effect of the second phase on the grain growth process during sintering of these ceramics. As the grain boundary moves over the foreign particle, the grain boundary area is reduced by an amount equal to the cross-sectional area of the particle. The surface area and the surface energy must increase if the particle is to be pulled away. Thus, foreign particles may exert a restraining force on the grain boundary movement during the sintering process [3]. Obviously, this is not the only possible active sintering mechanism. As an example, the formation of a liquid phase frequently acts as a sintering aid.

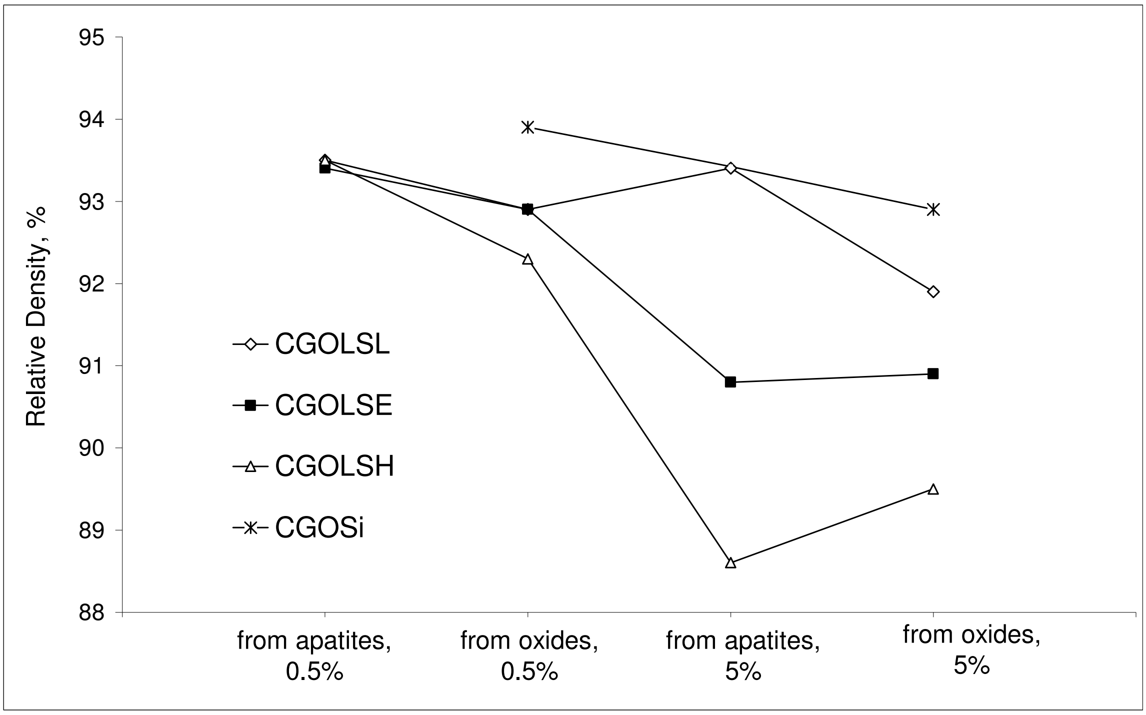

Figure 3.2 Relative density of sintered specimens as a function of level of silica and/or lanthanum oxide, or direct apatite additions

It can be noticed also that the higher the concentration of La_2O_3 introduced in CGO, the lower the grain growth during the sintering process. This suppressed grain growth in the presence of lanthanum oxide can also be explained by a solute drag model due to a space charge effect. The grain boundary migration during the sintering process is inhibited by the space charge layer formed by the dopant segregation in the grain boundary region. This was observed in systems such as Y-, Gd- and Sm-doped ceria [4-7]. Besides, partial dissolution of La^{3+} leads to distortion of ceria lattice, confirmed by XRD, and apparently decreases the cation mobility during sintering, resulting in a smaller grain size and lower densification rate [7].

An introduction of lanthanum oxide and 5 mol% silica decreases the sinterability of the CGO ceramics, while a small amount of silica (0.5 mol%) causes almost no effect on the densification of ceria-based ceramics. An investigation of Zhang *et. al.* on the role of silica content on the densification behaviour of ceria-based ceramics showed that while a small amount of silica is expected to enhance the densification rate because of the already mentioned liquid phase sintering effect [8], a high content of silica causes a detrimental effect on the densification process of CGO(20). The latter case was explained as a pinning effect of this second phase [9].

Overall, the final densification of these ceramics was below expectation, even after significant changes in the processing route. The influence of the low density and small grain size of these ceramics on the electrical properties of samples will be discussed later in this chapter.

3.2 Structural and microstructural characterization

X-ray powder diffraction (XRD) was used to identify the phase composition of sintered specimens. Formation of gadolinium silicate, partly unexpected, was clearly observed in CGOSi-5% samples, as indicated by XRD, Fig. 3.3. The XRD patterns of the CGO and silica-containing ceramics were refined using WinPLOTR and FullProf suite to identify the corresponding phases and to obtain the lattice parameters of phases represented in Table 3.4. The refinement profiles can be found in Appendix I.

Table 3.4. Refined lattice parameters (in Å) of CGO and gadolinium silicate phases in CGO, CGOSi-0.5% and CGOSi-5% samples

Lattice parameter of CGO		Lattice parameters of mixed apatite phase		
Composition	Lattice parameter, a	Composition	Lattice parameter, a	Lattice parameter, c
pure CGO(20)	5.4328(2)	$Gd_{9.33}(SiO_4)_6O_2$ [10]	9.4264	6.8444
		$Ce_{9.33}(SiO_4)_6O_2$ [11]	9.598	7.106
CGOSi-0.5%	5.4265 (1)	CGOSi-0.5%	9.4690(42)	6.8739(54)
CGOSi-5%	5.4216(1)	CGOSi-5%	9.4635(6)	6.8770 (7)

The decrease of the lattice parameters of CGO in silica-containing samples can be caused by the loss of gadolinium to the silica-based secondary phase due to lixiviation and consequent formation of the gadolinium apatite. The lattice parameters of the apatite phase in CGOSi-0.5% and CGOSi-5% specimens are large if compared to the lattice parameters of pure $Gd_{9.33}(SiO_4)_6O_2$. This is probably due to the formation of a solid solution based on $Gd_{9.33}(SiO_4)_6O_2$ and the metastable $Ce_{9.33}(SiO_4)_6O_2$ phase.

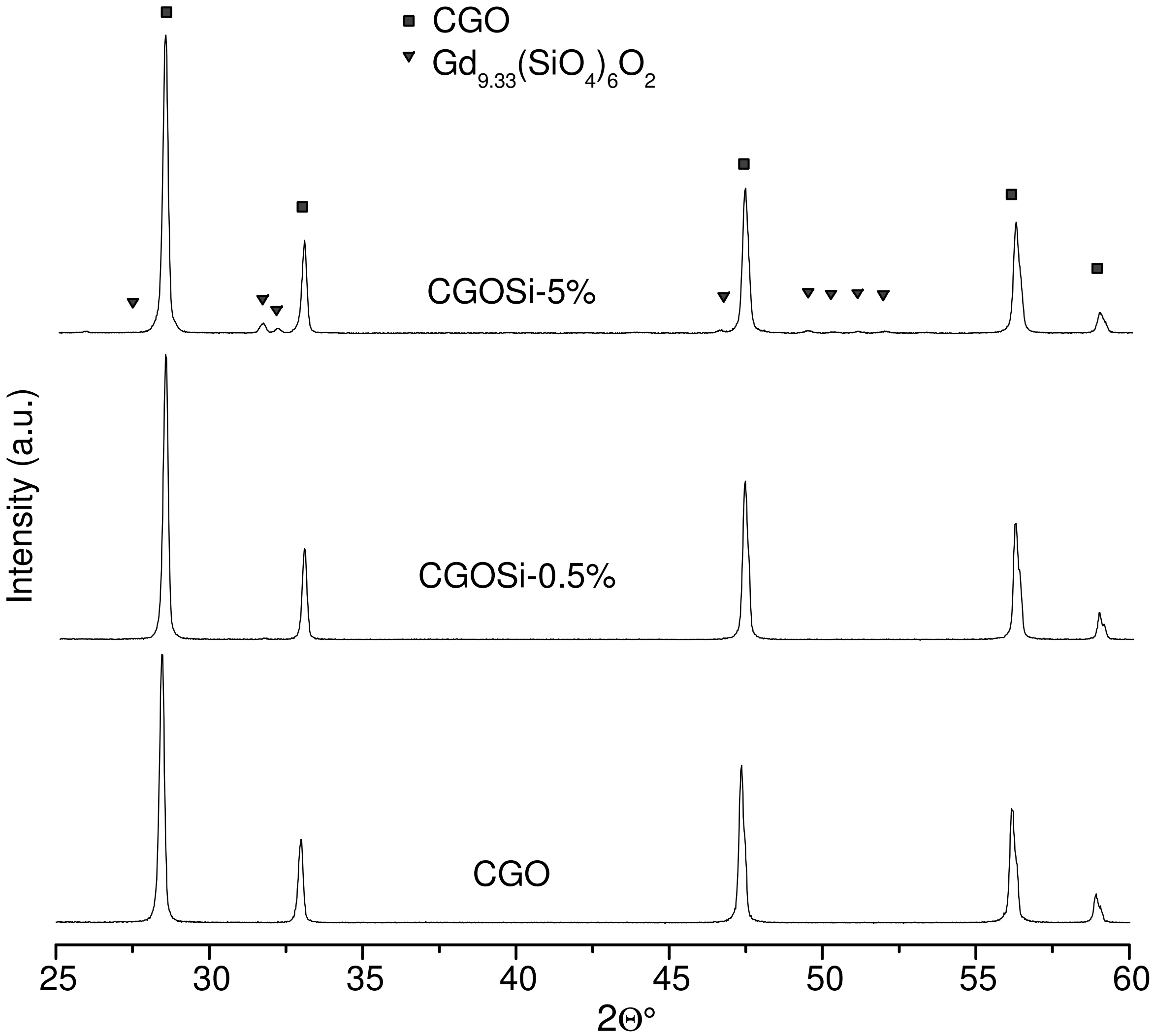

Figure 3.3 XRD patterns of the CGO, CGOSi-0.5% and CGOSi-5% sintered samples

As the formation of one $Gd_{9.33}(SiO_4)_6O_2$-based solid solution from reaction between silica and CGO was not anticipated, several CGOSi-5% samples were sintered at various temperatures in order to reveal the conditions corresponding to the formation of the former phase. XRD results of the CGOSi-5% specimens sintered in the temperature range from 1100°C to 1650°C showed that the formation of the $Gd_{9.33}(SiO_4)_6O_2$-based solid solution takes place at about 1100-1150°C (Figure 3.4). This means that lixiviation of gadolinium from CGO starts at quite low temperatures, but also that gadolinium oxide might be a good silica scavenging agent, as an alternative to lanthanum oxide.

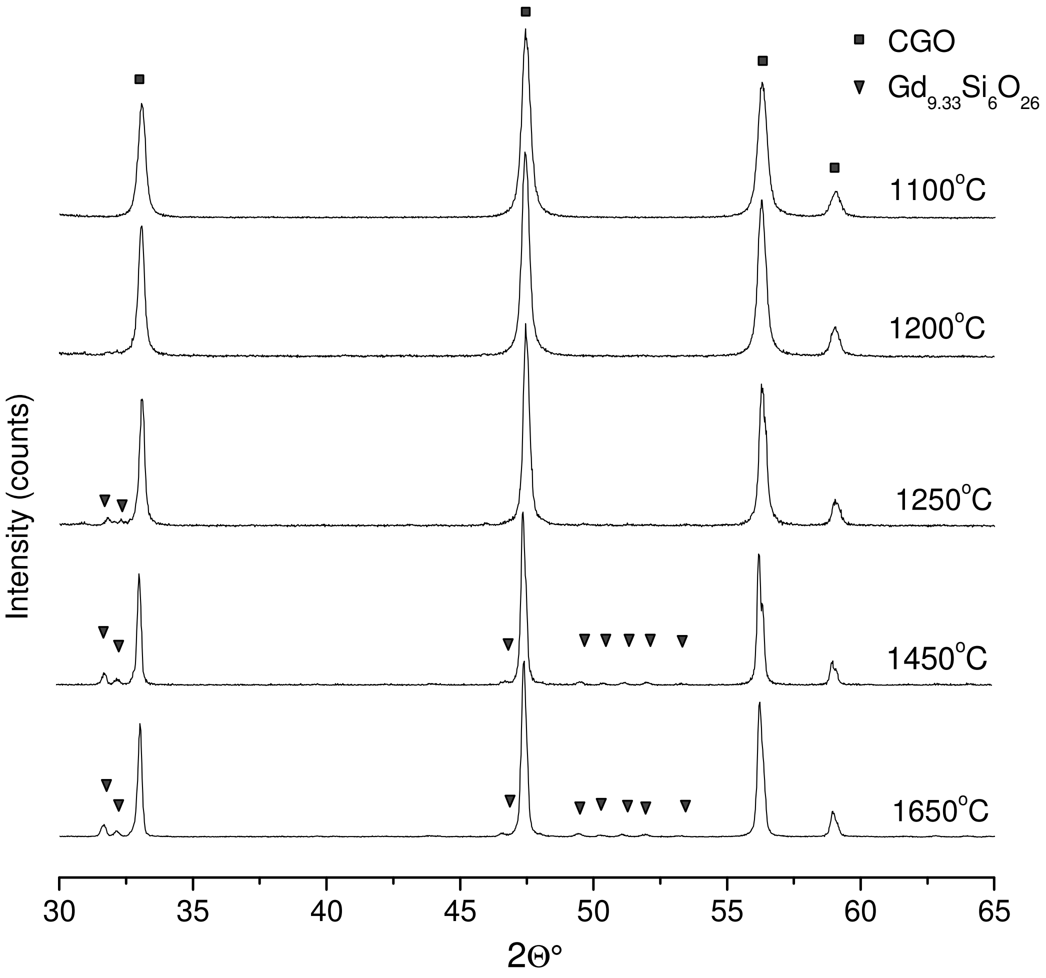

Figure 3.4 XRD patterns of the CGOSi-5% samples sintered in the temperature range from 1100°C to 1650°C

This result is coherent with data obtained by the U. Kolitsch *et al.* on the phase relationships in the ternary system Gd_2O_3-Al_2O_3-SiO_2. However, in this case formation of the $Gd_{9.33}(SiO_4)_6O_2$ was observed at 1400°C in alumina-free samples [12]. The present observation is somehow surprising since several previous studies undertaken to eliminate silica from gadolinium-doped ceria provided no clues for the formation of gadolinium apatite based solid solution in SiO_2-containing CGO ceramics, even in materials sintered at 1600°C [9]. Different SiO_2 precursors (wet chemical method using tetraethyl orthosilicate (TEOS) as precursor [8, 9, 13] or dilute SiO_2 sol [14-17]) might explain the diversity of results. Also, in the case of low silica contents, negligible amounts of reaction products might be hardly identified by XRD. The formation of gadolinium apatite phase in our study was certainly facilitated by the exaggerated amount of SiO_2 used in some experiments as well as by the high sintering temperature adopted.

The micrographs of pure CGO and CGO with low content of silica samples are depicted in Figure 3.5

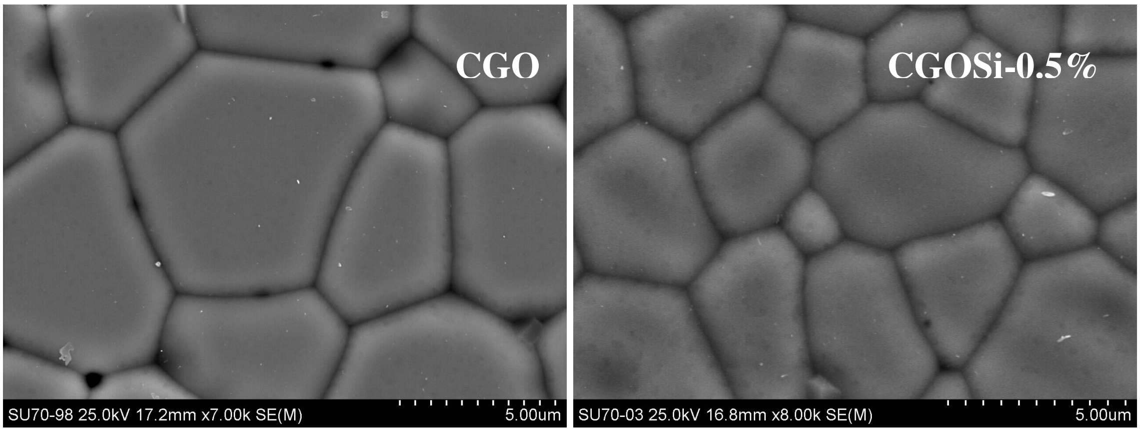

Figure 3.5 Microstructure of the pure CGO and CGOSi-0.5% samples

Pure CGO and CGOSi-0.5% show rather similar microstructure without open porosity, uniform grain size (slightly larger for CGO) and without any clear evidence of any second phase in the grain boundary region. As the level of silica is considerably small, thin silica films can be easily spread along the grain boundaries of CGO either free or combined with gadolinium as was detected by XRD. Such behaviour in the presence of low content of silica is common in the case of YSZ [18].

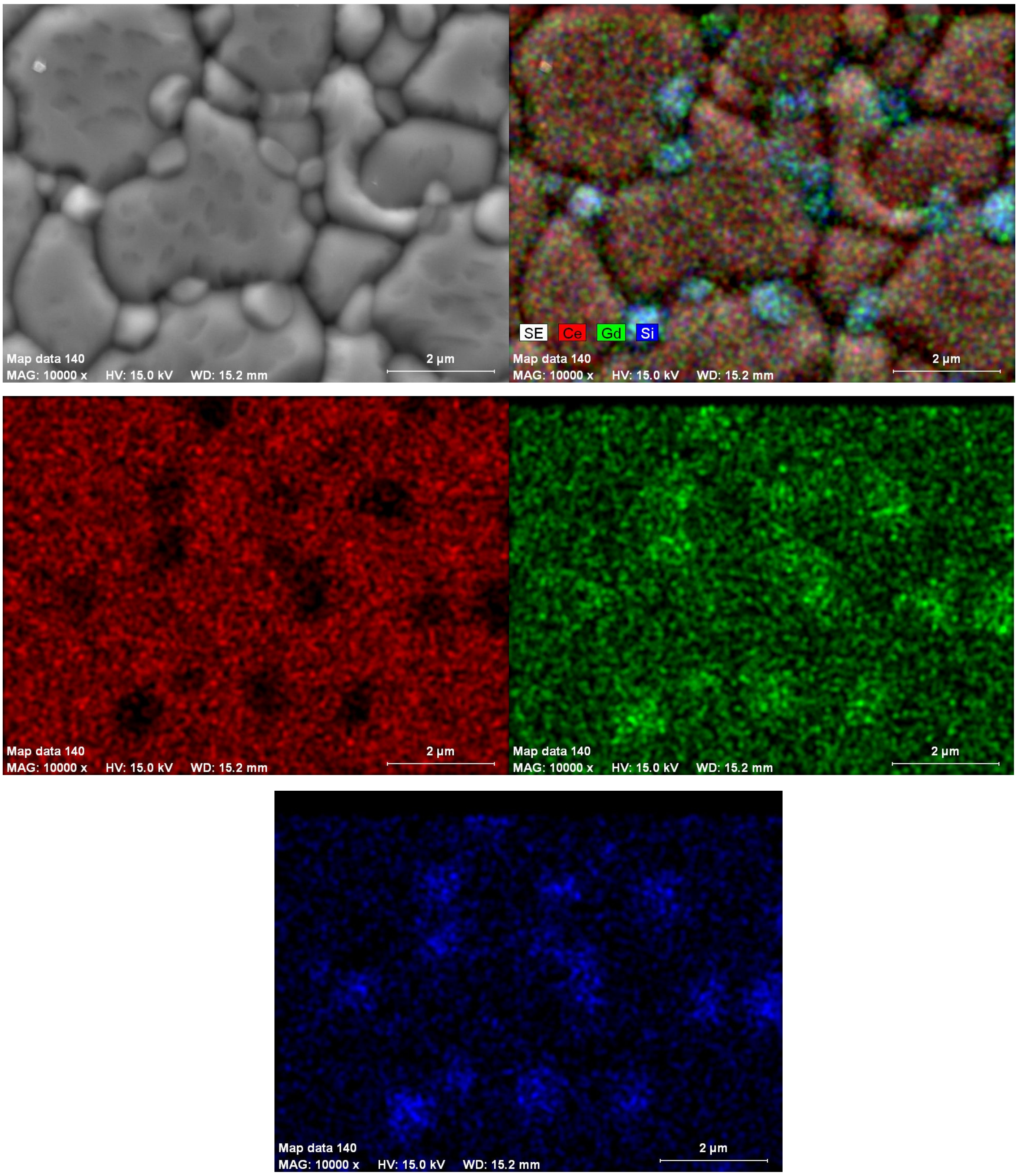

Figure 3.6 Microstructure and atomic number mapping of the CGOSi-5% ceramics

The microstructure of CGO with 5 mol% of silica phase shows a clearly composite material with the $Gd_{9.33}(SiO_4)_6O_2$ apatite phase located preferably at the grain boundaries of CGO, Figure 3.6. The formation of the $Gd_{9.33}(SiO_4)_6O_2$-based solid solution does not exclude the possible presence of thin siliceous layers along the grain boundaries of CGO ceramics. On the other hand, formation of the gadolinium apatite at high sintering temperatures clearly decreases the level of free silica along grain boundaries, acting as a silica scavenger agent.

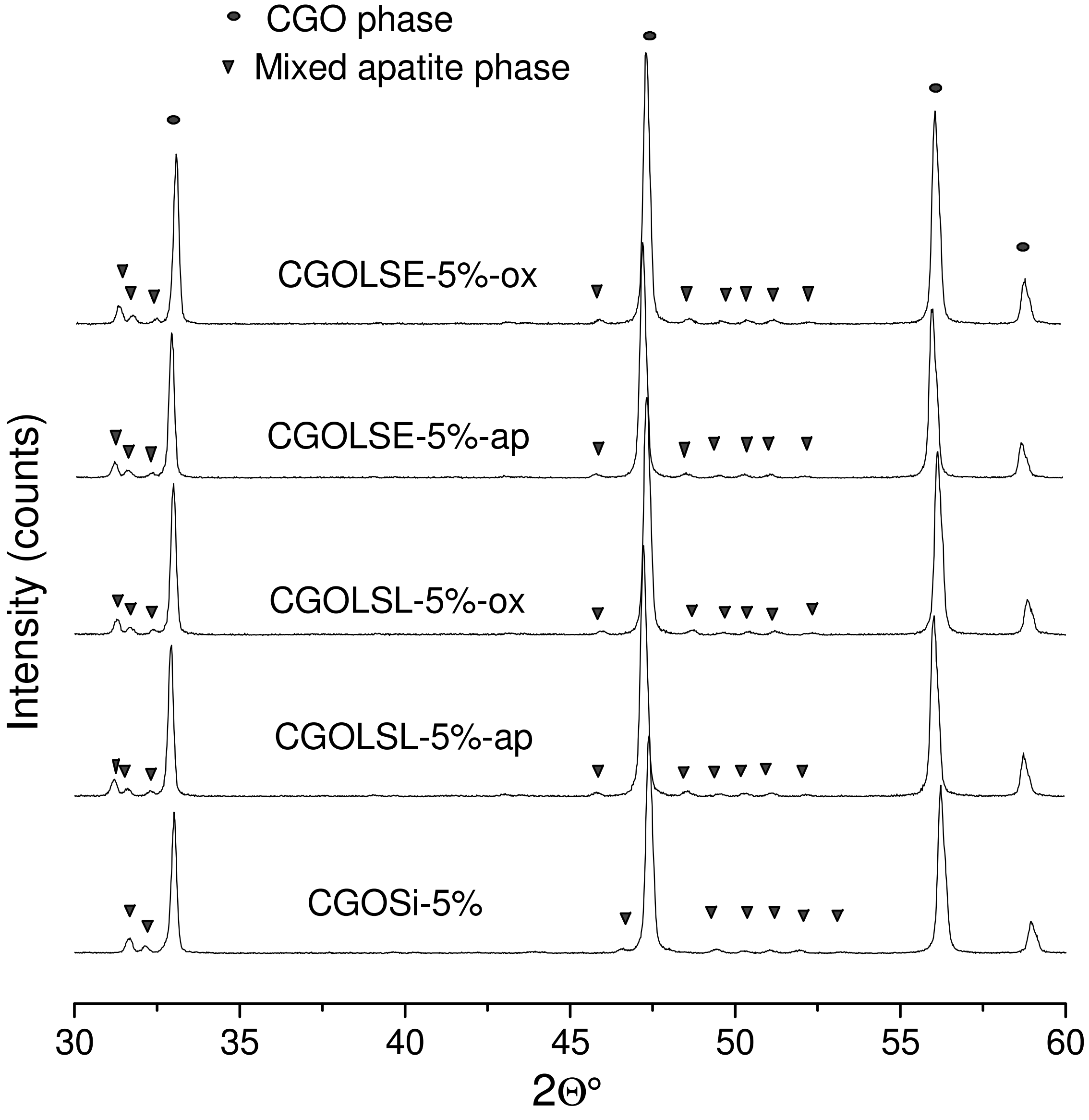

Figure 3.7 XRD patterns of the CGOSi-5% apatite-containing samples

Formation of one $La_{9,33}Si_6O_{26}$-based solid solution was detected by X-ray powder diffraction in the case of CGOLS-samples (Figure 3.7). The refined lattice parameters of CGO and secondary apatite phase in apatite-containing samples based on XRD data are presented in Table 3.5. The refinement profiles of presented samples can be found in Appendix I.

Table 3.5 Refined lattice parameters (in Å) of CGO and apatite based phases in CGO and apatite containing samples

Lattice parameter of CGO		Lattice parameters of mixed apatite phase		
Composition	Lattice parameter, a	Composition	Lattice parameter, a	Lattice parameter, c
Pure CGO(20)	5.4328(2)	$La_{9.31}(SiO_4)_6O_2$ [19]	9.699	7.125
		$Gd_{9.33}(SiO_4)_6O_2$ [20]	9.4264	6.8444
CGOLSL-0.5%	5.4270 (2)	CGOLSL-0.5%	9.5901(13)	7.0030(11)
CGOLSL-5%	5.4379(2)	CGOLSL-5%	9.5978(8)	7.0106(7)
CGOLSE-0.5%	5.4285(1)	CGOLSE-0.5%	9.4921(41)	7.0049(55)
CGOLSE-5%	5.4373(2)	CGOLSE-5%	9.5947(9)	7.0073(8)

In low silica content samples gadolinium oxide still tends to leave the CGO grains as can be seen from the decrease in the refined lattice parameters of the CGO-based phase in apatite-containing samples. However, the refinement of the lattice parameters of the apatite phase in these samples also showed that co-addition of lanthanum oxide and silica suppresses the formation of gadolinium silicate due to dominant reaction between silica and lanthanum oxide. On the other hand, in highly doped samples some La^{3+} dissolves in the ceria lattice, according to the enlarged lattice parameters of CGO in CGOLSL-5% and CGOLSE-5% samples. This shows that coexistence of all these species at high temperature promotes a strong interaction between constituents, exceeding by far the simple scavenging effect being exploited. Nevertheless, the tendency to combine silica with other species with formation of new phases is notorious, as expected.

Figure 3.8 shows SEM micrographs of typical apatite-containing ceramics after thermal etching during 1h at 1480°C. These microstructures illustrate the formation of the apatite phase preferably in triple points or as isolated grains along the grain boundaries of CGO ceramics.

The dominant characteristics of these microstructures are not influenced by the precursor's choice (lanthanum oxide, silica and CGO, or from the pre-synthesised apatite phase and CGO), although the grain sizes tend to be smaller in the case of single oxides as apatite precursors.

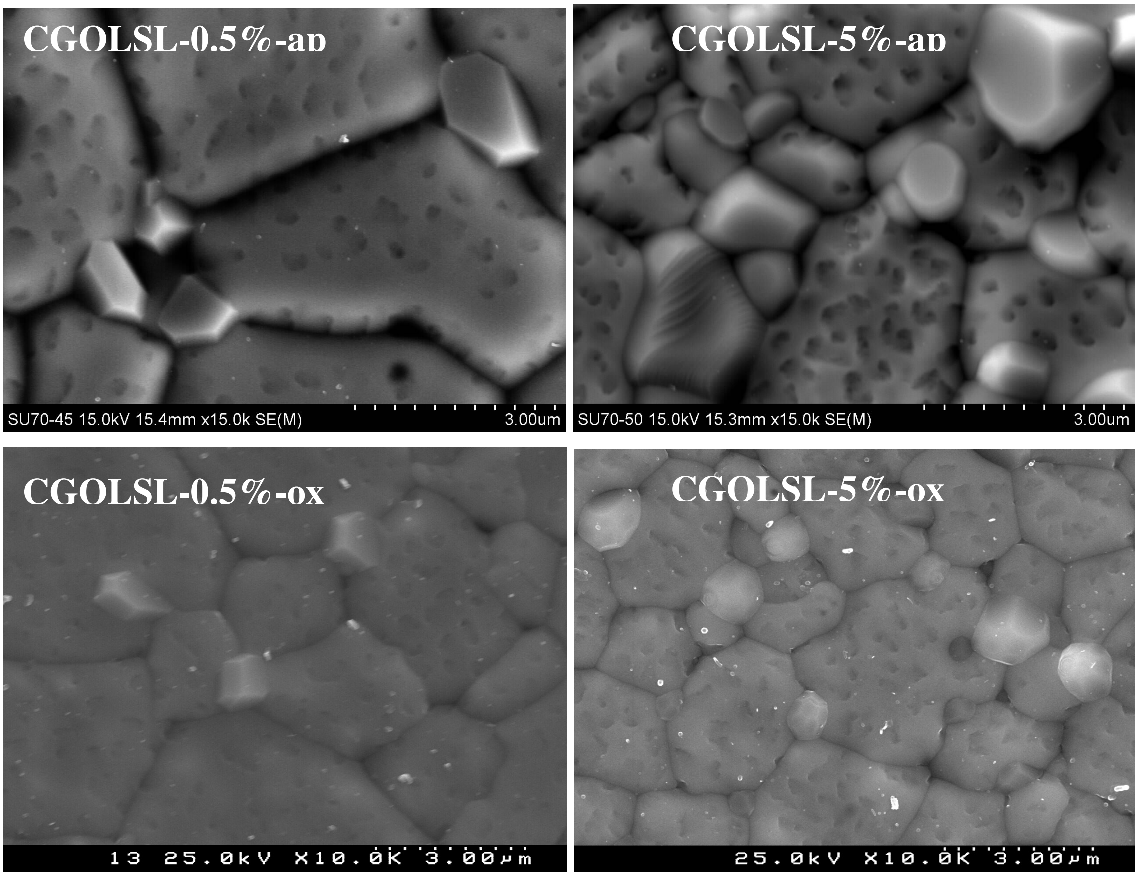

Figure 3.8 SEM micrographs of the CGOLSL-0.5% and CGOLSL-5% samples sintered from the various types of precursors (oxides or pre-synthesized apatite and CGO)

EDS analysis of samples, combined with XRD results already discussed, proved the formation of one $La_{9.33}(SiO_4)_6O_2$-based solid solution containing some gadolinium, Figure 3.9. Typical atomic number maps and EDS spectra are presented in Figure 3.10 for the CGOLSL-5%-ox sample. EDS mapping clearly indicates that silica, combined with lanthanum, tends to segregate in triple points of the CGO-based matrix. However, some silica is also spread throughout the ceria grains.

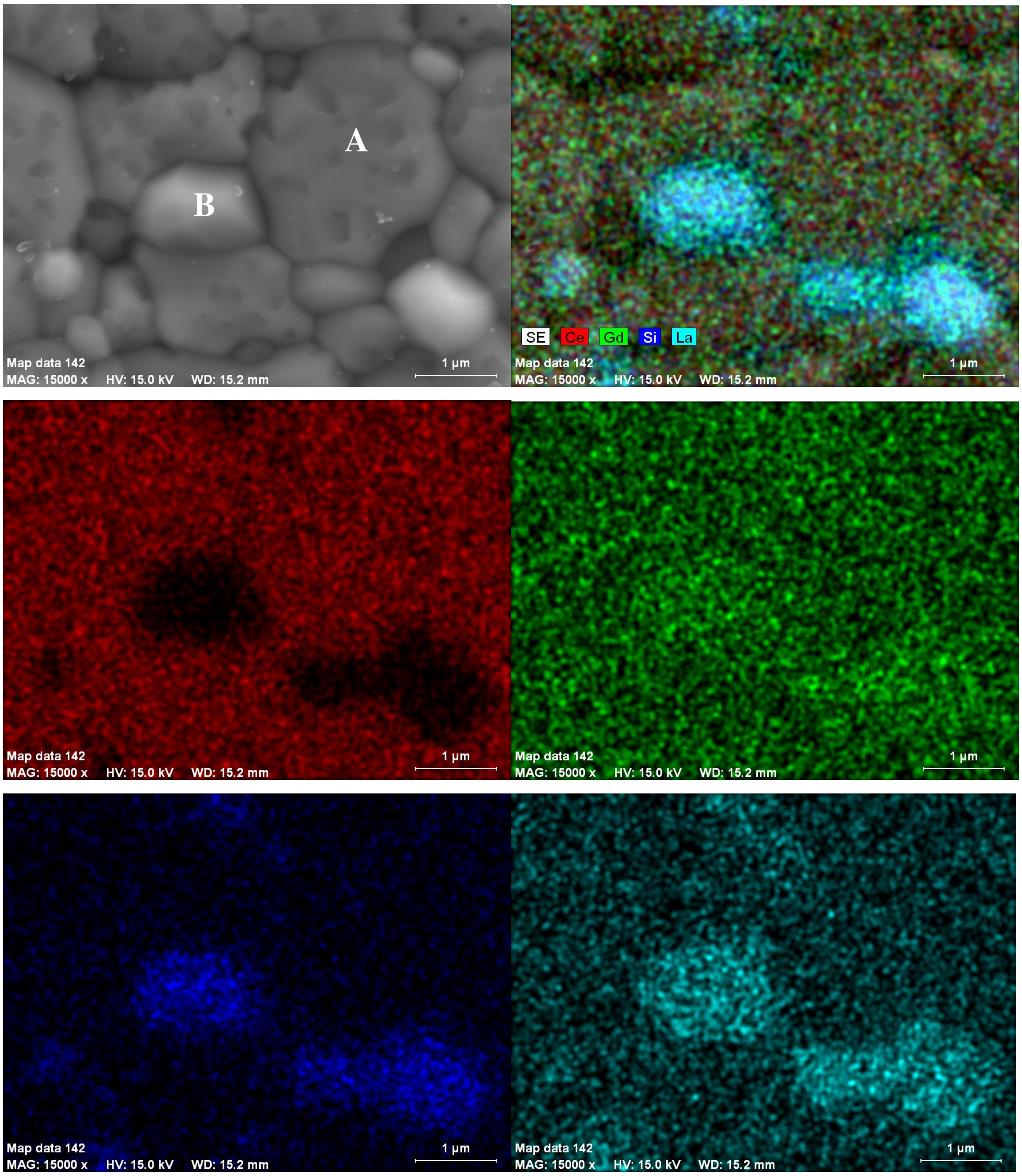

Figure 3.9. SEM micrograph and EDS maps of the CGOLSL-5%-ox sample: point A – CGO grain, point B - $La_{9.33}(SiO_4)_6O_2$-based solid solution

The microstructures of CGOLSE and CGOLSH samples (with intermediate and high amount of apatite) are identical to those of CGOLSL, deserving no special comments. The SEM images and EDS results for these compositions can thus be found in Appendix II.

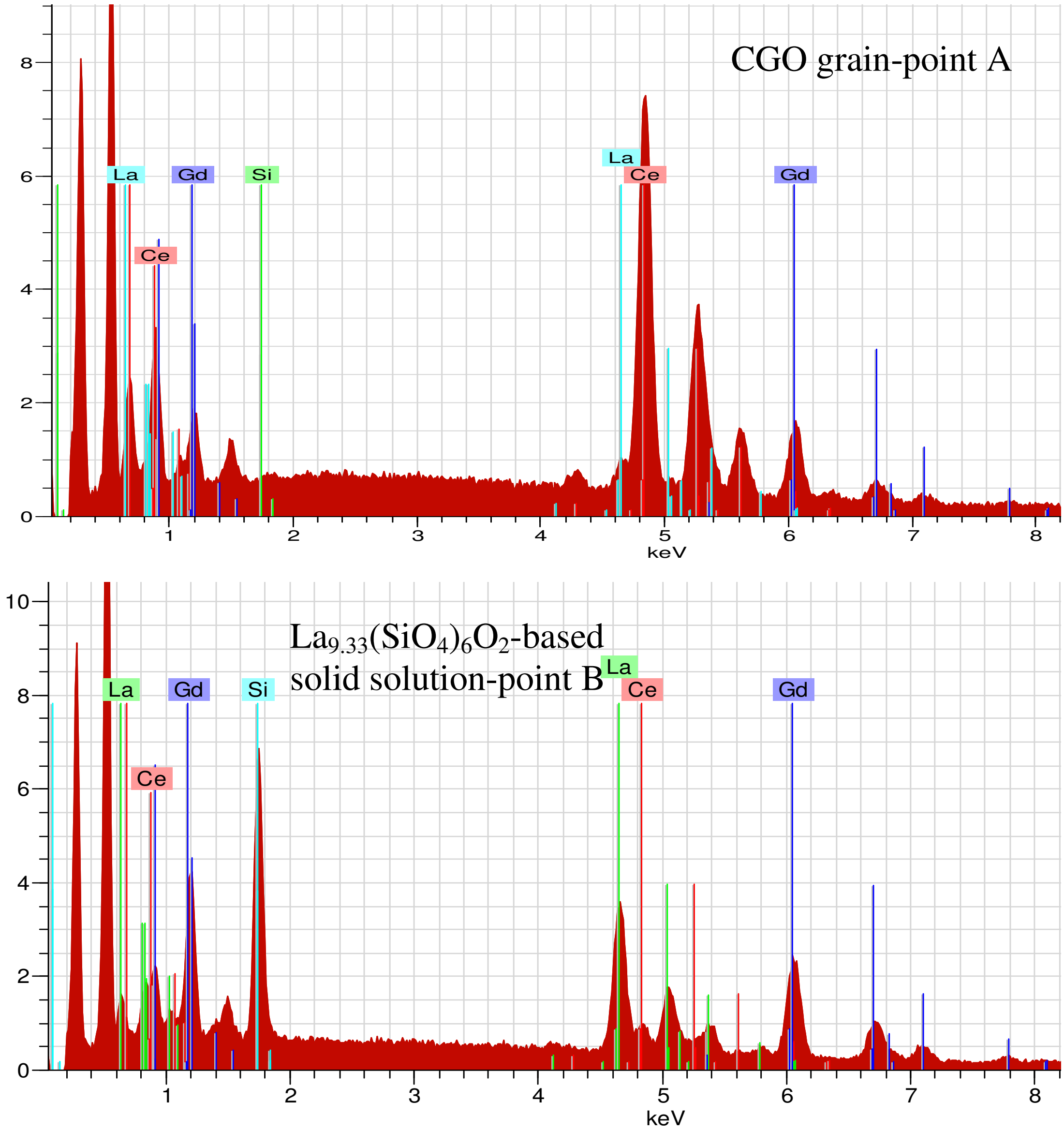

Figure 3.10 EDS spectra of CGOLSL-5%-ox: point A – CGO grain, point B - $La_{9.33}(SiO_4)_6O_2$-based solid solution (see Fig. 3.9)

Summarizing, the combined XRD and microstructural characterization of all these samples indicated two different groups of ceria-based materials. In the first group (pure CGO and CGO with low silica content) the material seemed homogeneous, with regular grain size and no visible presence of any secondary phase. In the second group of materials (CGO with large amounts of silica and all samples with apatite), the microstructure was typical of a composite, with the secondary phases spread throughout the CGO-based matrix, apparently as isolated grains located in the grain boundaries of the dominant phase. Overall, the interaction between constituents exceeded the envisaged silica scavenging effect due to the addition of lanthanum oxide. However, the tendency of silica to combine with formation of new phases was confirmed, with one lanthanum silicate-based apatite being one of the products of reaction present in these samples, as envisaged. These comments are needed to discuss the electrical performance of these materials in the next section.

3.3 Influence of La_2O_3 on the electrical properties of silica-containing CGO ceramics

In order to evaluate the influence of lanthanum oxide on the transport properties of silica-containing CGO ceramics, the ionic conductivities of pure CGO, silica-containing CGO and apatite-containing CGO were analyzed by impedance spectroscopy in air. Impedance spectroscopy can be used to separate the grain boundary and bulk contributions to the total conductivity of single phase specimens. In the case of composites the situation tends to be more complex. However, as in the present case CGO is clearly the dominant phase, data analysis adopted the simplest approach, as if in the presence of single phase materials with minor amounts of secondary phases.

Complementary information can also be obtained from these spectra, namely from the so-called arc depression and arc relaxation frequency. Highly depressed arcs usually correspond to materials with heterogeneous characteristics. Relaxation frequencies act as fingerprints of various phenomena. When appropriate, comments on such features will be introduced in the following discussion.

The impedance spectra were fitted assuming a series-parallel association of circuit elements: *R-(RQ).* The first *R* term corresponds to the bulk contribution; the second resistance and *Q,* a pseudo-capacitance/constant phase element, are related to the grain boundary contribution. The latter element was introduced taking into account that arcs were slightly depressed. The rationale for this choice will become obvious after the introduction of the impedance spectra in the following section. This was also already introduced in chapter 2.

The fitting parameters were used to estimate the grain boundary, bulk and total conductivity of samples by simple conversion of the relevant resistance value to electrical conductivity, taking into consideration the sample geometry (l - thickness of sample and S - electrode surface area):

$$\sigma = l/(S^*R) \qquad (3.1)$$

In the simplest presentation and analysis of raw impedance data, the values of impedance were normalized to account for small differences in samples electroded area and thickness.

The existence of impurities along the grain boundaries is usually noticed in impedance spectra by the presence of well-defined grain boundary arcs with magnitude sometimes exceeding the magnitude of bulk arcs. In such circumstances the effect of La_2O_3 loading as a scavenger agent should be visible for affecting the grain boundary behavior of these materials.

Considering the significant amount of materials being studied, the following discussion is organized in three major parts. The first part is focused on the analysis of the samples with higher levels of additives (CGOSi-5%, CGOLSL-5%, CGOLSE-5% and CGOLSH-5%). The silica content of these samples is not typical of commercial powders. As previously explained, these samples were studied to enhance the capability of several analytical tools to provide unambiguous information of the consequences of materials interaction.

The second set of samples studied in this section corresponds to those with silica levels close to low grade powders. From a practical point of view this is by far the most interesting set of results. In this case the analysis of the performance is divided in two parts. The first part is focused on the role of lanthanum oxide as a silica scavenger agent; the second part is dedicated to the analysis of the impact of various lanthanum oxide/silica ratios on performance.

3.3.1 Electrical properties of ceramics with high content of additive phase

The impedance spectra of CGO, silica- and apatite-containing samples measured at 500°C in air are presented in Figure 3.11. The low frequency branch of these spectra is attributed to electrode effects, while the discernible arcs correspond to the grain boundary behaviour of the materials. In fact, considering the actual working temperature and frequency range available, the high frequency bulk arc is not visible in this case. However, bulk transport properties can still be assessed from the grain boundary arc high frequency intercept with the Z' axis.

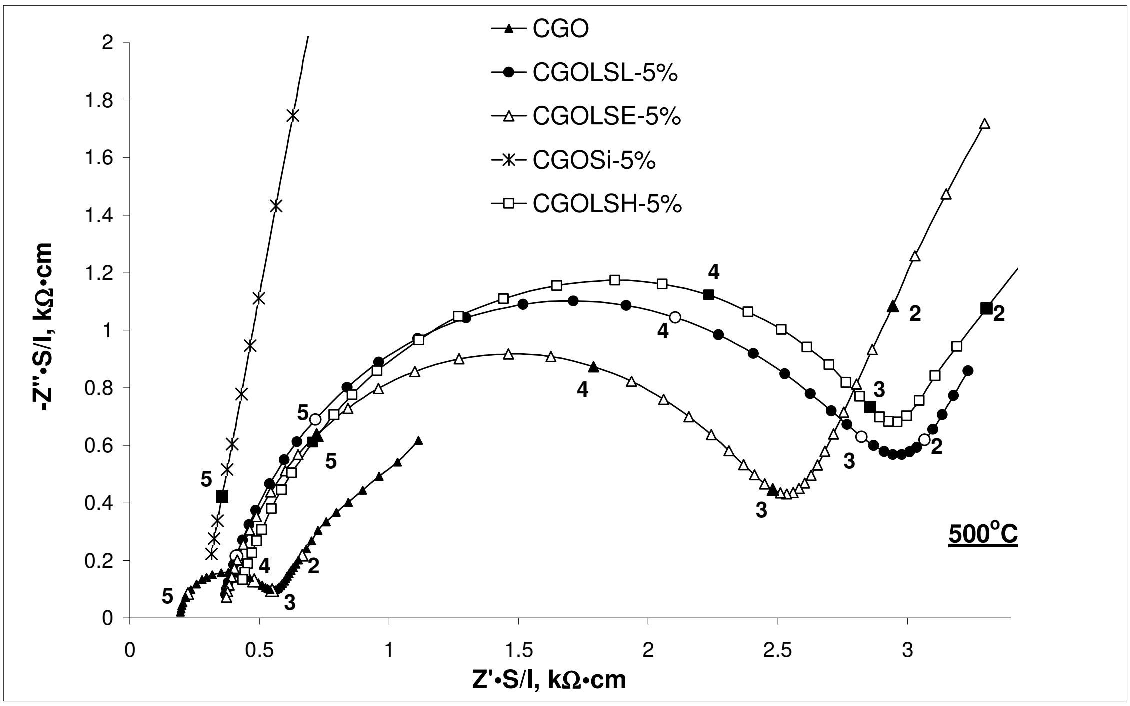

Figure 3.11 Nyquist plots obtained at 500°C in air for CGO and CGO samples containing 5% of the apatite phase

The grain boundary impedance of CGOSi-5% is very large. For this reason this set of results was plotted in a different scale, Figure 3.12. The numbers nearby highlighted points correspond to the logarithm of the measuring frequency.

These impedance spectra emphasize that high amounts of silica (5 mol%) in the CGO ceramics cause an extremely detrimental effect on the electrical properties of these materials. The total conductivity of silica-containing CGO decreased by a factor of about 120 when compared to pure CGO. This well pronounced effect was already evidenced in a wide range of previous studies [2,9,13-18, 21-27].

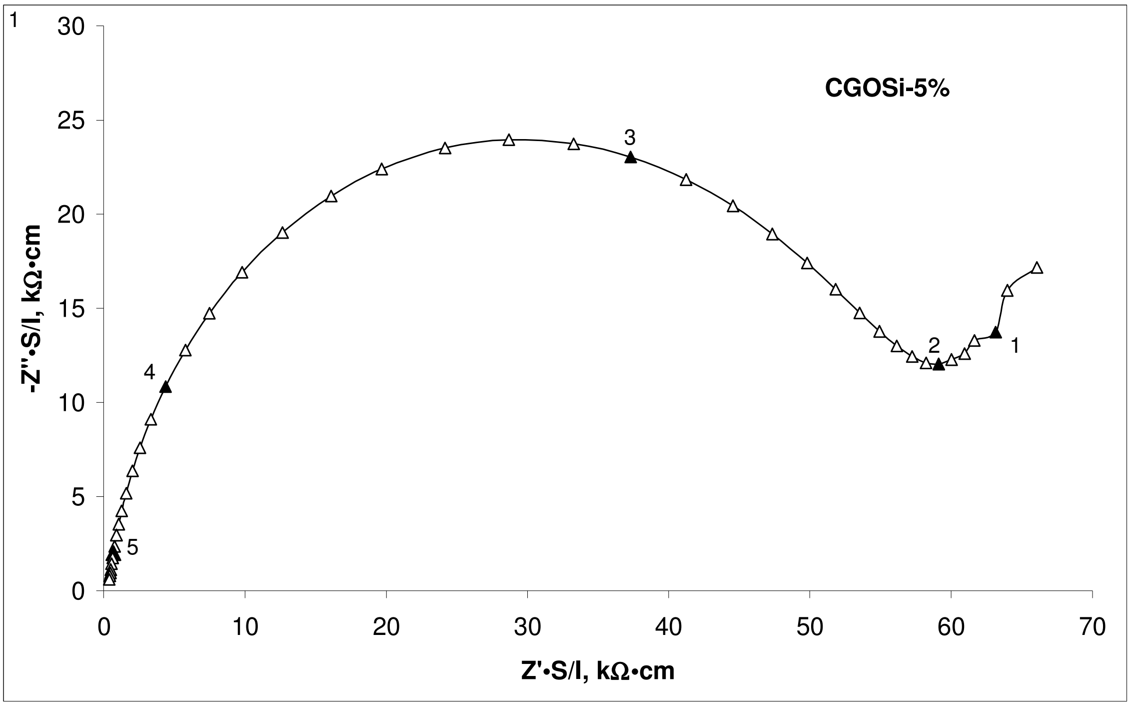

Figure 3.12 Nyquist plots obtained at 500°C in air for CGOSi-5% sample.

The main reason for this loss in ionic conductivity is related to the formation of resistive grain boundary shells in CGOSi-5%. The enlarged grain boundary impedance in silica-containing CGO ceramics is usually attributed to the presence of thin siliceous layers along grain boundaries [2, 9, 13-18, 21-27]. However, formation of another non-conductive second phase, namely the $Gd_{9.33}(SiO_4)_6O_2$-based solid solution, was also detected in our study. Both effects can contribute to the poor electrical properties of silica-containing CGO ceramics.

Addition of lanthanum oxide in adequate proportions to fully combine with silica leads to formation of one conductive apatite phase as mentioned before. Formation of $La_{9.33}(SiO_4)_6O_2$-based solid solutions in the grain boundary region is expected to remove the siliceous intergranular phase and to suppress gadolinium loss from the gadolinium-doped ceria lattice, resulting in improved ionic conductivity across grain boundaries. Figures 3.11 and 3.12 show that the grain boundary impedance of apatite containing ceramics is about 20 times lower than for CGOSi-5%. Even in the presence of such exaggerated levels of additions, the tolerance of CGO performance to the presence of the apatite phase is by far better than in the case of single silica additions.

An Arrhenius plot of the grain boundary conductivity of samples (Figure 3.13) shows that the grain boundary conductivity of the CGO containing apatite samples is much lower than for pure CGO, but still about one order of magnitude higher than the grain boundary conductivity of CGOSi-5%.

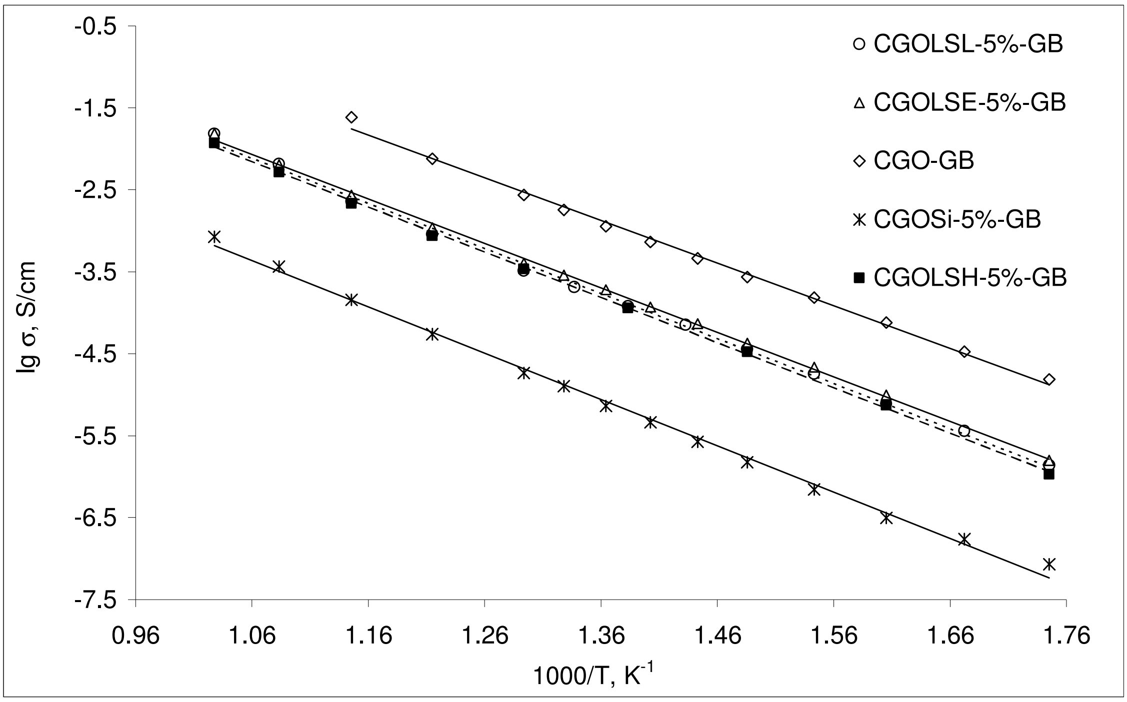

Figure 3.13 Arrhenius plot of grain boundary conductivity of CGO, CGOSi-5% and CGO samples containing 5% of the apatite phase

The bulk conductivity of CGOSi-5% is lower than for the bulk conductivity of pure CGO as a result of dissolution of gadolinium in the silica-based secondary phase and subsequent formation of the $Gd_{9.33}(SiO_4)_6O_2$ solid solution, Figure 3.14. The low bulk conductivity of CGO ceramics with the apatite phase (Figure 3.14) can be related to the high level of interdiffusion at high temperature including two complementary effects: a) lanthanum dissolution in the ceria lattice; b) migration of Gd^{3+} to the $La_{.33}(SiO_4)_6O_2$-based solid solution.

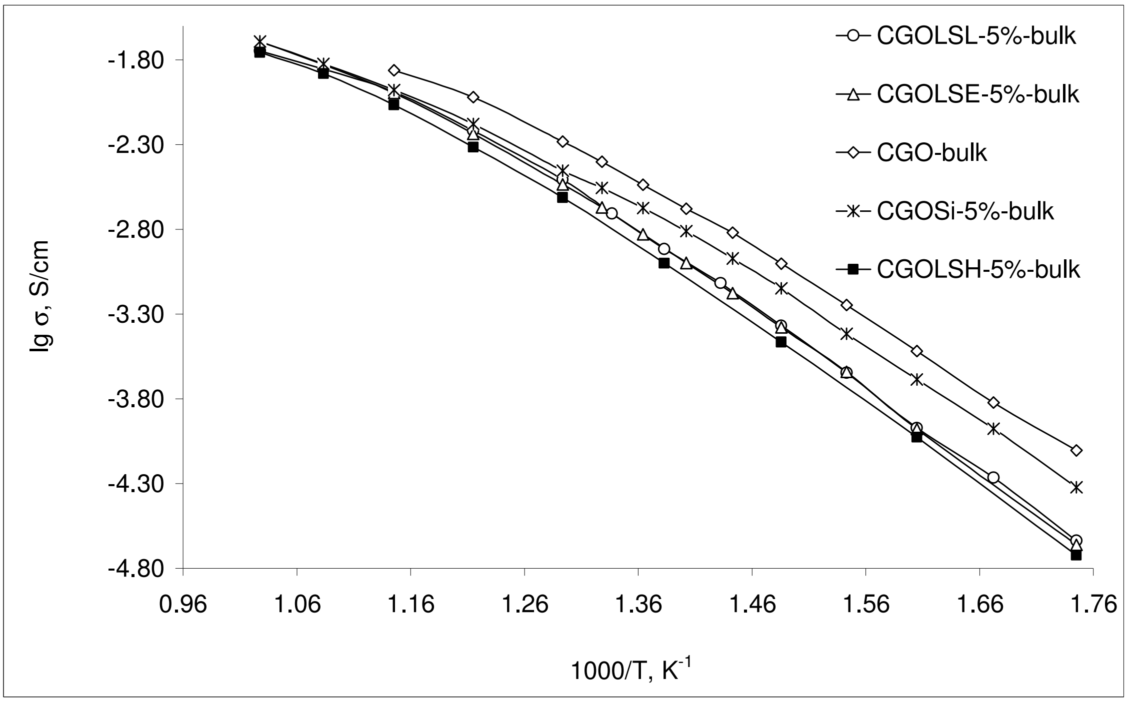

Figure 3.14 Arrhenius plot of bulk contribution to the total conductivity of CGO, CGOSi-5% and CGO samples containing 5% of the apatite phase.

The high temperature bending of the Arrhenius plots further suggests a significant role for defect association.

This reduction in bulk conductivity has only a side effect on the total conductivity of apatite-containing ceria-based ceramics since in the intermediate temperature range the total resistance is generally dominated by grain boundary effects. The total resistivity of CGO ceramics with high content of additive phases is presented in Figure 3.15.

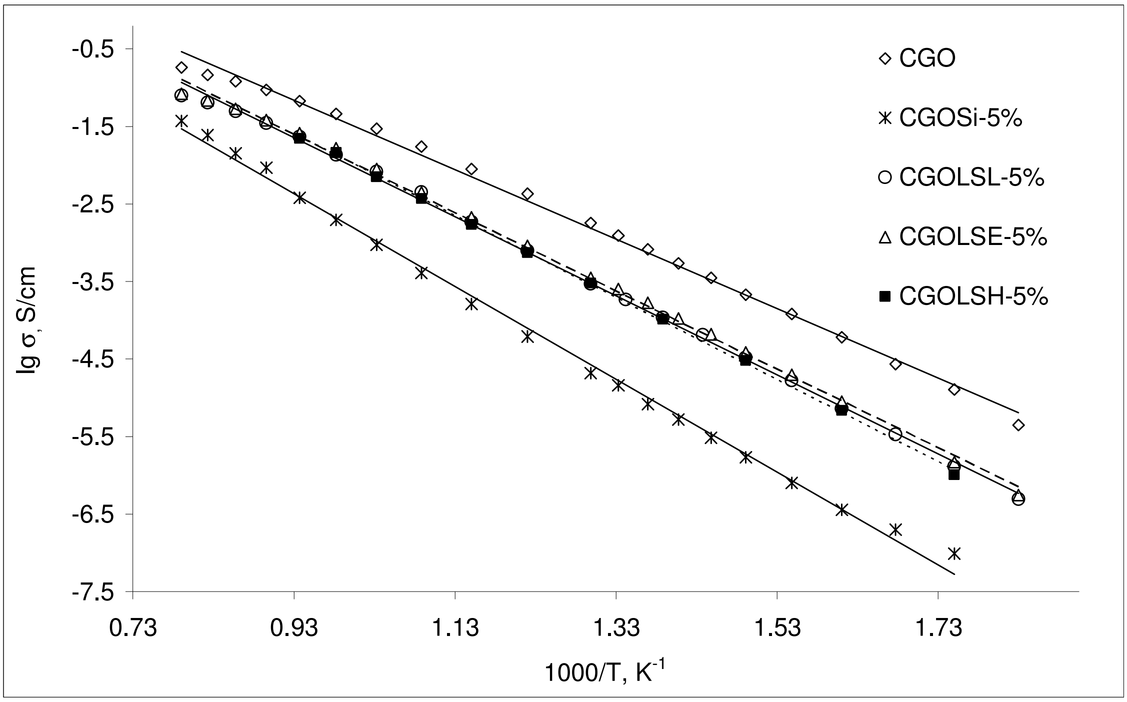

Figure 3.15 Arrhenius plot of the total conductivity of CGO, CGOSi-5% and CGO samples containing 5% of the apatite phase.

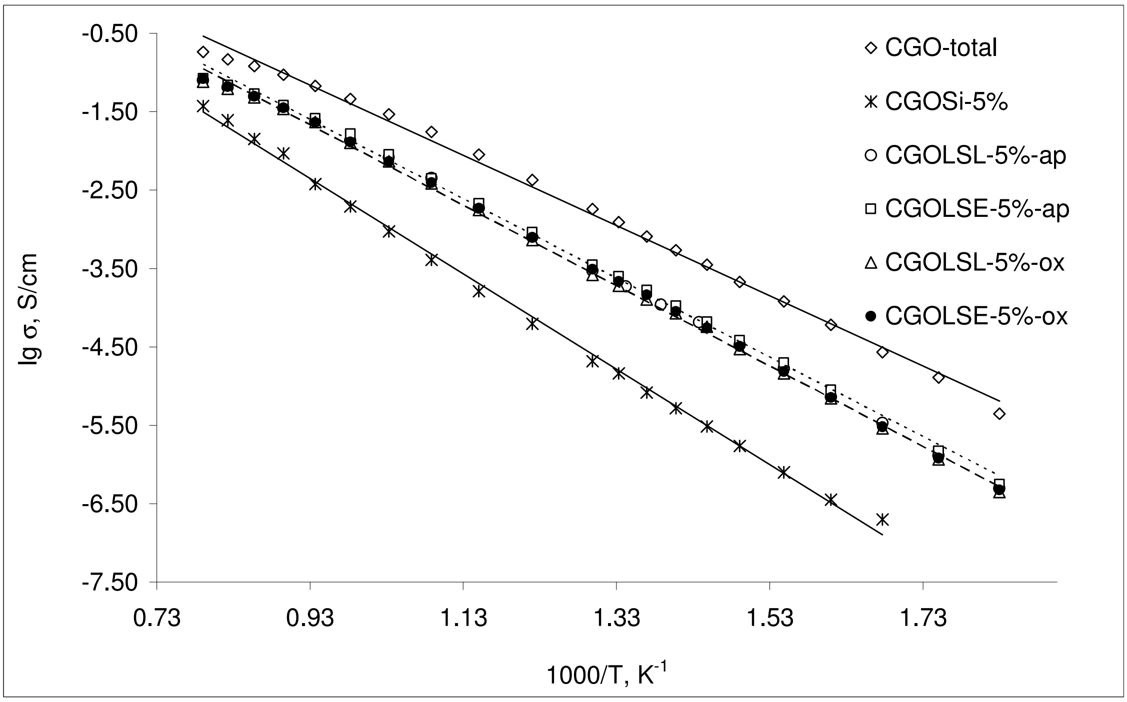

Figure 3.16 Arrhenius plot of the total conductivity of CGO, CGOSi-5% and CGO samples containing 5% of the apatite phase.

The electrical properties of CGOLSL-5%-ox and CGOLSE-5%-ox ceramics showed the same trends as for the materials formed from the pre-synthesized apatite and CGO (Figure 3.16).

Overall, these results confirmed that coexistence of lanthanum oxide and silica causes the envisaged cleaning effect of the grain boundaries of CGO ceramics. The formation of a conductive apatite phase due to reaction between silica and lanthanum oxide is responsible for the fact that less free silica remains in the grain boundary region. The formation of the apatite conductive phase in the grain boundary region significantly increases the ionic transport. However, for this high content of silica (5 mol %), hardly typical of low-grade powders, the overall result is modest. The analysis of the electrical properties of CGO ceramics with low content of silica (0.5 mol %) and lanthanum oxide will provide further information on the effectiveness of the scavenging effect of lanthanum oxide in low-grade CGO ceramics.

3.3.2 Electrical properties of ceramics with low content of additive phase

The impedance spectra of pure CGO, silica-containing samples and apatite-containing samples with 0.5 mol% of additive phase, at 500°C in air are presented in Figure 3.17. The major features of these arcs are identical to those discussed in the previous section.

Figure 3.17 shows that silica-containing CGO ceramics always have the worst transport properties. The bulk conductivity of CGOSi-0.5% decreases as a consequence of reaction between CGO and silica, as confirmed by XRD, SEM and EDS studies. The highest grain boundary impedance is also observed for the silica-containing CGO sample. The large grain boundary arc is a result of the formation of a poorly-conducting $Gd_{9.33}(SiO_4)_6O_2$-based solid solution and possible additional presence of thin siliceous layers along the grain boundaries of CGO ceramics. As the grain boundary and bulk contributions are in series, the low conductivity of grain boundaries makes the total conductivity of silica-containing samples much lower than for pure CGO.

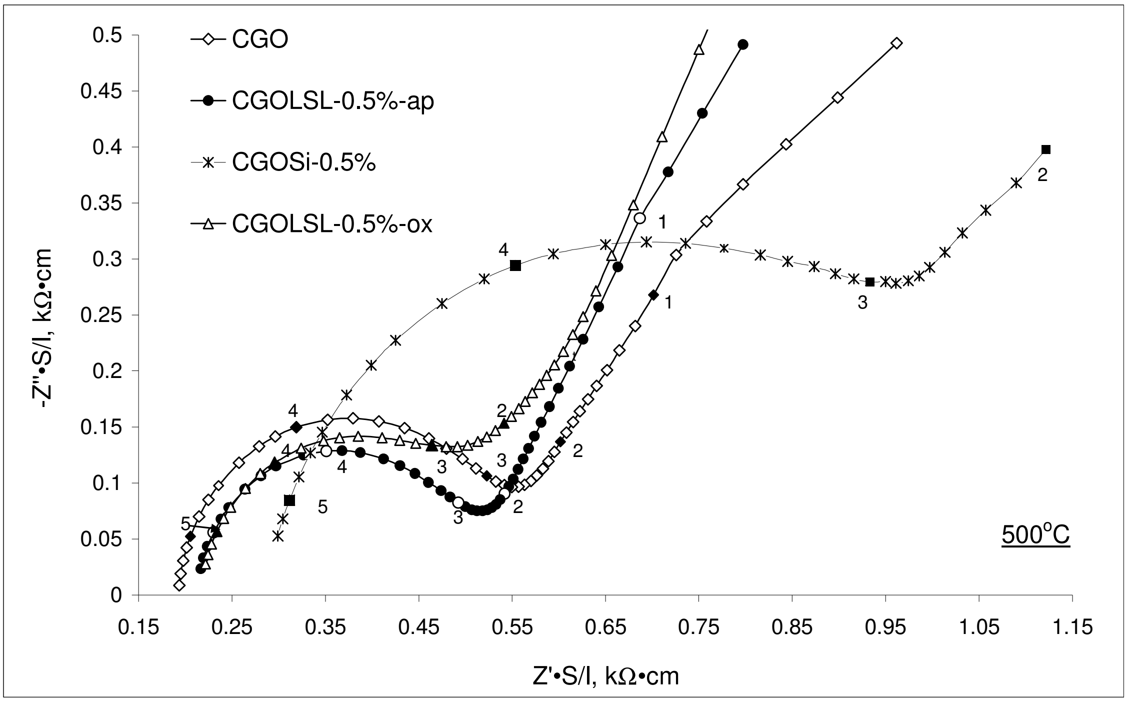

Figure 3.17 Nyquist plots obtained at 500°C in air for CGO, CGOSi-0.5% and apatite-containing samples

As expected, the grain boundary conductivity was greatly improved by the formation of a $La_{9.33}(SiO_4)_6O_2$-based solid solution in CGOLSL-0.5%. Since this apatite phase is a conductive one [28], there is no negative influence on the grain boundary resistance; instead, ion-blocking silica is removed from the grain boundaries.

The grain interior resistance of CGOLSL is slightly higher than for pure CGO. This can be explained by the loss of Gd^{3+} from the CGO lattice due to formation of gadolinium silicate (Table 3.5), at least from the outer region of CGO grains. On the other hand, some La^{3+} can also be dissolved in the ceria lattice during sintering, lowering the bulk conductivity of these materials. Overall the impact of these effects is modest.

As a result of compensation between grain boundary and bulk contributions, the total resistance of CGOLSL-0.5% is almost the same as for pure CGO, as shown in Figure 3.17.

An Arrhenius plot is presented in Figure 3.18 to provide a global picture of the bulk conductivity of these materials. The bulk resistivity of silica-containing materials is always higher than for pure CGO and apatite-containing samples. A few reasons for this effect were already mentioned. Zhang *et al.* ascribes also the decrease in the grain interior conductivity of the silica-containing ceramics to dissolution of SiO_2 in the CGO lattice [9]. Considering the EDS results for highly doped silica-containing CGO ceramics, where Si was found throughout the CGO grains (Figure 3.5) this possibility should be considered. However, the coverage with SiO_2 might also be the result of thermal etching. In this case we would be facing a surface effect rather than a bulk effect. Also, the size and preferential coordination of Si^{4+} are hardly coherent with the hypothesis of significant solubility in the ceria lattice.

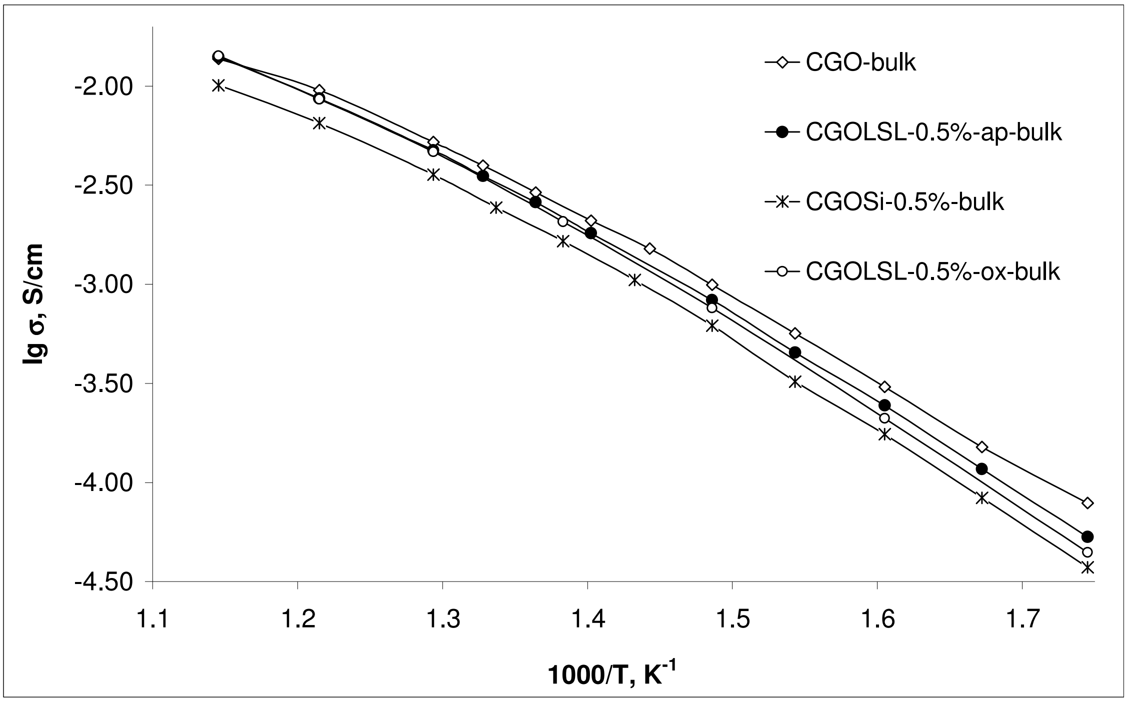

Figure 3.18 Arrhenius plot of bulk conductivity of CGO, CGOSi-0.5% and CGOLSL-0.5% samples

According to recently reported data on enhancement in bulk conductivity in co-doped ceria, dissolution of some lanthanum in CGO should yield even higher grain interior conductivity. However, in our study the bulk conductivity enhancement of lanthanum containing CGO samples was not detected, probably due to a high total dopant concentration. This comment is also coherent with the high temperature bending of the Arrhenius plots suggesting a significant role for defect association, common in highly doped materials.

As evidenced in Figure 3.19, even a small amount of silica in CGO ceramics (0.5 mol%) causes a noticeable detrimental effect on the grain boundary conductivity of these ceria-based materials.

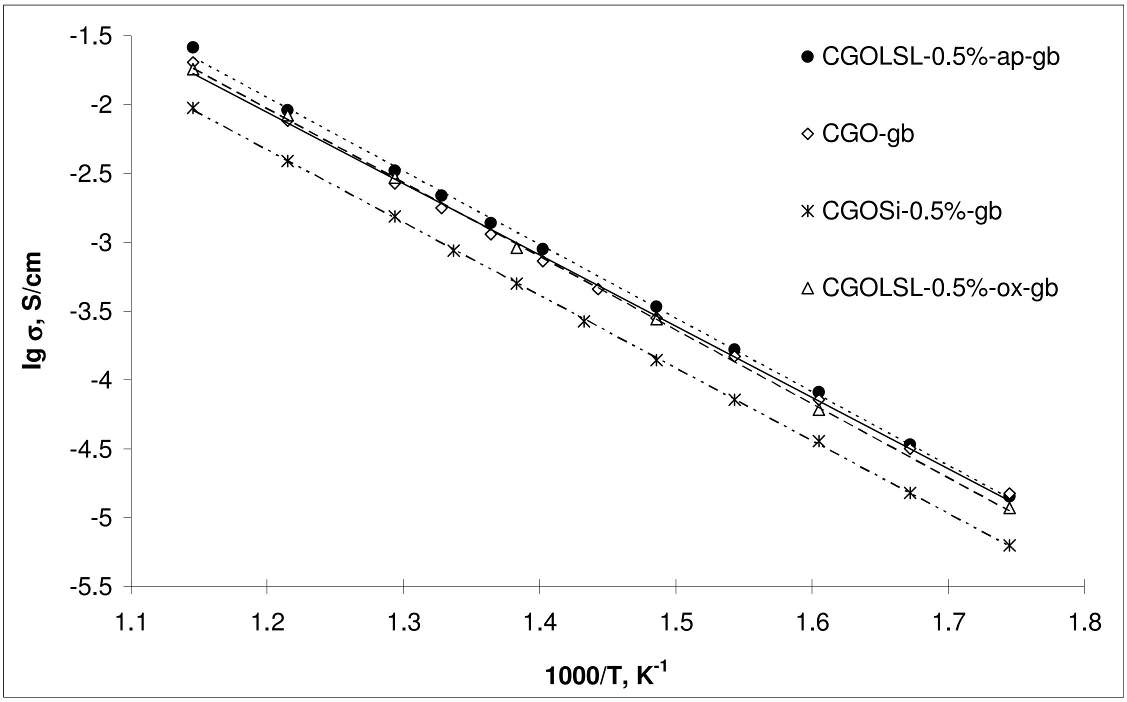

Figure 3.19 Arrhenius plot of grain boundary contribution to the total conductivity of CGO, CGOSi-0.5% and CGOLSL-0.5% samples.

Since gadolinium silicate is a poorly-conducting phase, the presence of $Gd_{9.33}(SiO_4)_6O_2$ layers or grains along the grain boundaries of CGO ceramics should increase the grain boundary resistivity of CGOSi-0.5% material. In addition, the presence of siliceous layers along the grain boundaries of CGO grains is certainly responsible for enhanced grain boundary impedance in silica containing ceria-based ceramics. Both factors explain the poor total conductivity of silica-containing samples (Figure 3.19).

Different grain boundary effects were observed in the case of apatite-containing CGO ceramics. Formation of a $La_{9.33}(SiO_4)_6O_2$-based solid solution was found to improve the grain boundary conductivity of these ceramics as can be seen from Figure 3.19. The reason for improved grain boundary properties is believed to be the scavenging of silica by lanthanum oxide.

From a practical perspective, the result worth mentioning is that the performance of “impure” CGO was upgraded to the performance of pure CGO. In this range of compositions the envisaged scavenging effect was reached without negative side effects. This can be seen from the Arrhenius plot shown in Figure 3.20 where the total conductivity of silica-containing CGO is significantly low, while the total conductivities of pure CGO and apatite-containing samples almost coincide.

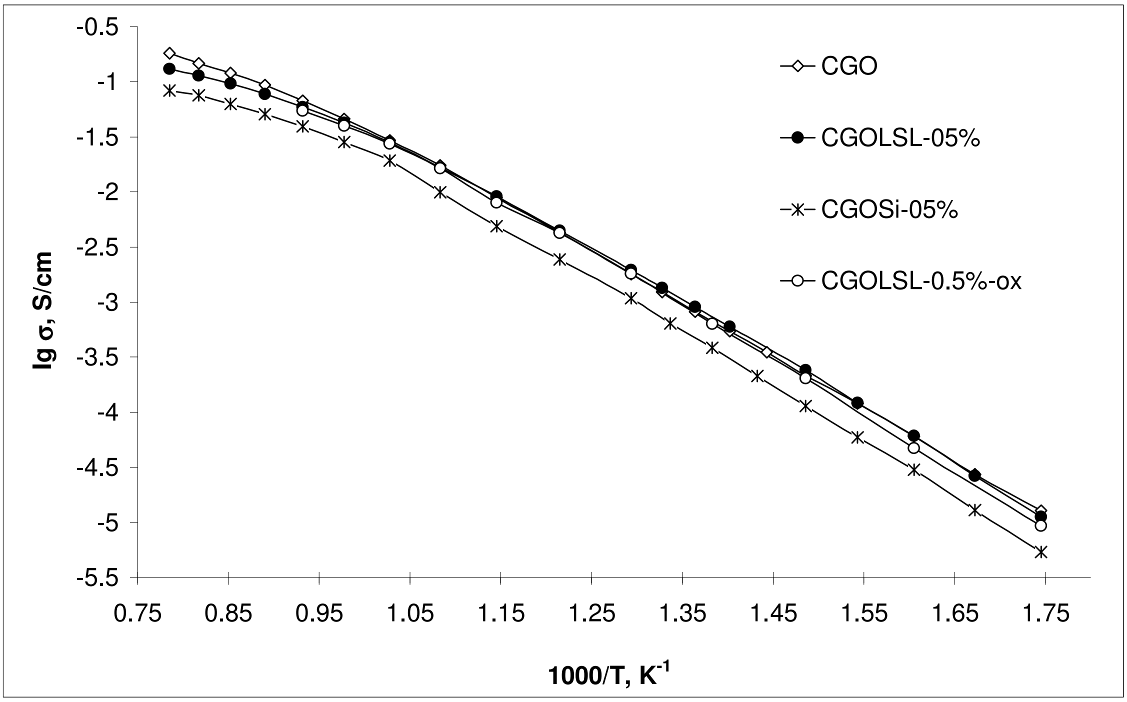

Figure 3.20. Arrhenius plot of total conductivity in air of CGO, CGOSi-0.5% and CGOLSL-0.5% samples.

Significant deviation from the Arrhenius dependence at high temperature can be explained by different dominant mechanisms at high and low temperature. Higher activation energies for ionic conduction in the low temperature range can be attributed to the already mentioned defect association process and to a more pronounced role of resistive grain boundaries [29].

3.3.3 Influence of the La_2O_3/SiO_2 ratio on the electrical properties

Different nominal compositions of lanthanum apatite were used to investigate the dependence of the grain boundary conductivity on the lanthanum oxide/silica ratio. The lowest content of lanthanum oxide corresponded to the $La_{9,33}Si_6O_{26}$ (CGOLSL) composition, the intermediate content to $La_{9,83}Si_6O_{26.75}$ (CGOLSE) and the highest one to $La_{10}Si_6O_{27}$ (CGOLSH).

The likelihood of partial migration of lanthanum to the CGO-based phase might be responsible for a lack o lanthanum oxide to fully combine with silica. On the contrary, the likelihood of partial migration of gadolinium from the CGO-based phase to the apatite phase might determine a surplus of lanthanum oxide with respect to silica. The tolerance of these apatites to various La/Si ratios enabled the present set of experiments.

The impedance spectra of the CGO ceramics with different nominal compositions of the apatite phase are presented in Figure 3.21. As expected, the La/Si ratio is indeed relevant, with major impact on the grain boundary impedance. The best results were obtained for the apatites with lower La/Si ratio and the worst result obtained for the higher La/Si ratio. Interestingly, the latter apatites with nominal excess of oxygen should exhibit better ionic transport. This suggests that the balance between the migration of La to CGO and Gd lixiviation out of CGO is likely to determine an overall excess of these trivalent cations with respect to silicium (to fully combine as a single apatite phase). In this manner the unreacted excess of La and/or Gd might form insulating oxide layers along the grain boundaries. The opposite balance between relative amounts of counter diffusing ions might also determine the formation of an oxygen deficient apatite with poor transport properties. Thus, this simple exercise is in fact inconclusive. Further experimental evidence is needed to support any of these speculations.

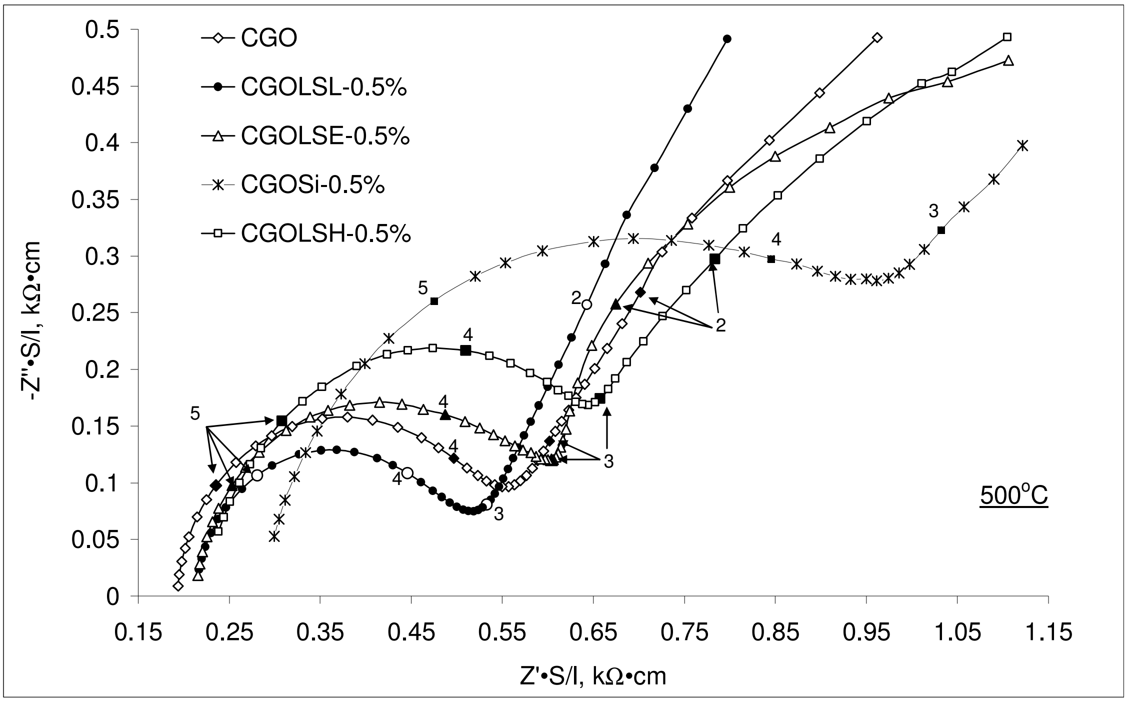

Figure 3.21 Nyquist plots obtained at 500°C in air for CGO, and CGO with different nominal compositions of the apatite phase

Unlike for grain boundaries, at 500°C the bulk behaviour of the apatite containing ceramics is not significantly influenced by the amount of La_2O_3 in the specimens. However, as the temperature decreases, the bulk conductivity of La_2O_3-rich samples decreases in a more pronounced manner, as shown in the Arrenhius plots in Figure 3.22. This loss in bulk conductivity can be caused by enhanced defect interaction in lanthanum rich CGO samples, which leads to the low mobility of oxygen vacancies and high association enthalpy of complex defects. Again caution is needed to avoid over speculation on an overall modest difference in performance.

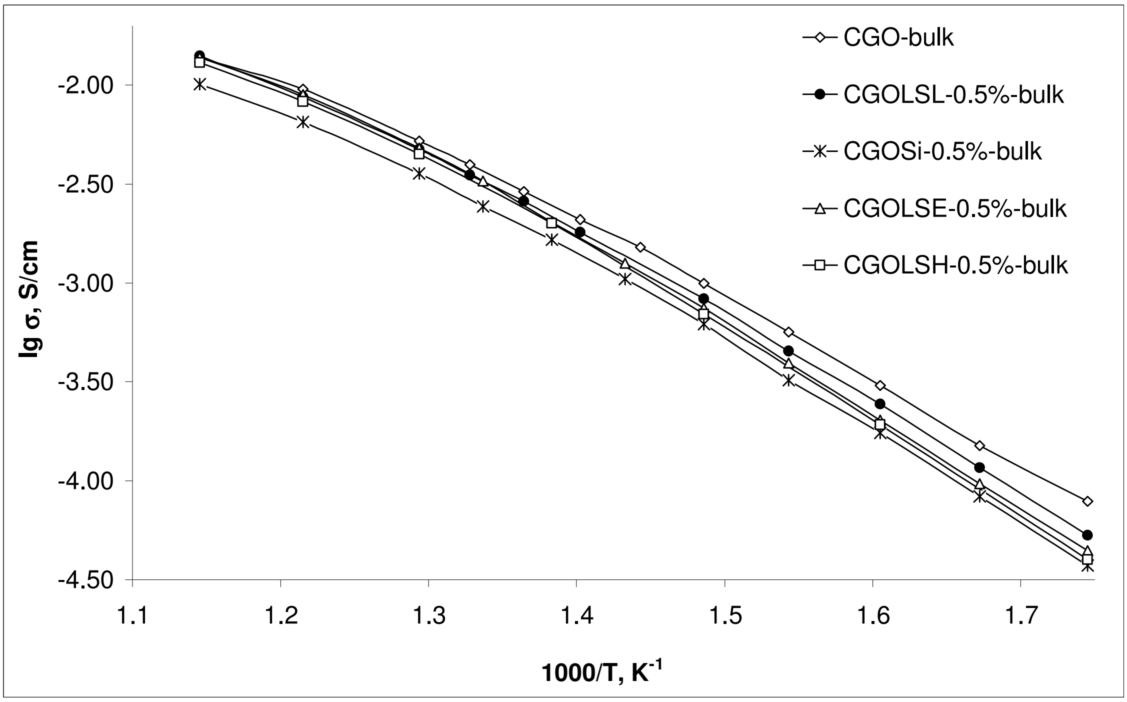

Figure 3.22 Arrhenius plot of bulk conductivity of CGO, CGOSi-0.5% and apatite-containing CGO ceramics.

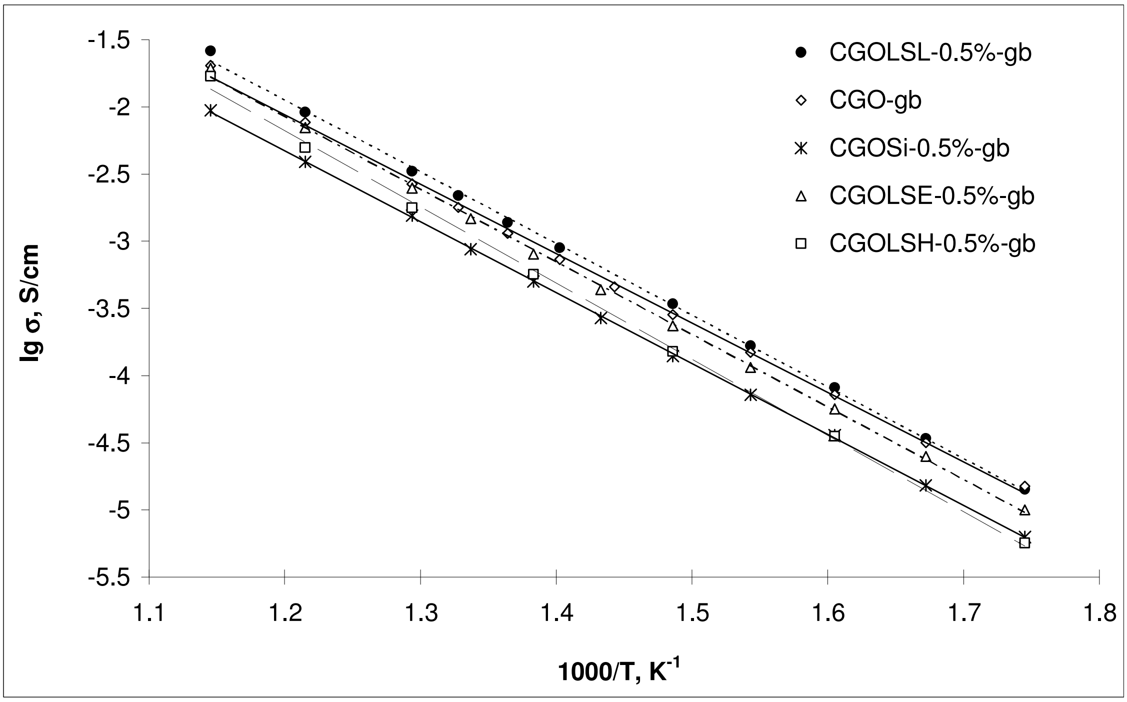

Figure 3.23 Arrhenius plot of grain boundary conductivity of CGO, CGOSi-0.5% and apatite-containing CGO ceramics.

An Arrhenius plot is presented in Figure 3.23 to provide a global picture of the grain boundary conductivity of these materials. Samples with high content of La_2O_3 perform worst than those with low lanthanum content. This tendency already discussed in the introduction of the corresponding impedance spectra (Figure 3.21), seems to prevail throughout the entire temperature range. Simple compositional effects related to the likely composition of the apatite phase and intrinsic transport properties were previously discussed. Now, the role of specific microstructural feature will be shortly addressed.

Previous results showed that all these samples (CGOLSL, CGOLSE and CGOLSH) have identical phases and interrelated microstructures but different grain size. This is due to suppressed grain growth of CGO ceramics in the presence of large amounts of La_2O_3. According to a simplified approach based on the so-called brick layer model, samples with smaller grain size should have higher grain boundary resistivity. This would explain why the lowest grain boundary conductivity was observed in samples with smallest average grain size (CGOLSH-0.5% - 3.4 μm, CGOLSE-0.5% - 4.0 μm) and the highest grain boundary conductivity was observed in CGOLSL-0.5%, with a grain size of 4.2 μm. To try to test this hypothesis another CGOLSH sample was prepared under different sintering conditions. The hereby named CGOLSH-2 sample was prepared as described in the experimental procedure but the heating rate during sintering was decreased from 5°C/min to 3°C/min. This change in the sintering process resulted in a slightly higher average grain size (3.7 μm for CGOLSH-2 compared to 3.4 μm for CGOLSH-0.5%). Coherently, the grain boundary conductivity of CGOLSH-2 is slightly higher than for the CGOLSH sample (Figure 3.24). This observation suggests that grain size plays a role in the grain boundary conductivity. However, the modest range of grain sizes also recommends a moderate emphasis on this aspect.

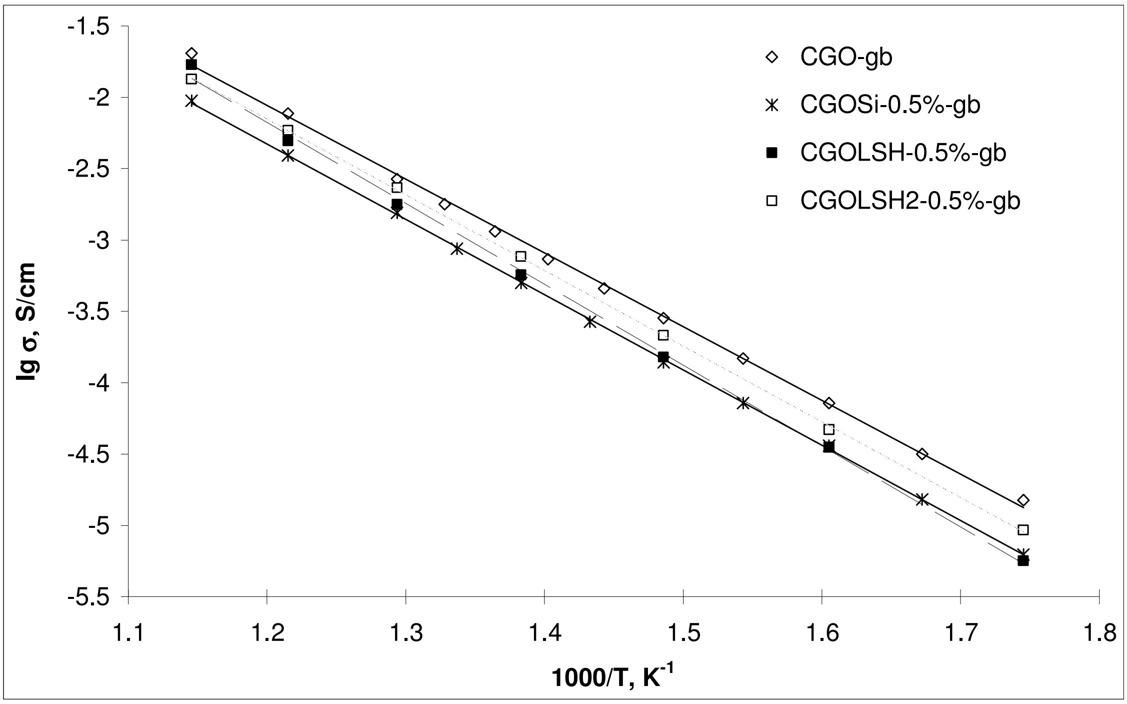

Figure 3.24 Arrhenius plot of grain boundary contribution to the total conductivity of CGO, CGOSi-0.5% and CGOLSH-0.5% ceramics.

The reduction in the grain boundary conductivity in the presence of $La_{9.83}Si_6O_{26.75}$ or $La_{10}Si_6O_{27}$ as second phase might also be related to a change in the specific grain boundary properties. Simplified attempts to estimate “true” grain boundary conductivities can be made. The most effective approach is based on the grain boundary arc peak relaxation frequency. In the case of the peak relaxation frequency size effects might cancel:

$$f_{gb}= (2\pi C_{gb}R_{gb})^{-1}= \sigma_{gb}/2\pi\varepsilon_o\varepsilon_r \qquad (3.2)$$

In eq. (3.2) $\varepsilon_o = 8.854 \cdot 10^{-12}$ F/m is the permittivity of vacuum and the relative dielectric constant ε_r is likely to be in the order of 30 [29-34].. Thus, one can calculate the true grain boundary conductivity, which is dependent on the nature of the grain boundary only:

$$\sigma_{gb} =2\pi\, f_{gb}\, \varepsilon_o\varepsilon_r \qquad (3.3)$$

The true grain boundary conductivity of all specimens was estimated following this kind of calculations. The results indicated that the grain boundary properties were all still within a narrow range of values preventing any meaningful distinction between compositions.

One final comment is needed on the overall deepness of these analyses. Grain boundaries tend to be complex even in single phase materials. The grain boundary space charge layer is obviously sensitive to composition and, for a given composition, to processing conditions. Solute and defect segregation effects are always present but depend strongly on processing conditions. This picture is even more complex in the case of composite materials when thin layers of a second phase cover the grains. A series resistance might have to be added to the remaining contributions. The complexity of this type of analysis clearly exceeded the limits and envisaged goals of this work.

3.4 Final comments

While the previous results suggest a meaningful role of several additions as silica scavengers, a more delicate distinction on the impact of minor compositional changes seems hardly sustainable. Other indirect evidence also points in the same direction.

Firstly, impedance plots as those shown in Fig. 3.21, clearly show that the range of frequencies of the grain boundary arcs corresponding to the various compositions are roughly the same. This is a strong indication that the various materials being studied show similar major microstructural characteristics.

One second series of results enhancing this aspect is obtained when comparing the various activation energies for the bulk and grain boundary conductivities of all samples. The summary of these results is shown in Table 3.5.

The only meaningful change is in the case of the bulk conductivity of pure CGO, where the activation energy is clearly lower than for the remaining compositions. This might be understood as a consequence of bulk compositional changes due to the strong phase interaction, already discussed in previous sections. The activation energies for grain boundary conductivities are all within a narrow range of values. These features were already evidenced by the apparent similarity between the slopes of all lines included in the Arrhenius plots previously presented.

Table 3.5 Relative densities, average grain size and activation energies for the bulk and grain boundary conductivities of samples studied in this work.

Abbreviation	Relative density, %	Average grain size, μm	Activation energy	
			E_a bulk, kJ/mol	E_a gb, kJ/mol
CGO	93.8	4.70	86±2	105±3
CGOSi-0.5%	93.9	3.73	93±3	107±1
CGOLSL-0.5%	93.5	4.23	91±3	108±3
CGOLSL-0.5%-ox	92.9	3.97	96±2	111±3
CGOLSE-0.5%	93.4	4.04	94±2	109±3
CGOLSE-0.5%-ox	92.9	3.78	96±3	110±4
CGOLSH-0.5%	93.5	3.39	95±3	114±5
CGOLSH-0.5%-ox	92.3	3.22	95±5	110±5

3.5 Conclusions

The role of lanthanum oxide as a silica scavenger in ceria-based electrolytes was clearly demonstrated. The grain boundary conductivity of compositions including silica and lanthanum oxide was clearly superior to the corresponding characteristics of those of CGO-based samples with single silica additions.

As a side consequence, strong interaction between constituents was also observed. The loss of Gd from CGO to the secondary phases was partly balanced by the diffusion of La to CGO grains. Interestingly, the bulk transport properties of these composite materials were quite close to the transport properties of phase pure CGO samples.

The adopted processing conditions and overall structural, microstructural and electrical results suggest that we might be in the presence of heterogeneous ceramics with significant compositional gradients, where the final stage is partly governed by slow mass transport kinetics.

3.6 References

1 J.S. Lee, K.-H. Choi, M.-W. Park,D.-J. Kwak, K.-H. Shin, C.-W. Shin, Journal of Materials Science, 41 (2006) 7983-7988

2 T.S. Zhang, J. Ma, L.B. Kong, P. Hing, Y.J. Leng, S.H. Chan, J.A. Kilner, Journal of Power Sources, 124 (2003) 26-33

3 N.J. Shaw, Powder Metallurgy International, 21 (5) 1989, 31-33

4 H. Inaba, T. Nakajima, H.Tagawa, Solid State Ionics, 106 (1998) 263-268

5 J.-G. Li, Y.Wang, T. Ikegami, T. Ishigaki, Solid State Ionics, 179 (2008) 951-954

6 S. Sameshima, K. Higashi, Y. Hirata, Journal of Ceramic Processing Research, 1 (2000) 27-33

7 J.G.Li, T. Ikegami, T. Mori, Acta Materialia, 52 (2004) 2221-2228

8 T.S. Zhang, J.Ma,Y.Z. Chen, L.H. Luo, L.B. Kong, S.H. Chan, Solid State Ionics, 177 (2006) 1227-1235

9 T.S. Zhang, J. Ma, S.H. Chan, P. Hing, J.A. Kilner, Solid State Science, 6 (2004) 565-572

10 A. Blasse, Materials Research Bulletin, 21 (1986) 683

11 E. Rocchini, A. Trovarelli, J. Llorca, G. Graham, W. Weber, M. Maciejewski, A. Baiker, Journal of Catalysis, 194 (2000) 461

12 U. Kolitsch, H.J. Seifert, F. Aldinger, Journal of Alloys and Compounds, 257 (1997) 104-114

13 T.S. Zhang, J. Ma, L.B. Kong, S.H. Chan, P. Hing, J.A. Kilner, Solid State Ionics, 168 (2004) 187-195

14 P.S. Cho, S.B. Lee, Y.H. Cho, D.Y. Kim, Journal of Power Sources, 183 (2008) 518-523

15 D.K. Kim, J.-H. Lee, P.-S. Cho, G. Auchterlonie, D.-Y. Kim, H.-M. Park, J. Drennan, Electrochemical and Solid State Letters, 10 (2007) (5) B91-

B95
16 Y.H. Cho, P.-S. Cho, G. Auchterlonie, D. K. Kim, J.-H. Lee, D.-Y. Kim, H.-M. Park, J. Drennan, Acta Materialia, 55 (2007) 4807-4815
17 S.D. Kim, P.-S. Cho, J.-H. Lee, D.-Y. Kim, H.-M. Park, Solid State Ionics, 177 (2006) 2125-2128
18 A.V. Kovalevsky, F.M.B. Marques, V.V. Kharton, F. Maxim, J.R. Frade, Ionics 12 (XXXX) 179-184
19 K N.Alsbeek, S. Larsen, J.G.Ronsbo, Cristallography, 191 (1990) 249
20 A. de Vries, G. Blasse, Materals Research Bulleten, 21 (1986) 683
21 S.P.S. Badwal, Solid State Ionics, 76 (1995) 67,
22 X.J.Chen, K.A. Khor, S.H. Chan, L.G.Yu, Materials Science and Engineering A, 335 (2002) 246-252
23 J. Drennan, G. Auchterlonie, Solid State Ionics, 134 (2000) 75-87
24 Xin Guo, Chao-Qun Tang, Run-Zhang Yuan, Journal of the European Ceramic Society, 15 (1995) 25-32
25 X.J.Chen, K.A. Khor, S.H. Chan, L.G.Yu, Materials Science and Engineering A, 374 (2004) 64-71
26 Xin Guo, Solid State Ionics, 96 (1997) 247-254
27 Aya Yuzaki, Akira Kishimoto, Solid State Ionics, 116 (1999) 47–51
28 A.L. Shaula, V.V. Kharton, F.M.B. Marques, Journal of Solid State Chemistry, 178 (2005) 2050–2061
29 D. Perez-Coll, P. Nunez, J. R. Frade, J. C. C. Abrantes, Electrochimica Acta, 48 (2003) 1551-1557
30 G.M. Christie, F.P.F. van Berkel, Solid State Ionics, 83 (1996) 17-27
31 D. Perez-Coll, P. Nunez, D. Marrero-Lopez, J. C. C. Abrantes J. R. Frade, Journal of Solid State Electrochemistry, 8 (2004) 644-649
32 D. Perez-Coll, P. Nunez, J. C. C. Abrantes, D.P. Fagg, V.V. Kharton, J. R. Frade, Solid State Ionics, 176 (2005) 2799-2805
33 D. Perez-Coll, P. Nunez, J.C. Ruiz-Morales, J.Pena-Martinez,J.R. Frade, Electrochimica Acta, 52 (2007) 2001-2008
34 D. Perez-Coll, D. Marrero-Lopez, P. Nunez, S. Pinol, J. R. Frade, Electrochimica Acta, 51 (2006) 6463-6469

35 J.C.C. Abrantes, J.A. Labrincha, J.R. Frade, Journal of the European Ceramic Society, 20 (2000) 1603-1609

Chapter 4

4 Conclusions

The effect of lanthanum oxide loading in silica-containing ceria-based ceramics was investigated. Addition of La_2O_3 was found to drive the microstructure of ceria based ceramics from homogeneous (identical grain size, typical for pure CGO and also for CGOSi-0.5%) to a composite microstructure for the apatite-containing ceramics, with a second phase (apatite-type solid solutions) dispersed in the CGO matrix. Additionally, the introduction of lanthanum oxide in CGO ceramics caused lower densification and suppressed grain growth as a likely result of segregation of lanthanum oxide in the grain boundary region.

Extensive interaction between precursors (in the cases of silica and silica + lanthanum oxide additions) determined significant deviation from nominal composition of major phases. CGO lost Gd to the remaining phases while La diffused to CGO. One CGO-based fluorite type phase was always present as dominant phase, but two apatite-type phases were also identified as reaction products. Combined structural and microstructural analyses provided coherent evidence for this.

The evaluation of the transport properties of CGO-based composites, performed by impedance spectroscopy, showed that two opposite effects might partly cancel each other when La_2O_3 additive is loaded to silica-containing CGO ceramics:

i) since the grain size of the apatite-containing CGO ceramics is reduced (as a result of suppressed grain growth in the presence of La_2O_3 additive) a decrease in the grain boundary conductivity is expected as the number of grain boundaries per unit volume is increased, following a classical trend in similar types of ceramics.

ii) since La_2O_3 reacts with the silica impurity present in the grain boundary region, a significant increase in the actual grain boundary conductivity is expected.

As a consequence of both trends, the grain boundary conductivity of silica-containing CGO ceramics is still improved by lanthanum oxide addition in the nominal proportion to form the $La_{9.33}Si_6O_{26}$ apatite phase. The scavenging effect, although positive, becomes less pronounced when $La_{9.83}Si_6O_{26.75}$ or $La_{10}Si_6O_{26.75}$ are the nominal targets as secondary phase.

As a side consequence of strong interaction between batch constituents, fluorite-type materials with significant amounts of La and loss of Gd with respect to the starting CGO composition, evidenced interesting bulk transport properties. This reinforced the present interest in the search for novel compositions of electrolytes based on co-doping of ceria-based materials.

Overall, the formation of a conductive apatite phase as a result of reaction between silica impurity and lanthanum oxide was clearly shown as a useful procedure to improve the grain boundary conductivity of gadolinium doped ceria, prevailing over other negative effects.

Chapter 5

Suggestions for further work

This work demonstrated that lanthanum oxide can be used as a cleaning agent to remove silica (present in low grade CGO powders) from grain boundaries of sintered ceramics. However, a number of questions still need careful investigation.

Firstly it would be desirable to observe in greater detail the presence of the assumed secondary glassy phase, in low content silica-containing CGO ceramics, by means of high resolution transmission electron microscopy. This technique could be useful to know better the exact location of the silica phase in CGO ceramics. This could clarify which of the microstructural models can describe more accurately the electrical transport properties of impure CGO ceramics. Also, this could improve our knowledge on the homogeneous or heterogeneous nature of the fluorite phase after interaction with the remaining constituents. In fact, the analytical tools used in this work were not enough to identify meaningful composition gradients in CGO grains.

Secondly, a wider range of lanthanum oxide additions to CGO materials could improve the present knowledge on phase interaction and influence of La_2O_3 content on the grain boundary and bulk conductivity of CGO ceramics. For instance, a number of previous studies showed that co-doping of ceria with several rare-earth elements results in enhanced grain interior conductivity. A detailed investigation of the bulk conductivity of CGO samples doped with different amounts of La_2O_3 can be useful for the optimization of bulk transport properties.

Another suggestion is on the analysis of impedance spectroscopy data. The present level of analysis consisted mostly in the deconvolution of the spectra in nominal bulk and grain boundary contributions. The composite nature of many samples might justify a deeper examination of changes in the arc depression, arc overlap, shift in relaxation frequency and other parameters which might be used as fingerprints of compositional and microstructural changes.

Last but not least, the optimization of the sintering route is essential in this case. Two main aspects need consideration:

1. Considering the reported strong interaction between constituents, it is important to lower the sintering temperature. Several ways can be adopted to improve the sinterability of CGO ceramics. Considering that high-energy ball milling was already adopted in the framework of this study, an alternative approach could be the addition of sintering promoters like Co_2O_3 or Ga_2O_3. However, addition of a new component can cause the formation of undesirable new phases in the system. The tolerance of the apatite phase to various dopants might be used to screen potential co-dopants as sintering promoters.
2. In order to obtain ceramics with larger difference in grain size alternative processing routes and sintering conditions are needed. This kind of experiments could show more accurately the dependence of the grain boundary conductivity on the grain size of ceramics. To reach this goal one possibility would be the so-called two-step sintering approach, where samples are brought to a peak temperature to activate the densification process, and afterwards are kept at a lower temperature to increase densification without grain growth.

Appendix I

The refinement profiles of silica- and apatite-containing CGO samples used in study are represented in this section.

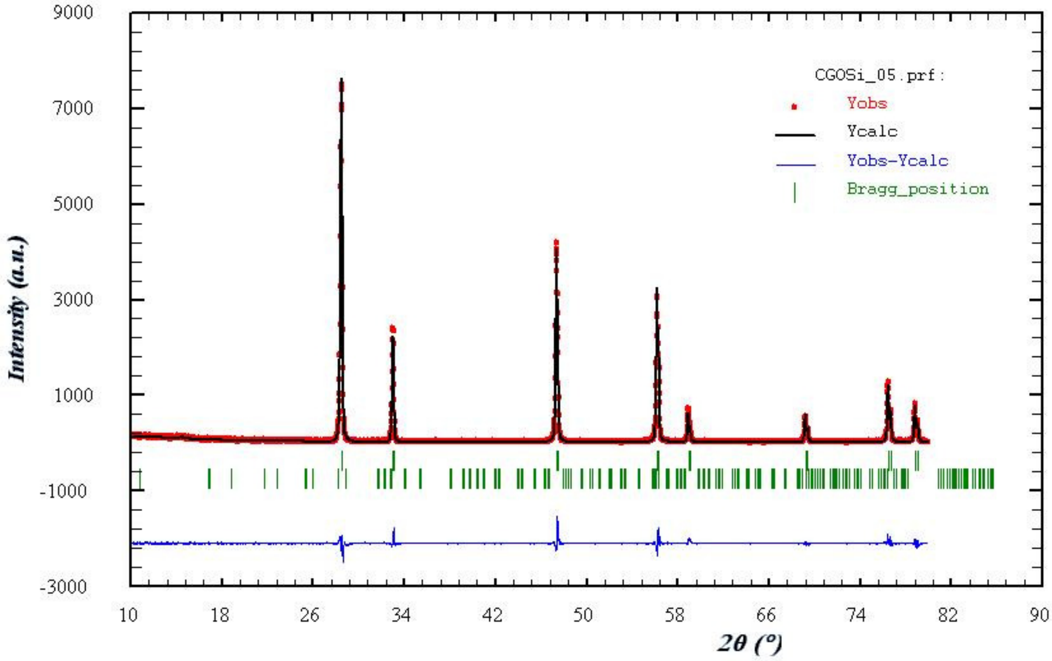
CGOSi_05

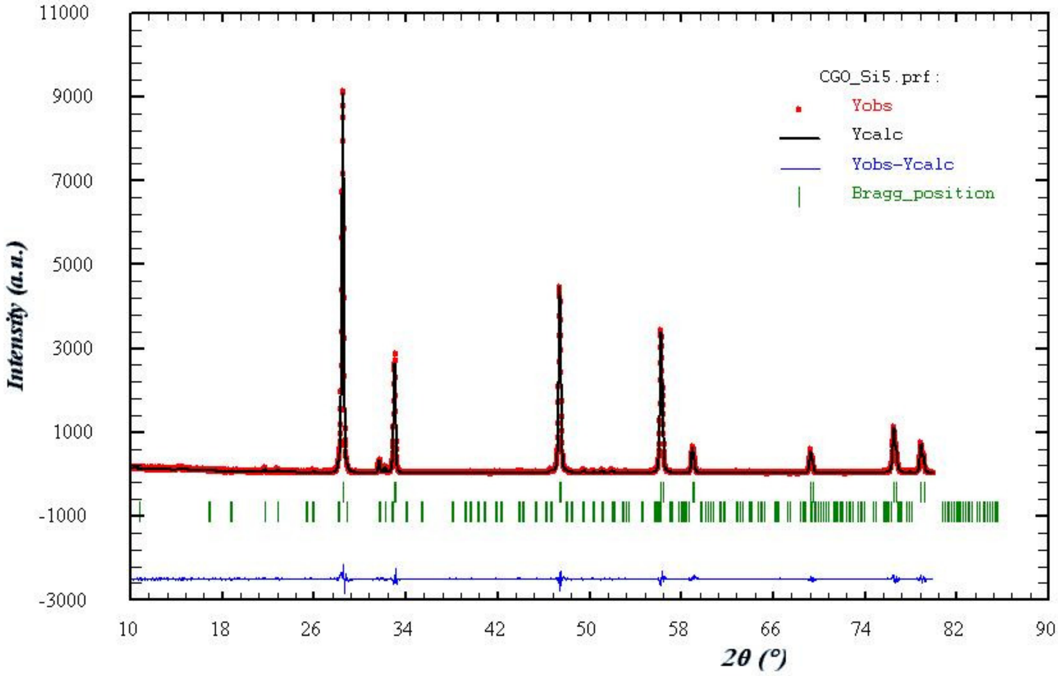
CGO-Si5%

CGOLSL05

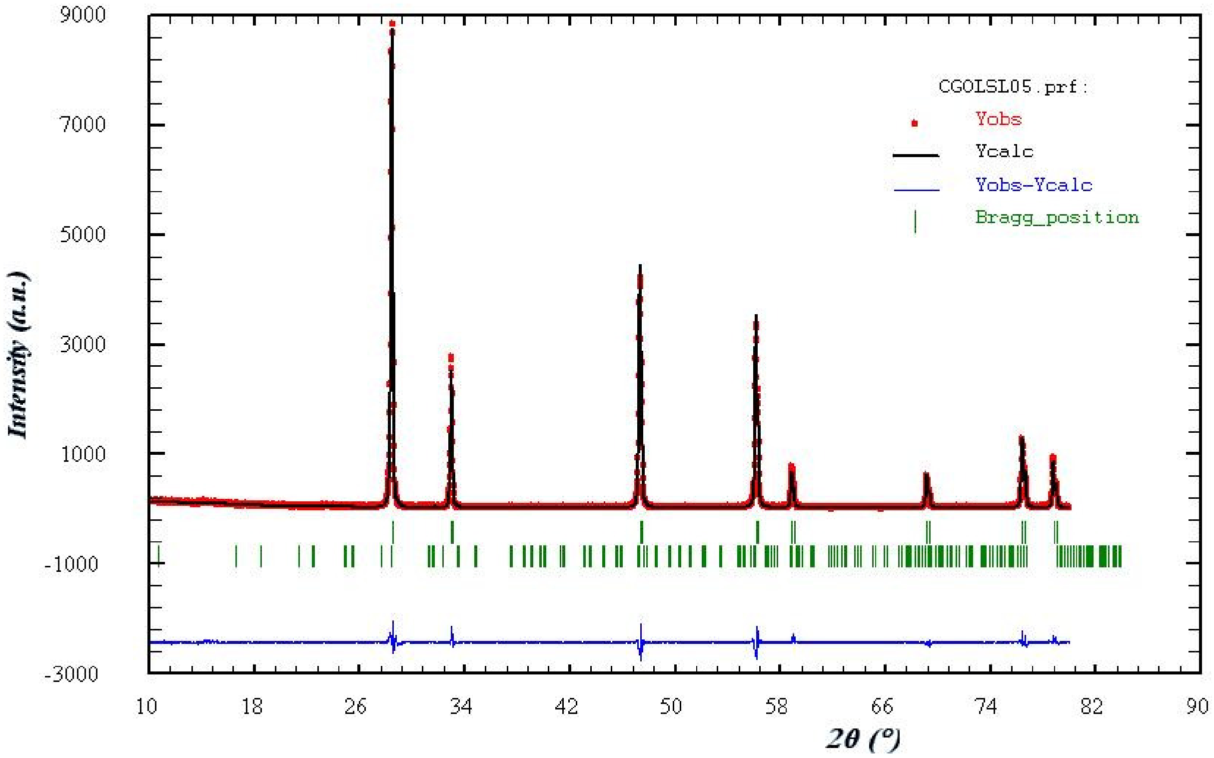

CGOLSL5

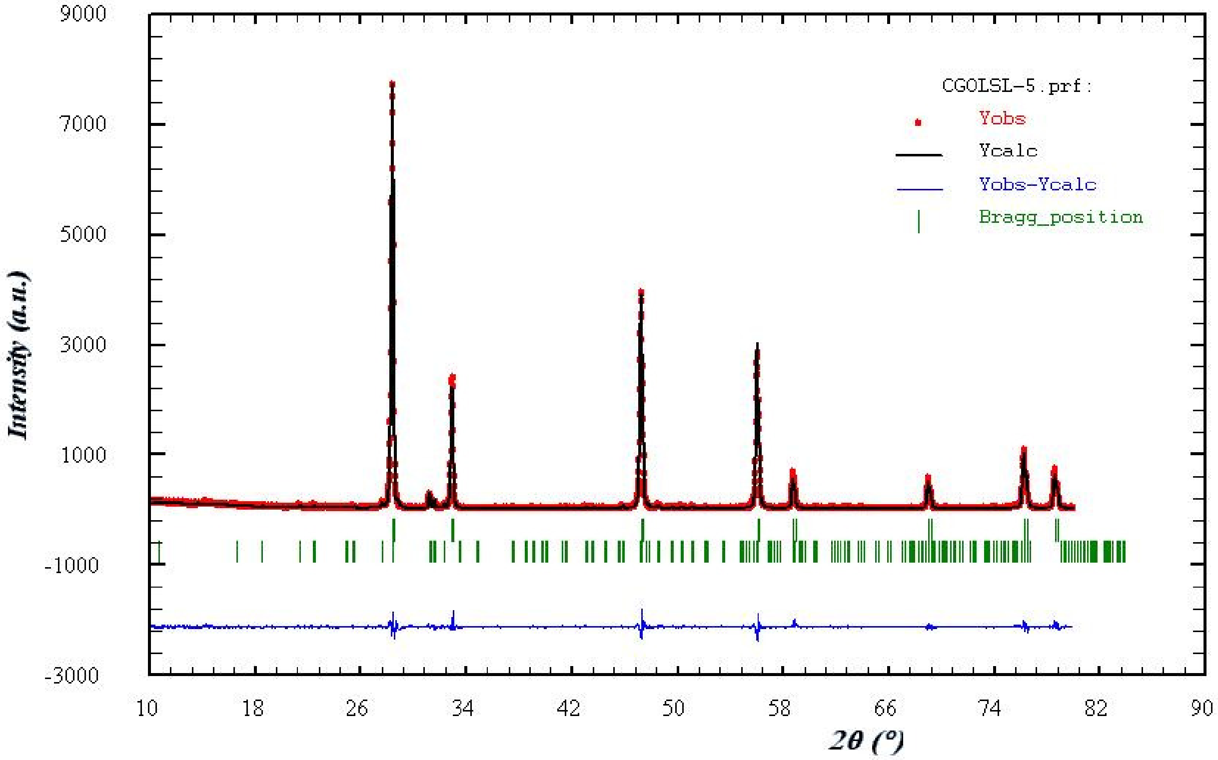

CGOLSE05

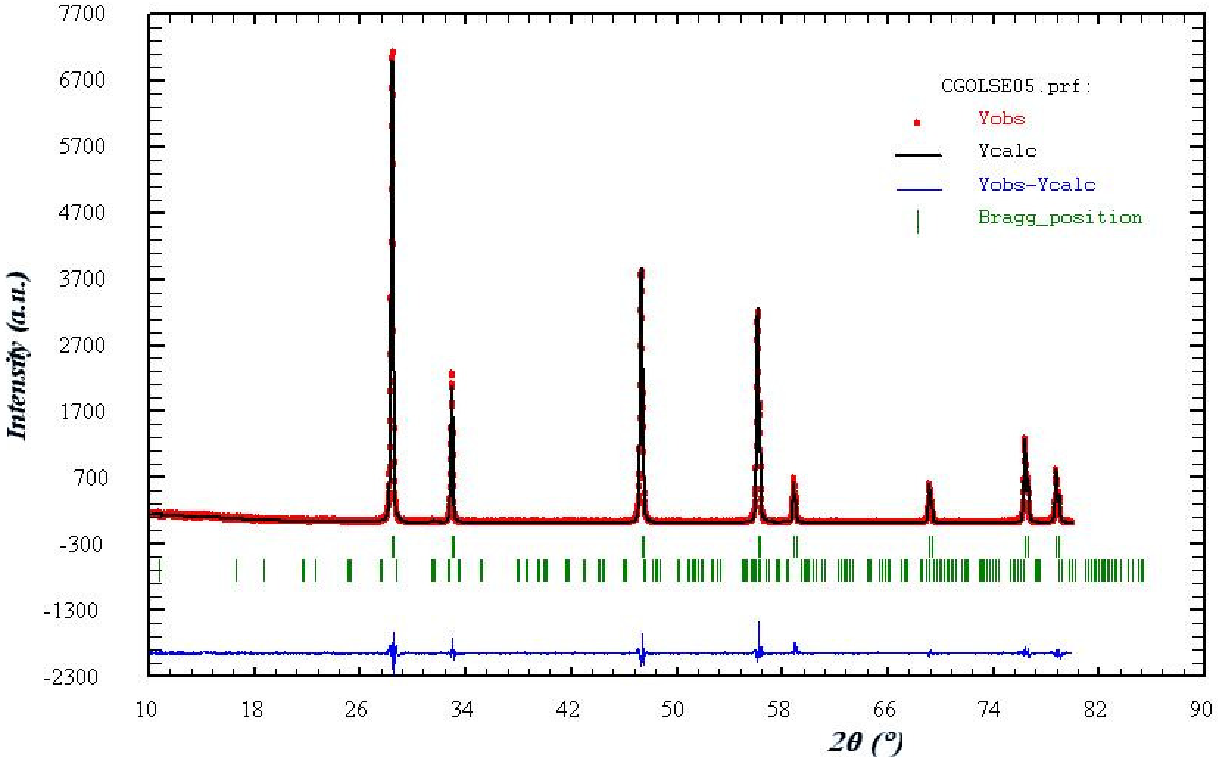

CGOLSE5

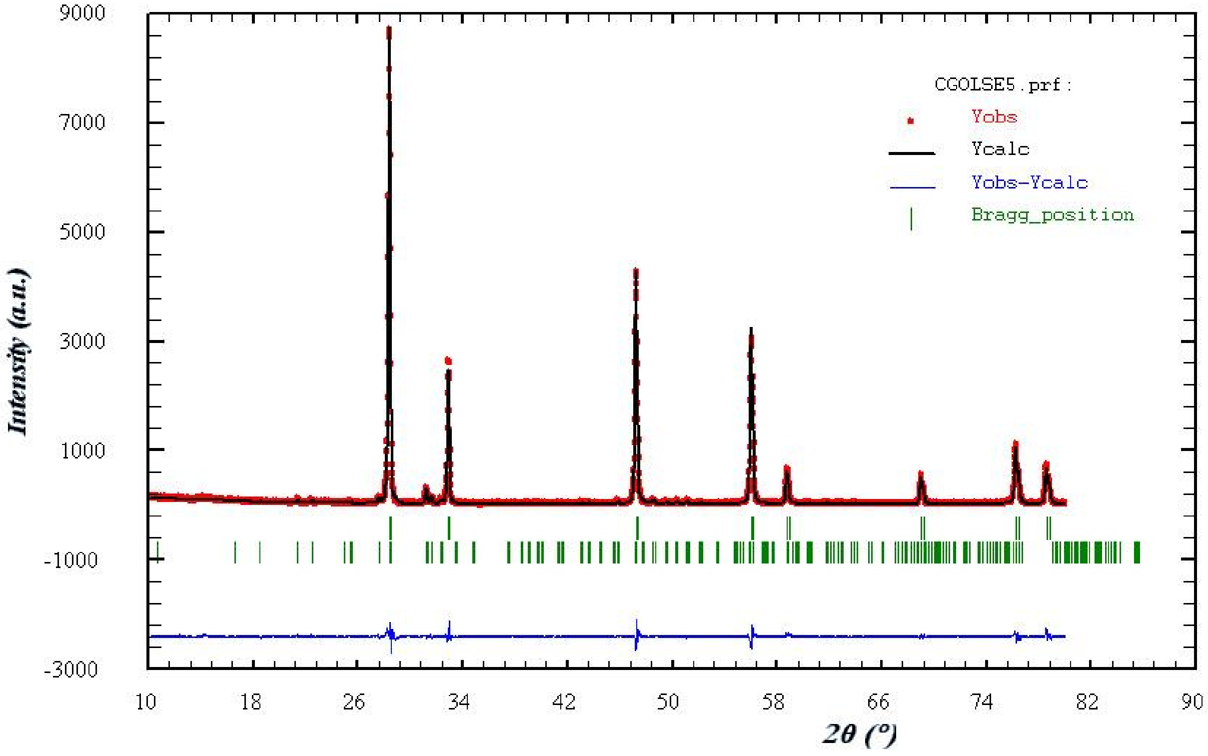

The quality of refinement can be estimated by means of reliability factors R_p, R_{wp}, R_{exp} and Chi2. The table with these reliability factors is represented below.

Reliability factors with all non-excluded points for pattern								
Sample	R-factors (not corrected for background) for Pattern				Conventional Rietveld R-factors for Pattern			
	R_p	R_{wp}	R_{exp}	Chi2	R_p	R_{wp}	R_{exp}	Chi2
CGOSi-0.5%	8.24	12.0	9.64	1.55	11.8	12.0	9.64	1.55
CGOSi-5%	7.20	10.50	8.69	1.47	9.71	12.6	10.40	1.47
CGOLSL-0.5%	8.34	11.8	9.19	1.65	11.7	14.3	11.13	1.65
CGOLSL-5%	8.42	12.3	9.14	1.8	11.9	15.1	11.24	1.80
CGOLSE-0.5%	8.43	12.1	9.67	1.56	12.3	14.9	11.97	1.56
CGOLSE-5%	7.69	11.2	8.97	1.57	10.5	13.5	10.81	1.57

Reliability factors for points with Bragg contributions for pattern								
Sample	R-factors (not corrected for background) for Pattern				Conventional Rietveld R-factors for Pattern			
	R_p	R_{wp}	R_{exp}	Chi2	R_p	R_{wp}	R_{exp}	Chi2
CGOSi-0.5%	8.25	12.0	9.64	1.55	11.6	14.6	11.71	1.55
CGOSi-5%	7.22	10.6	8.68	1.48	9.6	12.6	10.32	1.48
CGOLSL-0.5%	8.28	11.8	9.18	1.64	11.4	14.1	11.02	1.64
CGOLSL-5%	8.36	12.2	9.14	1.79	11.6	14.9	11.12	1.79
CGOLSE-0.5%	8.42	12.1	9.67	1.56	12.1	14.9	11.90	1.56
CGOLSE-5%	7.66	11.2	8.96	1.57	10.4	13.5	10.75	1.57

This table illustrates that the model for refinement was chosen properly. However, since the values of R_p and R_{wp} are a slightly higher then 10, the quality of refinement is moderate.

Appendix II

This section includes details on the micristructures of most materials studied in this work. The major microstructural features of all these compositions were already discussed in Chapter 3.

Combined SEM/EDS micrographs of apatite-containing CGO ceramics (a-k)

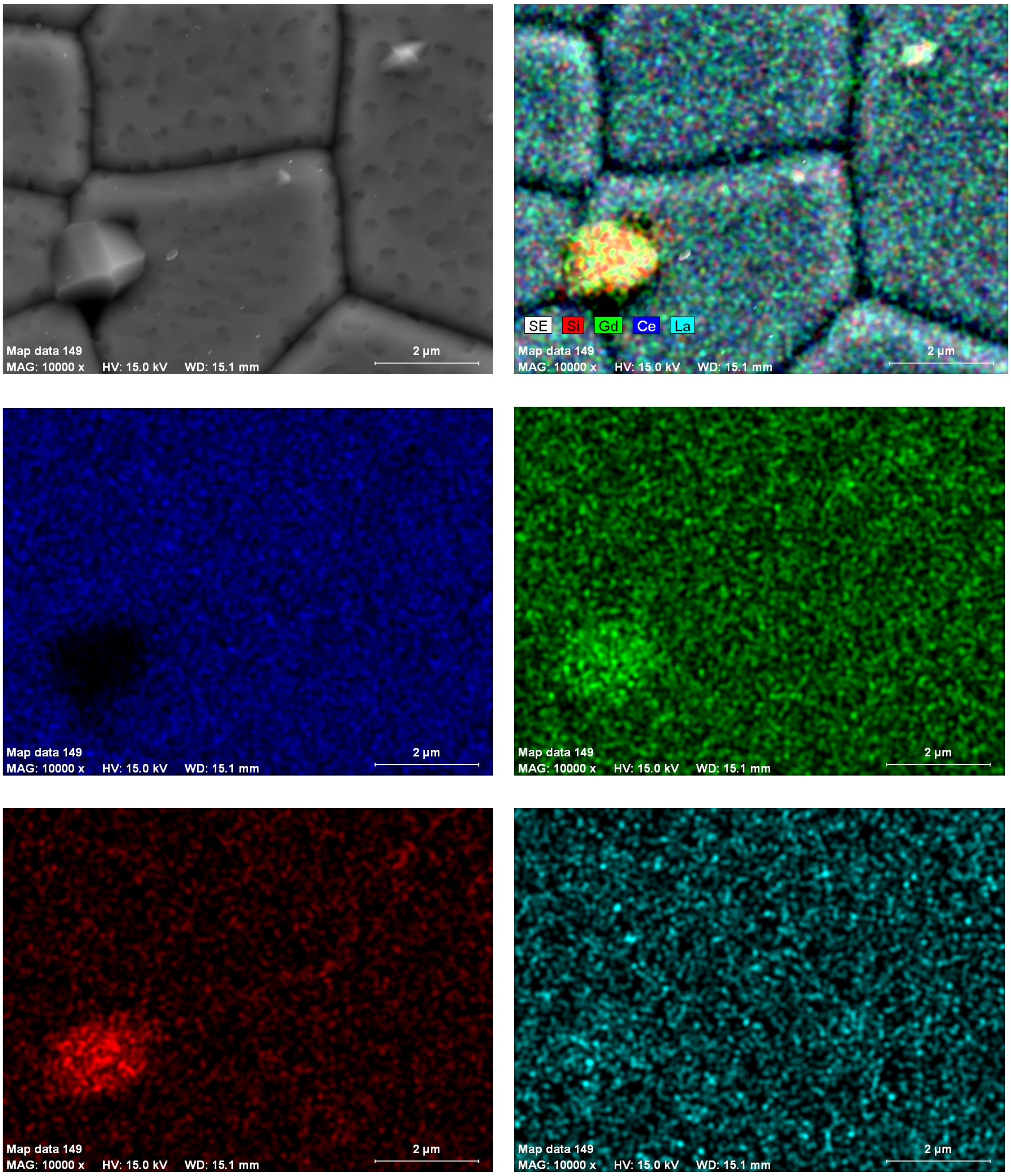

a) Microstructure and EDS mapping of the CGOLSL-0.5%-ap ceramics

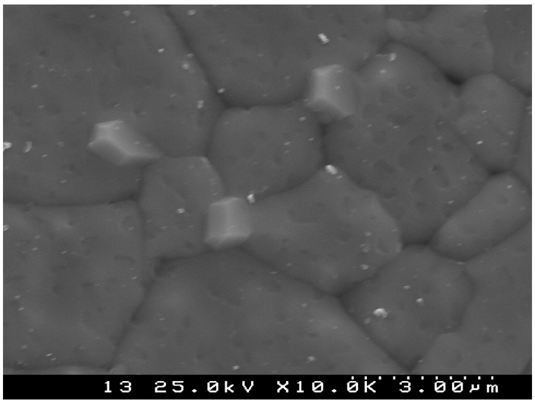

b) Microstructure of the CGOLSL-0.5%-ox ceramics

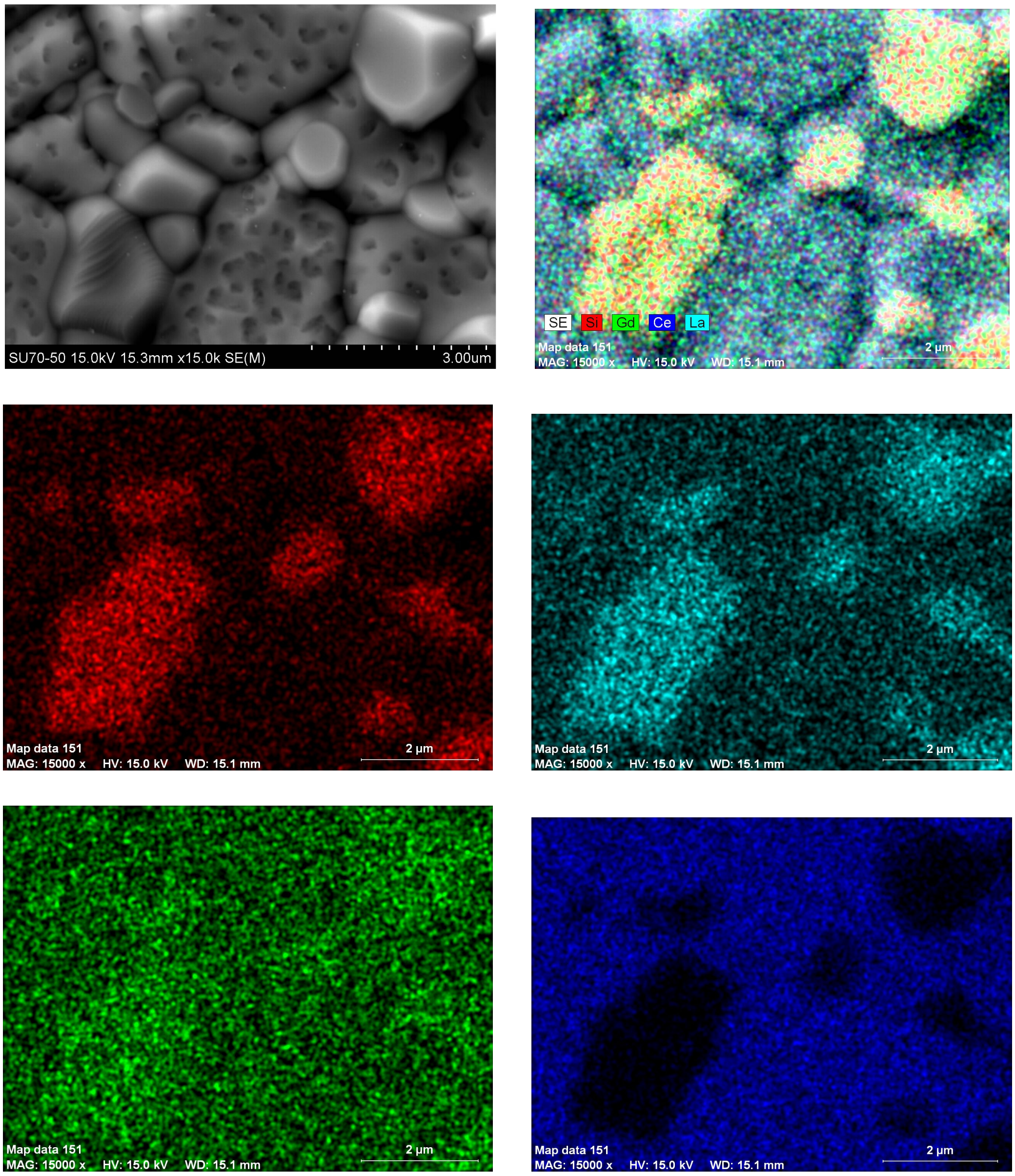

c) Microstructure and EDS mapping of the CGOLSL-5%-ap ceramics

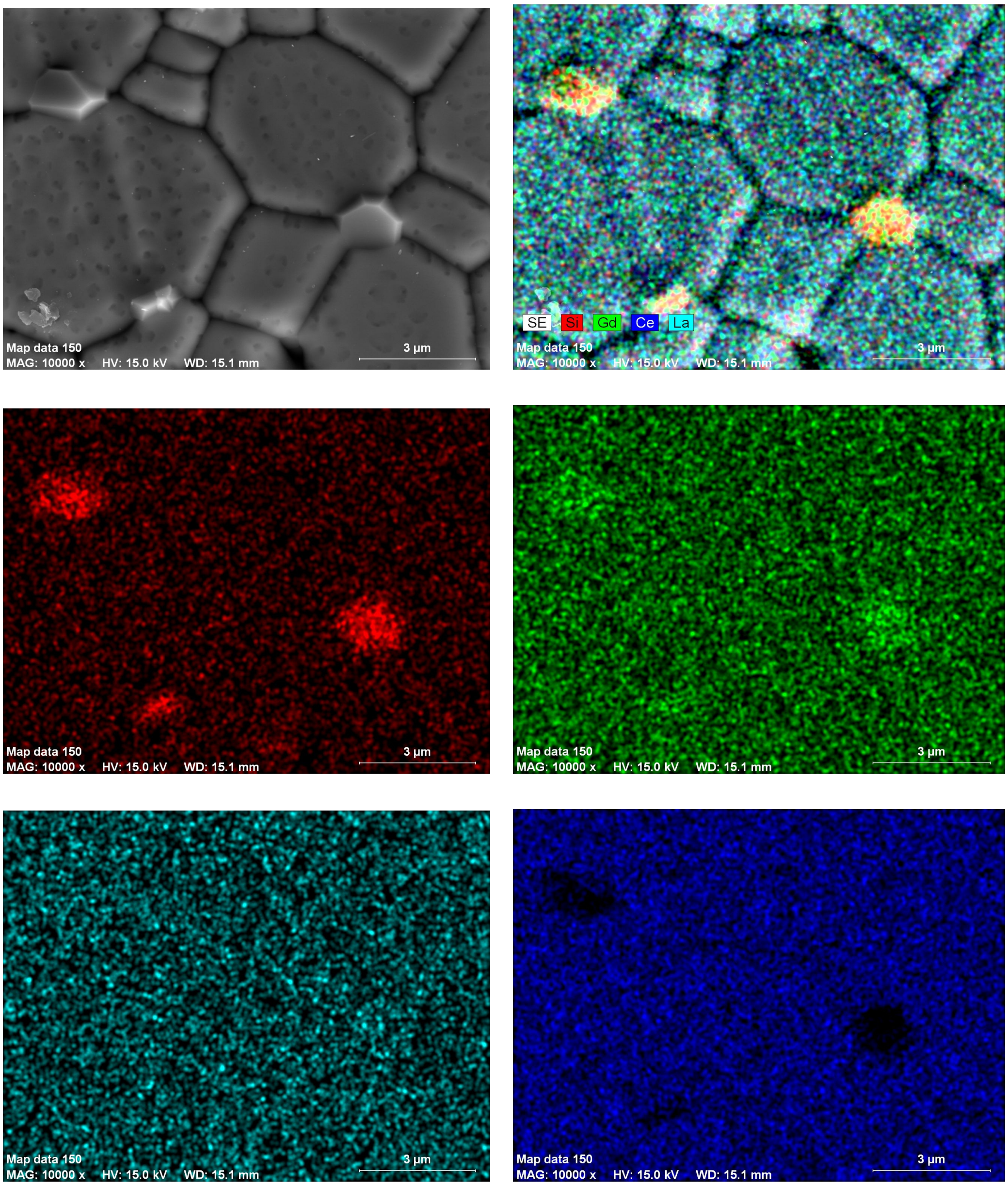

d) Microstructure and EDS mapping of the CGOLSE-0.5%-ap ceramics

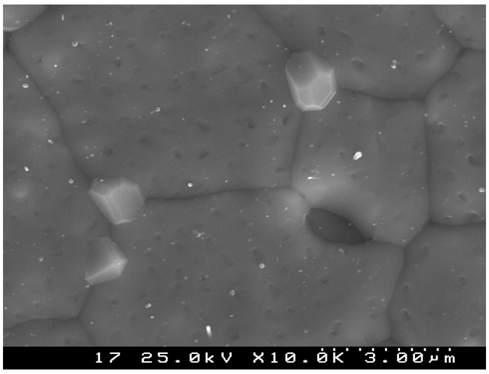

e) Microstructure of the CGOLSE-0.5%-ox ceramics

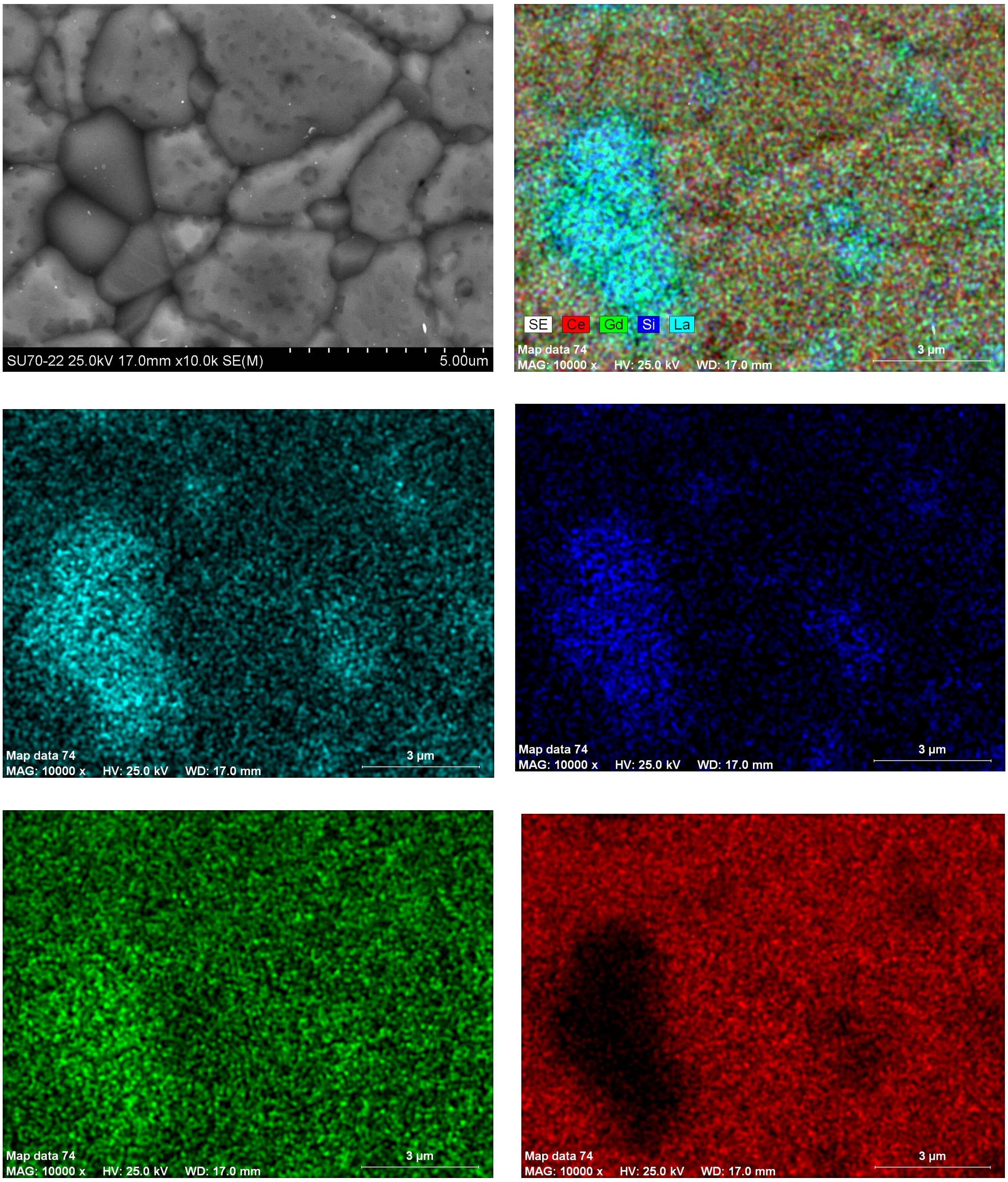

f) Microstructure and EDS mapping of the CGOLSE-5%-ap ceramics

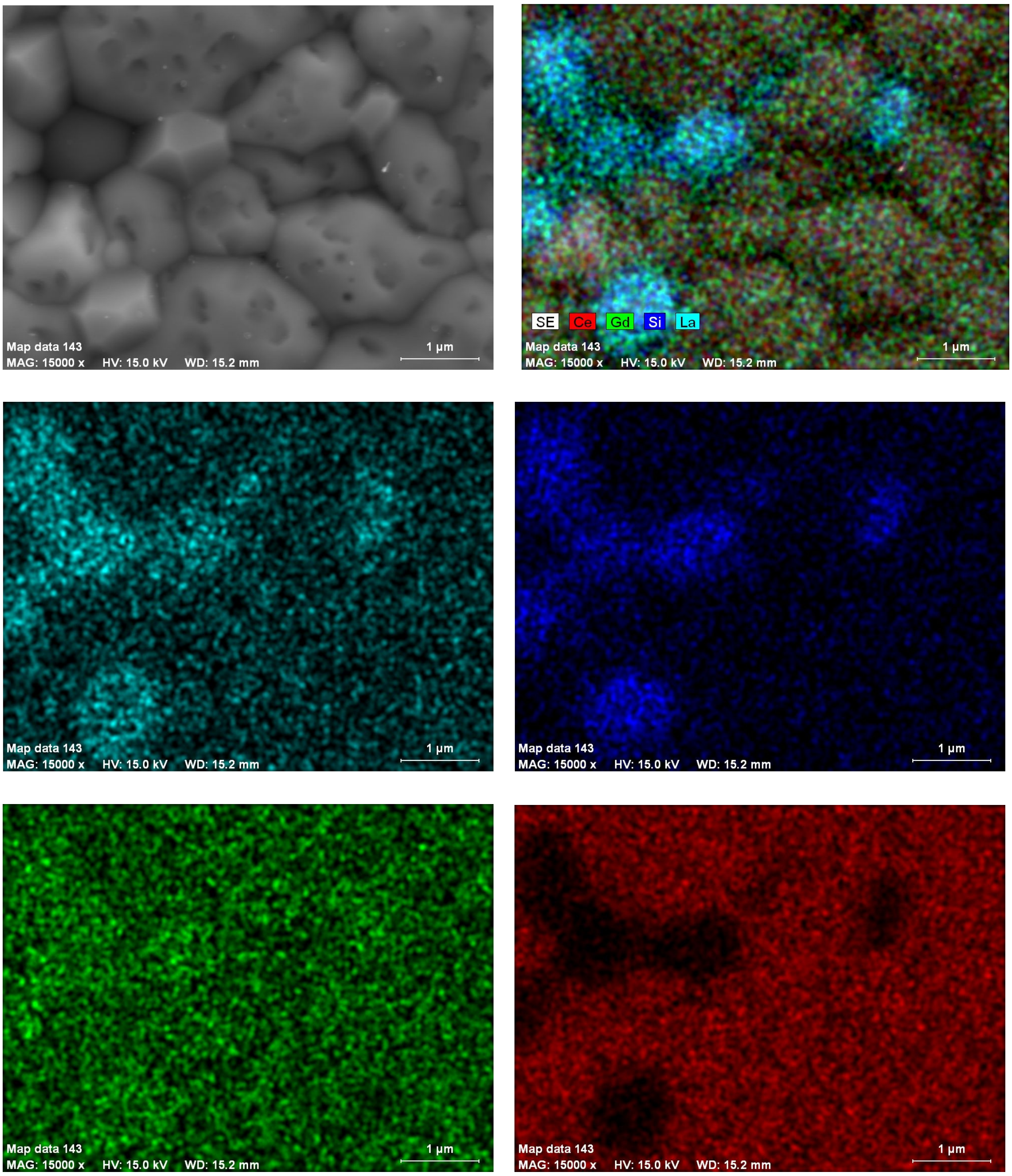

g) Microstructure and EDS mapping of the CGOLSE-5%-ox ceramics

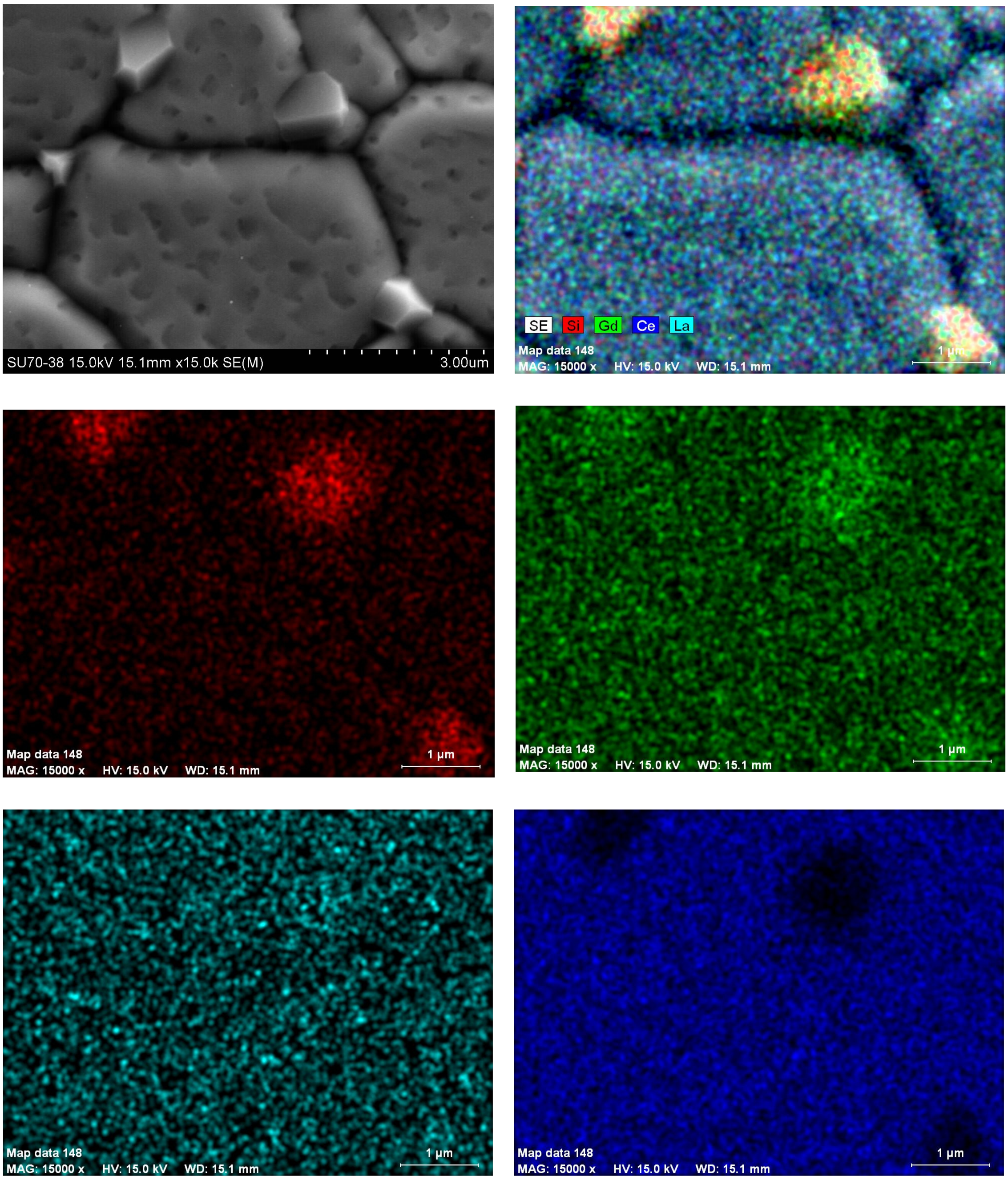

h) Microstructure and EDS mapping of the CGOLSH-0.5%-ap ceramics

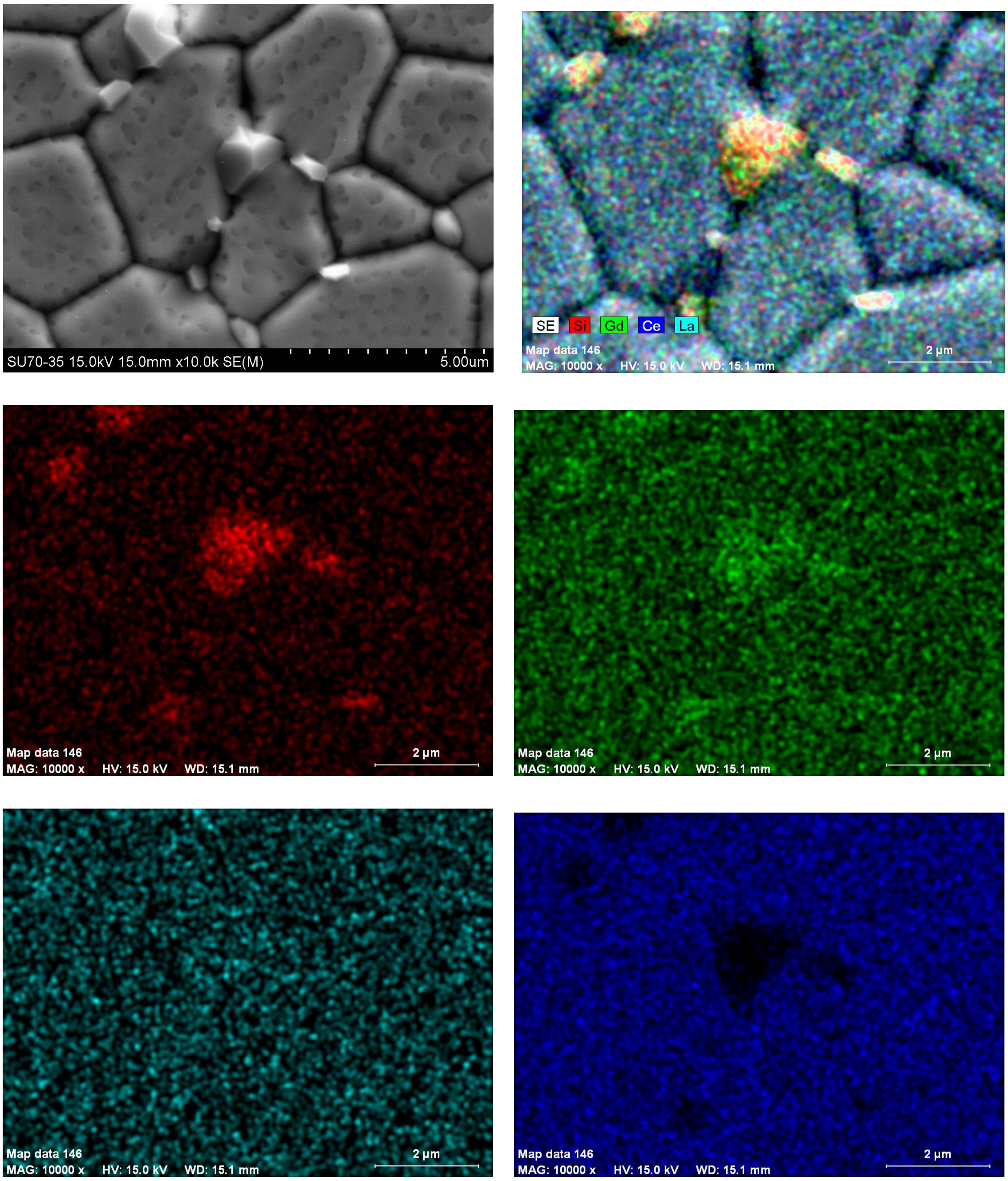

i) Microstructure and EDS mapping of the CGOLSH-0.5%-ox ceramics

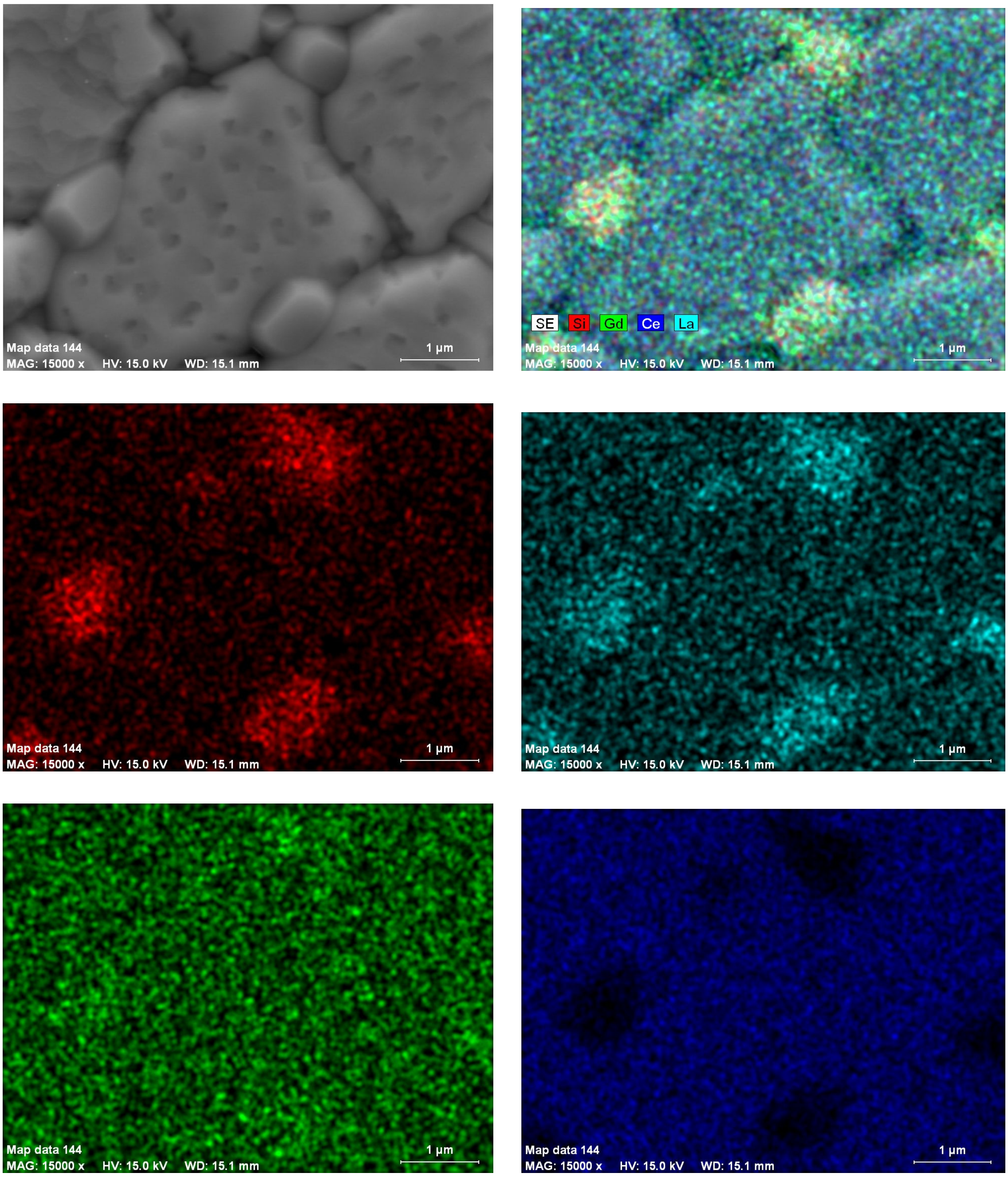

j) Microstructure and EDS mapping of the CGOLSH-5%-ap ceramics

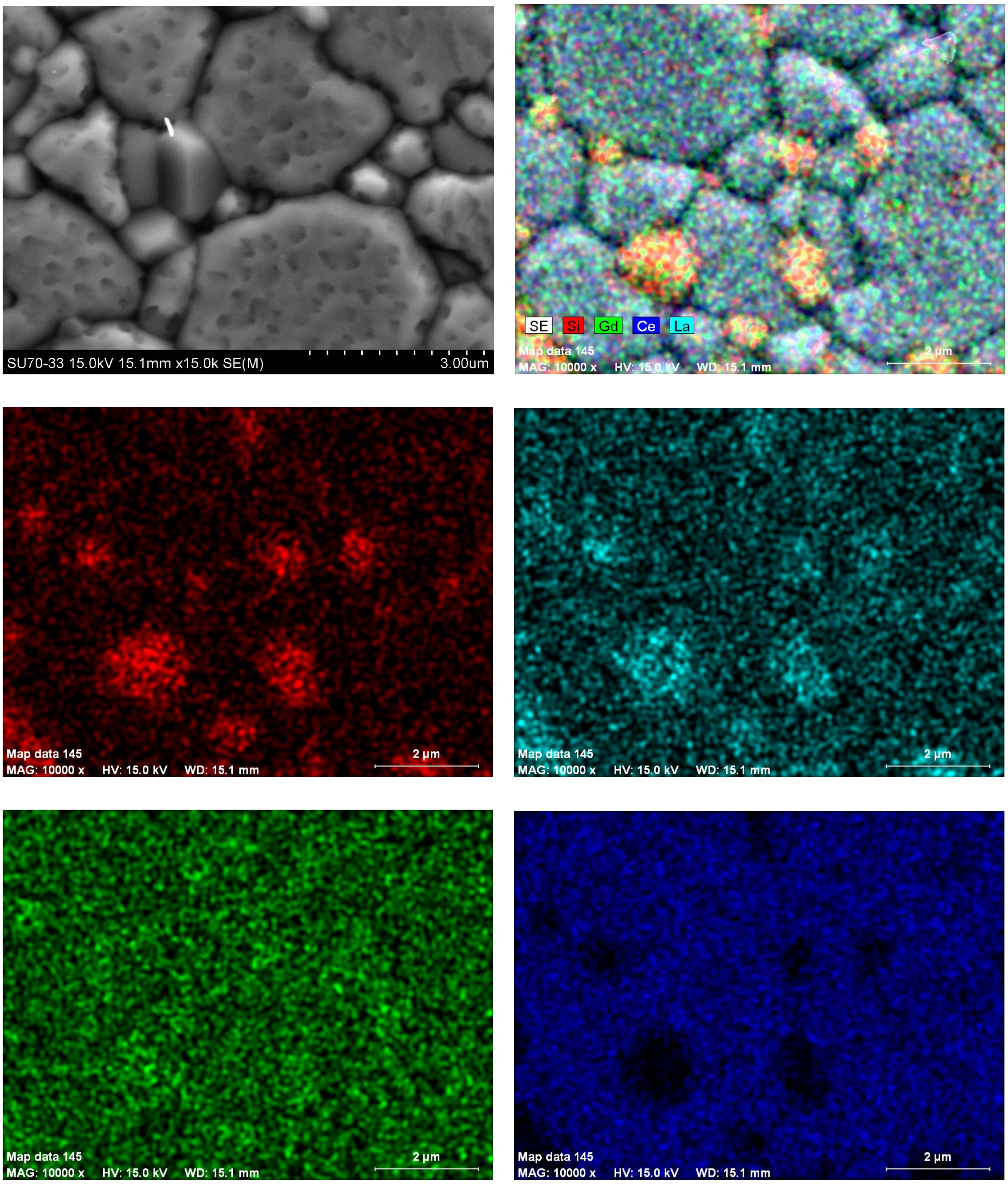

k) Microstructure and EDS mapping of the CGOLSH-5%-ox ceramics